UNIVERSIDAD
DE MÁLAGA

Elena Navarrete Astorga

TESIS DOCTORAL

2015

UNIVERSIDAD DE MÁLAGA
FACULTAD DE CIENCIAS
DPTO. FÍSICA APLICADA I

UNIVERSIDAD
DE MÁLAGA

TESIS DOCTORAL

OPTIMIZATION OF PROCESSES FOR THE REAR SIDE OF MONOCRYSTALLINE SILICON SOLAR CELLS

Química Avanzada. Preparación y Caracterización de Materiales

2015

Director: José Ramón Ramos Barrado

Elena Navarrete Astorga

UNIVERSIDAD DE MÁLAGA

DEPARTAMENTO DE FÍSICA APLICADA I

OPTIMIZATION OF PROCESSES FOR THE REAR SIDE OF MONOCRYSTALLINE SILICON SOLAR CELLS

TESIS DOCTORAL

Director:

José Ramón Ramos Barrado

Química Avanzada. Preparación y Caracterización de Materiales

Elena Navarrete Astorga

2015

Publicaciones y
Divulgación Científica

AUTOR: Elena Navarrete Astorga
EDITA: Publicaciones y Divulgación Científica. Universidad de Málaga

OPTIMIZATION OF PROCESSES FOR THE REAR SIDE OF MONOCRYSTALLINE SILICON SOLAR CELLS

Memoria presentada por la Ingeniera Química Dña. Elena Navarrete Astorga en cumplimiento de los requisitos para optar al grado de Doctor por la Universidad de Málaga.

Thesis submitted by the chemical engineer Elena Navarrete Astorga in partial fulfillment of the requirements for the degree of Doctor of the Universidad de Malaga.

Fdo.: Elena Navarrete Astorga

Málaga, 19 de marzo de 2015

El presente trabajo ha sido llevado a cabo con el apoyo del Ministerio de Economía y Competitividad de España través del proyecto TEC2010-16700 y de la Junta de Andalucía a través del grupo de investigación FQM-192.

This work has been supported by the Ministry of Economy and Competitiveness of Spain through the research project TEC2010-16700 and the research group FQM-192 related to the Junta de Andalusia (regional Andalusia government).

D. José Ramón Ramos Barrado, Catedrático de Universidad y Director del Departamento de Física Aplicada I, de la Universidad de Málaga,

CERTIFICA:

Que la memoria presentada por la Ingeniera Química Dña. Elena Navarrete Astorga, bajo el título "Optimization of processes for the rear side of monocrystalline silicon solar cells", ha sido realizada bajo mi dirección en los laboratorios del Departamento de Física Aplicada I de la Universidad de Málaga, reuniendo a mi juicio los requisitos necesarios para optar al grado de Doctor por la Universidad de Málaga, por lo que autorizo su presentación.

Y para que así conste, firmo el presente certificado en Málaga, a 19 de marzo de 2015.

Fdo.: José Ramón Ramos Barrado

Catedrático de Universidad

Dpto. Física Aplicada I

Universidad de Málaga

D. José Ramón Ramos Barrado, Catedrático de Universidad, Director del Departamento de Física Aplicada I y Coordinador del Programa de Doctorado *Química Avanzada: Preparación y Caracterización de Materiales*, de la Universidad de Málaga,

CERTIFICA:

Que la Tesis Doctoral, titulada "Optimization of processes for the rear side of monocrystalline silicon solar cells", constituye la memoria que presenta Dña. Elena Navarrete Astorga para optar al título de Doctor por la Universidad de Málaga, y que ha sido realizada bajo la dirección del Doctor D. José Ramón Ramos Barrado, en el Departamento de Física Aplicada I de la Universidad de Málaga.

Y para que así conste, firmo el presente certificado en Málaga, a 19 de marzo de 2015.

Fdo. José Ramón Ramos Barrado

AGRADECIMIENTOS

En primer lugar, quiero agradecer al profesor José Ramón Ramos Barrado por darme la oportunidad de llevar a cabo trabajos de investigación en su grupo *Laboratorio de Materiales y Superficies*, entre ellos la realización de esta tesis. Por su confianza, por estar siempre disponible para hablar y escuchar mis propuestas. Por permitirme evolucionar como investigadora, tanto en la Universidad de Málaga como en estancias en centros de investigación del extranjero y congresos internacionales. Me gustaría agradecer también al resto de componentes del grupo de investigación, con especial interés al profesor Francisco de Paula Martín Jiménez, por "meterme el gusanillo" de la investigación en mis últimos años de carrera y confiar en mí desde el principio. A la profesora Mercedes Gabás Pérez, por aportarme tantos conocimientos sobre el óxido de zinc y guiarme en el desarrollo de dicha investigación.

Gracias a Enrique Dalchiele, profesor de la Universidad de Uruguay, con el que es una alegría trabajar por su simpatía y buen hacer. Gracias a Cándido Vázquez por su colaboración durante su permanencia en Isofotón. ¡Ojalá no hubiera cerrado de tan mala manera y pudiéramos haber terminado los experimentos programados!

Me gustaría agradecer a todos los miembros del personal técnico, especialmente a los señores del microscopio, Goyo, David y Adolfo, por tener siempre un hueco para mí, a Laura de rayos X por ser tan eficiente, a Valle, Cristina, Shanti, y resto de técnicos que han hecho que parte de la caracterización de las muestras de este trabajo sea posible. A Juan Antonio y Jesús, del taller de mecanizado, por aportar buenas ideas a mis diseños y estar siempre disponibles. A Pedro, técnico de Ingeniería Química, por ser tan servicial y trabajar siempre con una sonrisa.

Gracias a los miembros del ICMM-CSIC, en especial a Fernando y Ángel, por aportar sus conocimientos acerca de Raman y TEM. Agradezco también la colaboración de Íñigo Ciarsolo, de Tekniker, surgida del proyecto Consolider.

A mis compañeros de doctorado, Ana, Virginia, Jorge, Efraín y Rafa. Gracias por aportar conocimientos y dar un toque de humor a la vida investigadora. A Rocío, por ser una buena compañera, además de una profesional en el manejo del microscopio SEM; por hacerme siempre hueco para mis medidas.

A Miguel y Javier, cuyos proyectos finales de carrera tuve el placer de dirigir durante la última etapa de la tesis. Gracias por aportar tantas ideas y por vuestro trabajo. Hemos aprendido mucho juntos.

Gracias a Daniel Biro por acogerme durante seis meses en su grupo de investigación del Fraunhofer ISE (Alemania), así como a los integrantes del mismo, especialmente

Robert Woehl, Achim Kimmerle y Benjamin Thaidigsmann, el cual me introdujo en el estudio del *fire-through contact*. Gracias también a Maximilian Pospischil y Saskia Kühnhold, compañeros en el Fraunhofer y amigos para siempre; sin ellos mi estancia en Alemania hubiese sido (aún) más fría.

Quisiera agradecer a Miquel Salmerón, por invitarme a realizar una estancia en su grupo, en la Universidad de California, Berkeley. Gracias por contestar a todas mis preguntas y por enseñarme con tanta humildad.

Agradecer el apoyo económico del Ministerio de Economía y Competitividad de España través del proyecto TEC2010-16700, mediante el que he disfrutado de una beca de formación de personal investigador (FPI).

"Los últimos serán los primeros". Por ello, muchas gracias a mis padres, Águeda y Jesús, por guiarme en el camino de la vida y estar siempre a mi lado. Sin ellos, no sería lo que hoy soy. Gracias a mi hermano, Jesús, por ser siempre tan optimista y enseñarme que la vida no está hecha para los débiles. Gracias también a mi abuela Antonia, que con 95 años, me ha transmitido mucha sabiduría y calma en los momentos más difíciles.

Gracias al mejor compañero de laboratorio, Jorge, que resulta ser también mi mejor amigo y mi marido. Juntos, hemos hecho que esto sea posible. Gracias.

A mi familia

RESUMEN

En esta tesis, se ha estudiado la formación de un campo local superficial trasero (LBSF) de aluminio mediante el uso de diferentes pastas de dicho metal, las cuales contienen fritas en su composición para una mejor sinterización. Para la impresión de la pasta sobre los diferentes sustratos de silicio monocristalino de tipo p se han empleado dos técnicas diferentes. Por un lado, la serigrafía, técnica ampliamente usada en la industria fotovoltaica tanto para la formación de contactos frontales como posteriores. Por el otro lado, se ha utilizado también la técnica de dispensado, la cual permite una impresión de la pasta evitando el contacto con el sustrato, posibilitando la impresión sobre obleas muy finas de silicio evitando su rotura.

Se han obtenido las resistencias específicas de contacto para las diferentes estructuras de aluminio creadas y los resultados se han comparado para diferentes pastas y sustratos. De esta manera, previa comprobación mediante imágenes microscópicas de cortes transversales de las muestras, se garantiza la formación del campo local superficial trasero.

Con el objetivo de una mejora de la eficiencia de las células solares de silicio, se han depositado diferentes capas finas sobre sustratos de silicio mediante las técnicas de magnetrón sputtering y PECVD (*Plasma Enhanced Chemical Vapor Deposition*), con el fin de darle características pasivantes, como SiO_2, SiN_x y SiriON (*silicon rich oxynitride*); antirreflejantes, como SiN_x; o de óxido conductor transparente para células de heterounión, como el caso de la capa de ZnO:Al. Para el estudio de dichas propiedades, se han empleado diversas técnicas, como QSSPC (*Quasi-Steady State Photoconductance*) para analizar la calidad de la pasivación y espectrofotometría para la medida de las propiedades ópticas. También se han empleado técnicas de caracterización de capa delgada para analizar su estructura y morfología.

Sobre las capas finas depositadas sobre silicio, se ha realizado el depósito de las pastas de aluminio para, mediante el método FTC (*fire through contact*), formar un campo local superficial trasero. Este método se ha utilizado como alternativa a los que se suelen usar en la industria fotovoltaica, los cuales utilizan una serie de pasos que incrementan el coste del proceso total, como láseres o el depósito de resinas para la posterior eliminación por método químico antes de la impresión metálica.

Se incluye un capítulo dedicado a la optimización del emisor de aluminio para células de contacto-trasero unión-trasera desarrollado en el Fraunhofer ISE (Alemania), con el objeto de aplicar las mismas técnicas de recubrimiento para el desarrollo de este nuevo tipo de celda solar y su posible transferencia a la producción industrial, atendiendo al proyecto de plan nacional de título *Transferencia de las estructuras de alta eficiencia a la producción industrial.*

ABSTRACT

In this thesis, the formation of an aluminum local back surface field (LBSF) has been studied through the use of different pastes of this metal which contain frits in its composition to obtain better sintering properties of the contact layer. Two different technologies have been employed to carry out the printing of the monocrystalline p-type silicon substrates with aluminum pastes. On the one side, screen printing technology, widely used in photovoltaic industry for the formation of front and rear contacts. On the other side, dispensing technology, which allows printing the wafer avoiding the contact, being favorable for the printing on very thin wafers to avoid its breakage.

The specific contact resistance of the different aluminum structures has been obtained, and the results were compared for different pastes and substrates. Thus, after verification through cross-sections microscopy images, the formation of the local back surface field can be assured.

To explore the enhancement of the silicon solar cells efficiency, different thin films were deposited on silicon substrates by magnetron sputtering and PECVD (Plasma Enhanced Chemical Vapor Deposition*)*: with the aim to passivate the surface, like SiO_2, SiN_x and SiriON (silicon rich oxynitride); working as ARCs, like SiN_x; or TCOs for heterojunction silicon solar cells, like the AZO (aluminum doped ZnO) films. To study the properties of the films, different techniques have been employed, like QPPSC (Quasi-Steady State Photoconductance*)* to analyze the passivation quality or a spectrophotometer to measure the optical properties. Characterization techniques were also applied to analyze the structure and morphology of the obtained thin films.

The thin films of SiO_2, SiO_2/ZnO, SiriON and SiO_2/SiN_x deposited on silicon were used as substrates for the deposition of the aluminum pastes and, through the FTC (Fire Through Contact) method, obtain a local back surface field. This method has been implemented as an alternative to the normally used in the photovoltaic industry, which require more steps that increase the process total cost, like lasers or the method of deposition of resins and its etching with chemicals before metal printing.

A final chapter about the optimization of the aluminum emitter for BJ-BC (Back Junction-Back Contact) silicon solar cells, developed during the six months stay in the Solar Energy Institute Fraunhofer ISE, Freiburg (Germany), is included. The aim of this chapter was the application of the same techniques described previously for the development of this new type of silicon solar cells and its possible transference to the industrial production, as the national project, *Transfer of high-efficiency solar cell structure into industrial production,* suggests.

LIST OF ACRONYMS AND SYMBOLS

Acronym	Description
Al_2O_3	aluminum oxide
AFM	Atomic Force Microscopy
ALD	Atomic Layer Deposition
AM1.5g	Air Mass 1.5 global spectrum
ARC	Anti-Reflective Coating
AZO	Aluminum-doped Zinc Oxide
BC-BJ	Back-Contact Back-Junction
BSF	Back Surface Field
CVD	Chemical Vapor Deposition
Cz	monocrystalline silicon produced by Czochralski method
ECV	Electrochemical Capacitance Voltage
EDX	Energy Dispersive X-ray
FC	Firng Condition
FESEM	Field Emission Scanning Electron Microscope
FTC	Fire Tthrough Contact
FZ	monocrystalline silicon produced by Float-Zone
H_2O_2	hydrogen peroxide
HCl	hydrochloric acid
LBSF	Local Back Surface Field
mpp	maximum power point

Acronym	Description
PECVD	Plasma-Enhanced Chemical Vapor Deposition
PERC	Passivated Emitter Rear Contact
PERL	Passivated Emitter Rear Locally diffused
PL	photoluminescence
$POCl_3$	phosphoroxychlorid
QSSPC	Quasi-Steady State Photoconductance
RMS	Root Mean Square
SEM	Scanning Electron Microscope
SiN_x	silicon nitride
SiO_2	thermal (di)oxide
SNMS	Secondary Neutral Mass Spectroscopy
SRH	Shockley-Read-Hall
SRV	Surface Recombination Velocity
TEM	Transmission Electron Microscope
TLM	Transmission Line Measurement
XPS	X-ray Photoelectron Spectroscopy
XRD	X-Ray Dispersion

Symbol	Description	Unit
D_{min}	diffusion constant of minority carrier	$m^2\ s^{-1}$
$d_{Si,dis}$	thickness of dissolved silicon	m
E_g	band gap	eV

Symbol	Description	Unit
FF	fill factor	%
G	generation rate	$m^{-3}\ s^{-1}$
j	current density	$A\ m^{-2}$
J_{0e}	emitter saturation current density	$A\ m^{2}$
J_{0s}	surface saturation current density	$A\ m^{2}$
j_{mpp}	current density at maximum power point	$A\ m^{-2}$
J_n	saturation current density	$A\ m^{-2}$
j_{ph}	photocurrent density	$A\ m^{-2}$
j_{sc}	short-circuit current density	$A\ m^{-2}$
λ	wavelength	nm
k	imaginary part of refraction index	-
n	electron density	m^{-3}
n_0	equilibrium concentrations of electrons	m^{-3}
N_D	concentration of donor atoms	m^{-3}
R	resistance	Ω
R_c	contact resistance	Ω
r_p	parallel resistance	$\Omega\ m^{2}$
r_s	area-weighted series resistance	$\Omega\ m^{2}$
R_{sh}	sheet resistance	Ω/sq
S_{eff}	effective SRV	$m\ s^{-1}$
S_{front}	front surface recombination velocity	$m\ s^{-1}$
$S_{met,eff}$	effective SRV of metallized area	$m\ s^{-1}$

Symbol	Description	Unit
T	temperature	°C
t	time	s
U	recombination rate	$m^{-3}\ s^{-1}$
V	voltage	V
V_{mpp}	voltage at maximum power point	V
V_{oc}	open-circuit voltage	V
V_{ph}	photo voltage	V
Δn	excess carrier concentration	m^{-3}
Φ	power density	$W\ m^{-2}$
η	photon conversion efficiency	%
ρ_c	specific contact resistance	$\Omega\ m^2$
σ	conductivity	$A\ V^{-1}\ m^{-1}$
τ	minority carrier lifetime	s
τ_{Aug}	Auger minority carrier lifetime	s
τ_{bulk}	minority carrier bulk lifetime	s
τ_{eff}	effective minority carrier lifetime	s
τ_{SRH}	Shockley-Read-Hall minority carrier lifetime	s

TABLE OF CONTENTS

1

Introduction

1.1. Motivation and aim of this work

Having in mind all types of renewable energy, photovoltaics has the enormous advantage that it exhibits an abundant capacity on Earth, because sunlight, which is available everywhere to a different extent and can be converted into electricity directly. Figure 1.1 shows the world map of the global horizontal irradiation, which is the most important parameter for evaluation of the solar energy potential of a particular region. The average annual sum of this parameter in Spain was comprised between 1200 and 1950 kWh/m^2, reaching the maximum value in Andalusia.

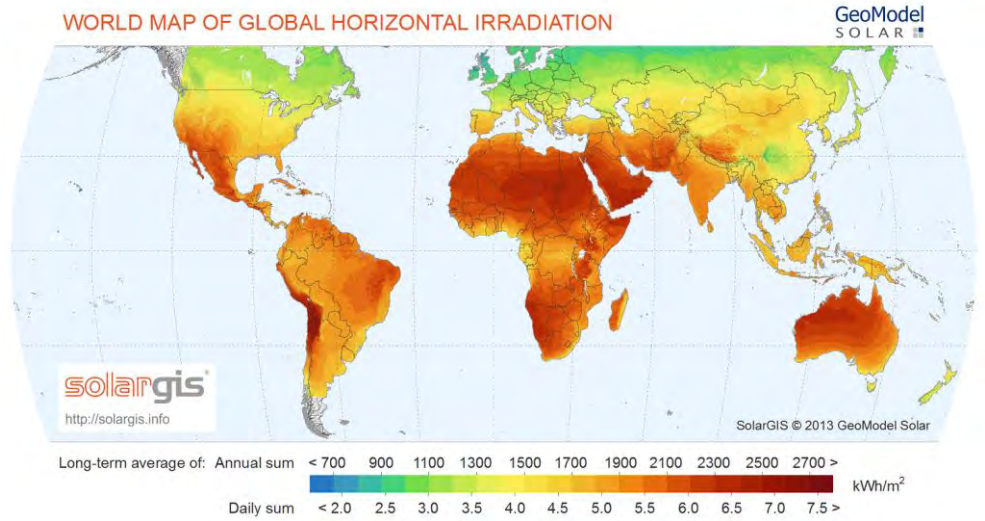

Figure 1.1. World map of global horizontal irradiation [1].

Since 2010, the world has added more solar photovoltaic capacity than in the previous four decades, being the total global capacity 150 GW in early 2014 [2]. Nowadays, about 90% of the photovoltaic energy production is generated by crystalline silicon wafer-based technology. But the cost of this energy production technology is still rather high. This cost could be decreased by simplifying the fabrication process steps, but also by using less material resources. A particular solution for the last issue would be using thinner silicon wafers as substrates, employing special techniques to avoid the breaking of the wafers. In this work, this issue was carried out by the using of a non-contact printing technology called as drop on demand, or dispensing technology in general. Moreover, in this work the fire through contact (FTC) method was implemented with the aim to reduce costs as well. By the application of this method, the step of creating a mask on the passivation layer to do a partial removing and printing the metal just in the places without it was eliminated can be omitted. Instead of it, the use of special aluminum pastes offers the opportunity to go through this

passivation layer and form the Al-Si eutectic to obtain the local back surface field. Furthermore, aluminum pastes were chosen instead of silver pastes because of the high cost of the last ones.

The main challenge of this thesis was the obtaining of an aluminum local back surface field by different techniques using several layers with the aim to passivate the cell and thus enhance the efficiency. A deep study on these layers was carried out when deposited on silicon, not just for the passivation quality of the layers but for the ability of working as antireflection coatings which is the case of layers such as SiN_x or as TCOs like Al:ZnO in heterojunction silicon solar cells. Moreover, aluminum pastes were also used to create the emitter in back-contact back-junction (BC-BJ) solar cells.

The quality of the passivation layers together with the good specific contact resistivity gave us signs of the improvement of a potential solar cell. Low-cost technology was implemented, like the FTC method mentioned before, for photovoltaics be competitive in the market, and thus, make a contribution in the direction of a sustainable energy production.

1.2. Thesis outline

In **chapter 2,** the background of the following work is described. Firstly, some basic semiconductor equations are presented together with the current-voltage characteristics of silicon solar cells. The loss mechanisms are explained having in mind the surface texturing process. The minority carrier lifetime is described as well and also the technique used to this study. The method used to carry out the contact resistance measurements is detailed. After that, the basic theory of alloying aluminum on silicon surfaces, which plays a key role in this work, is presented. Finally, the printing technologies and the thin film deposition methods using in this thesis are described.

In **chapter 3,** dielectric layers are created by diverse thin film preparation techniques. Some of them were studied as possible passivation layers for silicon solar cells and the structure of other films on silicon was analyzed and compared with the aim of working as antireflection coatings or TCOs for application to silicon solar cells. The quality of the passivation is studied by the QSSPC (quasi-steady state photoconductance) method, while the structure of the films was analyzed by several characterization techniques like XPS (X-ray Photoelectron Spectroscopy) and XRD (X-ray Diffraction) among others.

In **chapter 4,** screen-printed local Al-alloyed structures are analyzed on p-type monocrystalline silicon wafers with the aim to create a LBSF (Local Back Surface Field). The electrical properties of the local contacts were studied and an analysis of the microstructure was carried out as well. Firstly, the results by automatic screen printing carried out at Fraunhofer ISE during the stay of the author of this thesis are presented using the FTC method with different passivating layers and afterwards a manual screen printer was used to investigate the p^+-layer thickness on several dielectric layers.

In **chapter 5,** a dispensing robot was used to create aluminum structures on monocrystalline p-type silicon wafers with the same target when screen printing was used in the previous chapter. A local back surface field was created and studied its thickness. The specific contact resistance is compared for different aluminum pastes. To complete the study, a microstructure analysis was carried out.

Chapter 6 contains the results of the research carried out at Fraunhofer ISE related to the optimization of aluminum emitter for BC-BJ solar cells. Different structures were first printed with various aluminum pastes and then fired at different firing conditions. The results were compared regarding the contact resistance, the effective surface recombination velocity and a microstructure analysis.

2

Fundamentals

A solar cell is a device that converts sunlight directly into electricity through the photovoltaic effect. The efficiency of the cell quantifies the fraction of solar energy that it converts into electrical energy. In principle it depends on two parameters: the generation of current by absorbed incident illumination and the loss of charge carriers via so-called recombination mechanisms. A built in p-n diode separates charge carriers of opposite polarity, and drives the light-generated current through the cell and to the terminals. Finally, several solar cells will be electrically connected and encapsulated as a module. This chapter describes the background of the following thesis.

2.1. Current-voltage characteristic

The conversion efficiency η of light into electric energy is the most important parameter of a solar cell and also the most commonly used parameter to compare the performance of one solar cell to another. In order to measure it, the solar cell is illuminated with the standard spectrum AM1.5g (Air Mass 1.5 global) and a power density of Φ = 1000 W/cm² whereas the current-voltage characteristic is determined at a temperature T = 25°C (see Figure 2.1).

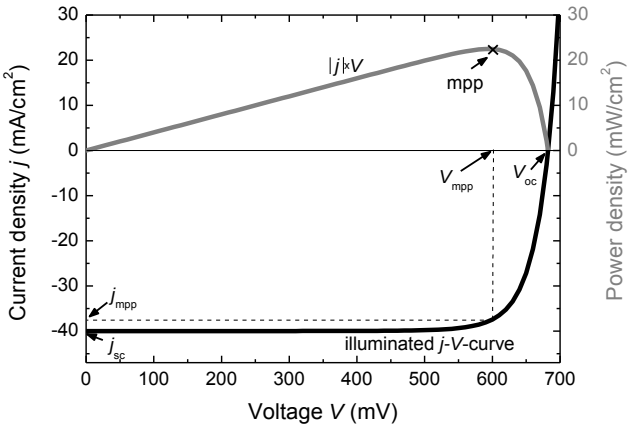

Figure 2.1. Illuminated j-v-curve together with the power density. The arrows show the important points along the curves [3]

At zero voltage the maximal current, called short-circuit current density *j*sc, is collected. The case where no current flows between the plus and minus contacts is reached under open-circuit conditions, measuring the open-circuit voltage *V*oc. In between lies the point where the highest power can be extracted, the maximum power point (mpp). With the voltage and current density at this point, the fill factor *FF* can be defined as follows:

$$FF = \frac{j_{mpp} \cdot V_{mpp}}{j_{sc} \cdot V_{oc}} \tag{2.1}$$

For standard silicon solar cells values of 80 to 85% can be achieved. The efficiency η then can be calculated:

$$\eta = \frac{j_{mpp} \cdot V_{mpp}}{\Phi} = \frac{j_{sc} \cdot V_{oc}}{\Phi} \cdot FF \tag{2.2}$$

2.1.1. Ideal diode equation

Electrically, the solar cell is equivalent to a current generator in parallel with an asymmetric, nonlinear resistive element, i.e., a diode (Figure 2.2).

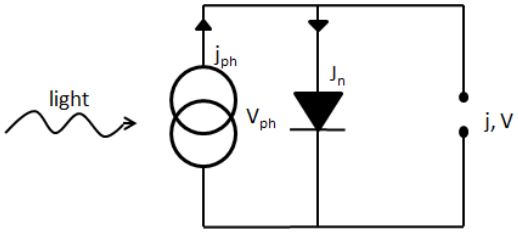

Figure 2.2. Equivalent circuit of ideal solar cell.

When illuminated, the ideal cell produces a photocurrent j_{ph} proportional to the light intensity. That photocurrent is divided between the variable resistance of the diode and the load, in a ratio which depends on the resistance of the load and the level of illumination. For high resistances, most of the photocurrent flows through the diode, resulting in a higher potential difference between the cell terminals but a smaller current though the load. The diode thus provides the photovoltage. J_n is the saturation current density.

2.1.2. Double diode equation

In real cells power is dissipated through the resistance of the contacts and through leakage currents around the sides of the device. These effects are equivalent electrically to two parasitic resistances in series (rs) and in parallel (rp) with the cell.

The circuit diagram (Figure 2.3) shows the photo current density j_{ph} and photo voltage V_{ph} generated by light (left side). Parallel resistance r_p (sometimes called shunt), series resistance r_s and losses due to the diode lead to a lower measured j and V (right side).

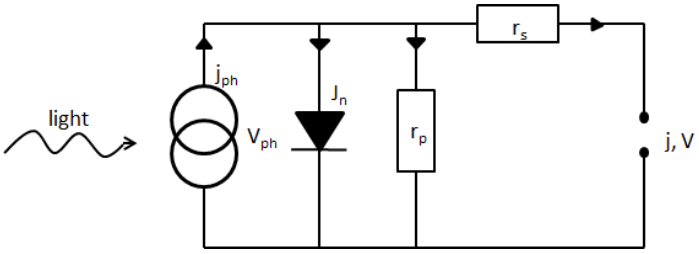

Figure 2.3. Circuit diagram of the simplified circuit model for a solar cell

The equivalent equation for this model is:

$$j(V) = -j_{ph} + J_n\left[\exp\left(\frac{q\cdot(V - j\cdot r_s)}{k\cdot T}\right) - 1\right] + \frac{V - j\cdot r_s}{r_p} \qquad (2.3)$$

The single diode equation assumes a constant value for the ideality factor n which is a function of voltage across the device. At high voltage, when the recombination in the device is dominated by the surfaces and the bulk regions the ideality factor is close to one. However at lower voltages, recombination in the junction dominates and the ideality factor approaches two. The junction recombination is modeled by adding a second diode in parallel with the first and setting the ideality factor typically to two. In Figure 2.4, J1 and J2 symbolize the saturation current density in the base and the emitter, respectively.

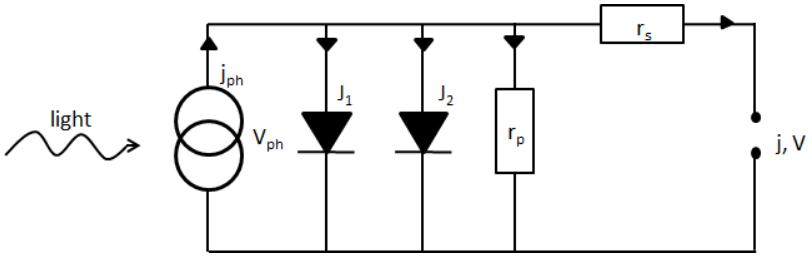

Figure 2.4. Circuit diagram of the double diode model for a solar cell

The equivalent two-diode equation is:

$$j(V) = -j_{ph} + J_1\left[\exp\left(\frac{q\cdot(V - j\cdot r_s)}{n_1\cdot k\cdot T}\right) - 1\right] + J_2\left[\exp\left(\frac{q\cdot(V - j\cdot r_s)}{n_2\cdot k\cdot T}\right) - 1\right] + \frac{V - j\cdot r_s}{r_p} \qquad (2.4)$$

with n_1 and n_2 as the ideality factors with values of 1 and 2 respectively, J_1 the dark saturation current density in the emitter, and J_2 the dark current density in the base.

Double diode model has limitations. In actual silicon devices the recombination components are a complex function of the carrier concentration. For example, in high efficiency PERL (Passivated Emitter Rear Locally diffused) solar cells, as the number of carriers increase with the applied voltage, the recombination at the rear surface changes dramatically with voltage. In such cases, the analysis is best performed by a single diode, but allowing both the ideality factor and the saturation current to vary with voltage. In such cases, which are quite common in silicon devices, a double diode fit yields erroneous values.

2.2. Loss mechanisms in Solar Cells

2.2.1. Optical losses

Optical losses are due to light that cannot generate electron-hole pairs because it is reflected on the front surface of the solar cell or it is not absorbed by the cell. Ideally, all the visible light should be absorbed by the silicon solar cells because the visible spectrum has enough energy to create electron-hole pairs in this semiconductor. In a solar cell, optical losses affect to the generated photocurrent, diminishing it and causing an efficiency loss.

There are many ways to reduce the optical losses, like increasing the thickness of the cell so that the absorption can be improved due to the optical path enhancement, minimizing the front metallic contact surface or some schemes of light trapping [4], but the most used in photovoltaic industry is the surface texturing and the ARCs (anti-reflection coatings).

2.2.1.a) Surface texturing

Surface texturing can be used to minimize reflection, either in combination with an anti-reflection coating or by itself. Any surface roughness reduces reflection by increasing the chances of reflected light bouncing back onto the surface, rather than out to the surrounding air (Figure 2.5).

A single crystalline substrate can be textured by etching along the faces of the crystal planes. The texturing called *random pyramid textur*e is widely used in photovoltaic industry for single crystal wafers [5,6], where the crystalline structure of silicon results in a surface made up of pyramids.

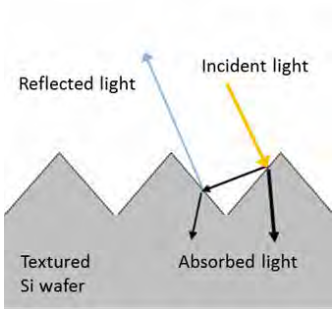

Figure 2.5. The surface texturing reduces the reflection of the incident light.

2.2.1.b) Anti-reflection coatings (ARCs)

ARCs on solar cells consist of a thin layer of dielectric material, with a specifically chosen thickness so that interference effects in the coating cause the wave reflected from the anti-reflection coating top surface to be out of phase with the wave reflected from the semiconductor surfaces. These reflected waves interfere destructively with another, resulting in zero net reflected energy.

Regarding the thickness of the ARC, it is chosen so that the wavelength in the dielectric material is one quarter the wavelength of the incoming wave. This thickness (d_1) is calculated from the relationship between the refractive index of the dielectric layer (n_1) and the wavelength related to the minimum reflection (λ_{min}):

$$d_1 = \frac{\lambda_{\min}}{4\, n_1} \tag{2.5}$$

To determine the refractive index of the ARC, the refraction indexes of the materials of both sides (silicon and air) should be taken account. Then, reflection is minimized if the refractive index of the anti-reflection coating is the geometric mean of that of the materials on either side:

$$n_1 = \sqrt{n_0 n_2} \tag{2.6}$$

being n_0, n_1 and n_2 the refractive index of air, the deposited coating and silicon, respectively.

The refractive index is dependent on wavelength; then, zero reflection occurs only at a single wavelength. For photovoltaic applications, the refractive index and therefore thickness are chosen in order to minimize reflection for a wavelength of 600 nm [7]. This wavelength is chosen since it is close to the peak power of the solar spectrum. On the other hand, if more than one anti-reflection coating was used, the reflection could be reduced in a wider wavelength, but this process would raise the price of the solar cell production and does not compensate the obtained benefit [8].

Examples of ARCs in silicon solar cells are silicon nitride [9,10], porous silicon [11,12], TiO_2 [13], porous silicon/SiO_x [14] or stacks of SiO_2/TiO_2 [15] among others.

2.2.2. Resistance losses

Series and parallel resistance losses diminish the fill factor and the net efficiency of the solar cell. Series resistance is usually controlled by the front contact design and the emitter resistance. These losses produced by series resistance (r_s) and parallel resistance (r_p) can be modelled on an equivalent circuit as shown in Figure 2.3.

Efficiency losses are produced due to these resistances, where the open circuit voltage is affected mainly by parallel resistance (the lower r_p value the higher loss).

2.2.3. Recombination losses

Usually, the recombination processes of charge carriers are defined as the reverse processes of their generation. In dark conditions, the thermal-equilibrium condition of a semiconductor can be disturbed by lighting the device, increasing of this way the charge carrier concentration throw the generation of electron-hole pairs [16]. After generation, the carriers have the tendency to return to their original state of equilibrium by the so-called recombination. Summing up, there are two mechanisms to disturb the equilibrium-condition: the recombination process of the electron-hole pairs (detrimental) and the thermal generation through photon illumination (required).

There are three basic types of recombination in the bulk of a single-crystal semiconductor: radiative recombination, Auger recombination and Shockley-Read-Hall (SRH) recombination. All of them are related by the following expression:

$$\frac{1}{\tau_{bulk}} = \frac{1}{\tau_{rad}} + \frac{1}{\tau_{Auger}} + \frac{1}{\tau_{SRH}} \tag{2.7}$$

Radiative (band-to-band) recombination

In radiative recombination, an electron from the conduction band directly combines with a hole in the valence band releasing the excess energy as a photon. This emitted photon has a similar energy to the band gap and therefore is only weakly absorbed. This process, reverse of the absorption, is less probable in indirect-bandgap (E_g) semiconductors like silicon than in a direct one, therefore under most circumstances, radiative recombination is a small proportion of the total recombination, with most recombination being non-radiative, taking place at point defects or at grain boundaries.

Auger recombination

This type of recombination involves three carriers. After an electron-hole recombination, the energy is supplied to a third carrier (an electron in the conduction band) instead being emitted as heat or as a photon. This electron then thermalizes back down to the conduction band edge. Auger recombination is more important at high carrier concentrations due to heavy doping or high level injection under concentrated sunlight. In silicon solar cells, this recombination limits the carrier lifetime and therefore the cell efficiency.

Shockley-Read-Hall recombination

Defects caused by impurities (incorporated in the bulk material during crystal growth), doping, wafer processing, and so forth, can act as recombination centers located within the bandgap [16]. The SRH recombination process is the predominant recombination process in Si bulk devices [17].

The three recombination types in the bulk of a single-crystal semiconductor are depicted in Figure 2.6.

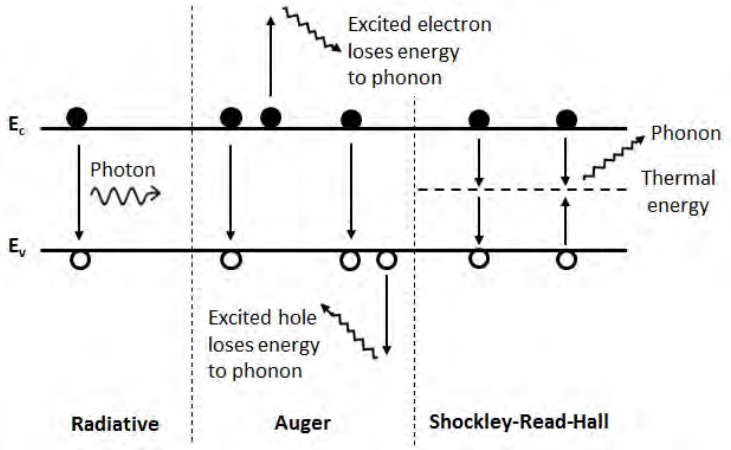

Figure 2.6. Recombination process in the bulk of a single-crystal semiconductor.

2.3. Contact resistance

Transmission Line Measurement (TLM) has been used in photovoltaic research for many years to determine the contact resistance between metal and semiconductor as well as sheet resistance of the semiconductor layer [18]. The method consists in contacting two metal pads with probes which apply a current between the contact pads and measure the voltage drop at the same time [19].

In this work, TLM was carried out in order to analyze the resistance of the rear contacts screen-printed or inkjet-printed on silicon wafers, with different aluminum pastes after the firing at different conditions in a tubular fast oven. A scheme of the method used for the samples studied in this thesis is depicted in Figure 2.7.

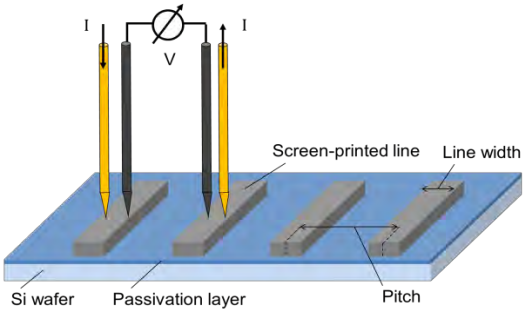

Figure 2.7. TLM scheme for the printed aluminum lines.

After measuring the samples, the contact resistance can be determined from a chart R = f(d). In Figure 2.8, this type of chart is represented for contacts made of aluminum lines of 1 mm width and 11 mm large. The interception of the curve with the ordinate corresponds to $2R_c$. The specific contact resistance ρ_c was calculated according to the condition $L_t<L$, where L_t is the transfer length, L the width of the line and k the length of the line:

$$\rho_c = R_c k L \ [\Omega\ cm^2] \tag{2.8}$$

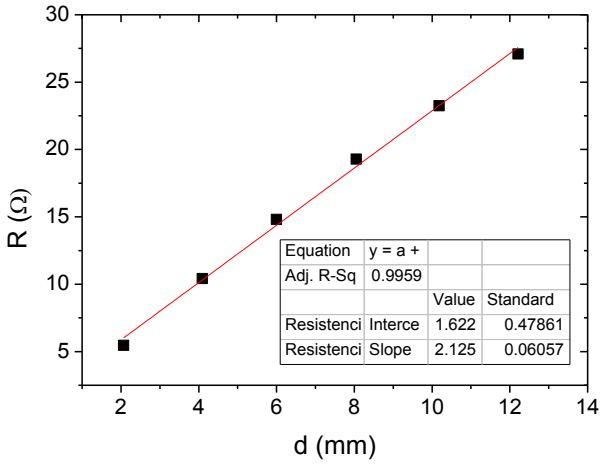

Figure 2.8. Typical graphic method used to determine the contact resistance.

2.4. Carrier lifetime

To study the quality of the passivation and antireflection layers, it is necessary to measure the carrier lifetime, which is the most important electronic property of semiconductor materials for solar cells. It is the average time that electrons and holes can move before a recombination process. The recombination rate is given by $\Delta n/\tau$, where τ is the carrier lifetime, and Δn is the excess carrier concentration.

In order to understand practical measurements of the carrier lifetime, it is essential to realize that usually it is measured relatively thin slices of material and, therefore, we should expect that the surfaces of the wafer may play an important role in the global recombination processes that it is being measured [20]. At the surface of the silicon wafer, electron and holes can recombine at a speed characterized traditionally by the *surface recombination velocity S*, which is directly proportional to the corresponding recombination rate U and also to the excess carrier concentration Δn. The concepts of S and τ_{eff} have opposite meanings: a high lifetime means a low recombination rate, whereas a high S implies a high recombination rate. Measurements of the effective carrier recombination lifetime τ_{eff} of silicon wafers have extensively been used for process and device optimization.

What it has been said about the lifetime can be extended to the surface recombination velocity. For determining the carrier lifetime by the photoconductance method, there are basically two possibilities [20]:

1. **Transient decay photoconductance (PCD).** It consists in stopping the excitation abruptly and measure the rate at which carriers disappear as time passes by. In practice, this method is generally used for measuring carrier lifetimes over 200 μs. The effective carrier lifetime of the transient method is deduced from

$$\frac{d\Delta n(t)}{dt} = -U(t) = -\frac{\Delta n(t)}{\tau_{eff}} \tag{2.9}$$

   and it is

$$\tau_{eff} = -\frac{1}{\frac{1}{\Delta n(t)}\frac{d\Delta n(t)}{dt}} \tag{2.10}$$

2. **Steady-state photoconductance (SSPC).** For determining the carrier lifetime through this method, a steady-state generation rate of known value is maintained. In practice, this method is generally used for measuring carrier

lifetimes up to 200 µs. The net recombination rate *U(t)* equals the generation rate *G(t)*, so that the effective carrier lifetime can be determined by definition:

$$G(t) = U(t) = \frac{\Delta n(t)}{\tau_{eff}} \quad ; \quad \tau_{eff} = \frac{\Delta n(t)}{U(t)} = \frac{\Delta n(t)}{G(t)} \tag{2.11}$$

- **Quasi-steady-state photoconductance (QSSPC).** The intensity of illumination varies with time in a gradual way. For quasi-steady-state measurements, the user selects the longest available time constant of the flash lamp. This method is the one used in this thesis to determine the carrier lifetime, so that it is detailed in the next section.

2.4.1. QSSPC method

The experimental set-up used in this thesis (Figure 2.9) for determining the effective lifetime was fabricated by Sinton Consulting. The conductivity of the wafer is measured inductively by a coil and an oscillator circuit, whereas the excess carrier density is excited by a flash lamp, the intensity of which is tracked by a reference cell. Approximate light sources are photographic flashes that, in combination with attenuating filters, can produce irradiance levels from nearly 1000 to 10^{-5} suns. A reference solar cell and oscilloscope are used to determine the time dependence of the excess photoconductance of the test sample and its illumination.

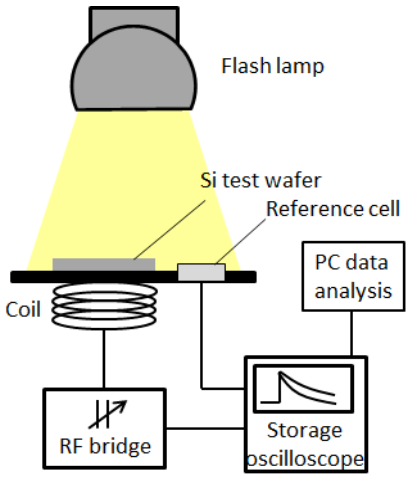

Figure 2.9. Scheme of measurement principle of QSSPC.

The QSSPC technique allows to measure low lifetimes and to calibrate the equipment to know the injection level.

The effective lifetime can be calculated by the following expression [21]:

$$\tau_{eff}(\Delta n) = \frac{\Delta n\,(t)}{G(t) - \frac{d\Delta n(t)}{dt}} \tag{2.12}$$

To determine the effective lifetime from this definition, it is thus required to measure the time dependence of the excess carrier density and the generation rate within the reference sample.

The excess carrier concentration is given by:

$$\Delta n(t) = \frac{\Delta\sigma(t)}{q(\mu_n + \mu_p)W}, \tag{2.13}$$

where $\Delta\sigma(t)$ is the variation of conductivity with time, W the sample thickness and μ_n and μ_p the mobility of electrons and holes, respectively, which are dependent on the dopant density and injection level [22].

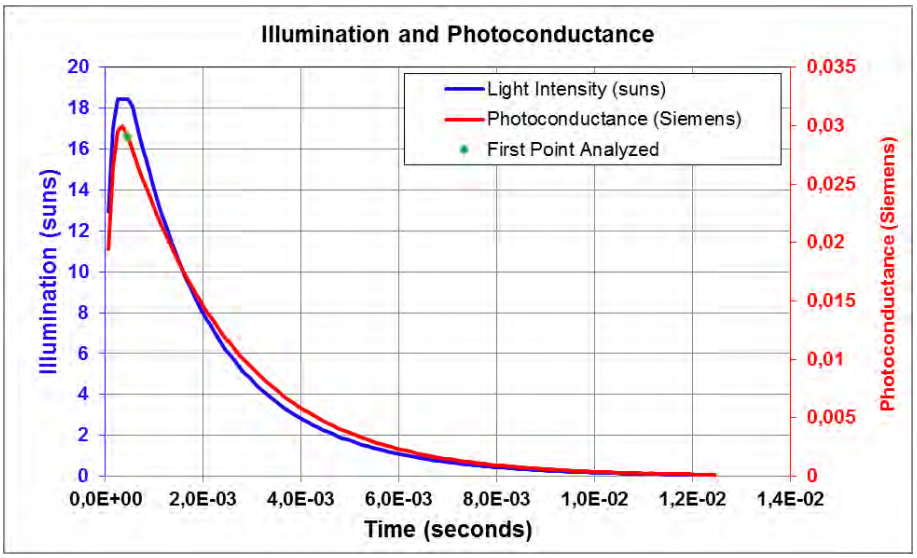

Figure 2.10. QSSPC measurement for a SiO_2 layer on silicon, where lifetime was 40 µs.

The illumination intensity I(t) measured from the solar cell is usually quoted in suns (1 sun=1 kW m^{-2}) as can be observed in Figure 2.10. It is a measure of the number of photons incident on the sample surface. Then, the generation rate within the sample can be determined as:

$$G(t) = \frac{I(t) f_{abs}\, N_{ph/1sun}}{W}, \tag{2.14}$$

where f_{abs} is the optical absorption fraction of the sample to take into account reflection and transmission losses, and $N_{ph/1sun}$ is the density of photons in solar light with an irradiance of 1 sun, with an energy greater than the silicon bandgap.

2.4.2. Surface saturation current density

Wafers usually have dopant diffusions on their surfaces. The best way to consider the effect of these diffused (or emitter) regions is by means of the parameter called the surface saturation current density, J_{0s}. A direct measurement of the surface recombination velocity S and surface saturation current density J_{0s} is not possible. It is, however, possible to measure the effective minority carrier lifetime τ_{eff}, which takes into account the recombination mechanisms at the surface of the measured sample as well as within its bulk. In the following sections, the formulas refer to n-type silicon (doping concentrations of atoms are donors N_D) and Δn is used for the excess carrier density.

Under low-level injection ($\Delta n << N_D$)

When symmetrical samples are processed that allow a QSSPC measurement, τ_{eff} can be determined and related to S_{eff} [3]. Considering a n-type Si sample of thickness W and dopant density N_D, the inverse effective lifetime is the following:

$$\frac{1}{\tau_{eff}} = \frac{1}{\tau_{bulk}} + \frac{1}{\tau_s} = \frac{1}{\tau_{bulk}} + \left[\frac{W}{2\, S_{eff}} + \frac{1}{D_{min}} \left(\frac{W}{\pi}\right)^2\right]^{-1} \tag{2.15}$$

Relating S_{eff} to the surface saturation current density J_{0s}:

$$S_{eff} = J_{0s}\, \frac{\Delta n + N_D}{q\, n_i^2} \tag{2.16}$$

Under low-level injection Δn can be neglected and J_{0s} can be expressed as follows:

$$J_{0s} = \frac{q\, n_i^2\, W}{2\, N_D} \left[\left(\frac{1}{\tau_{eff}} - \frac{1}{\tau_{bulk}}\right)^{-1} - \frac{1}{D_{min}} \left(\frac{W}{\pi}\right)^2\right]^{-1} \tag{2.17}$$

Under high-level injection ($\Delta n >> N_D$)

For low surface recombination velocities, the term corresponding to D_{min} (diffusion constant of minority carriers) can be neglected from the Equation (2.15). Under high-level injection with Equation (2.16) the relation appears as follows:

$$\frac{1}{\tau_{eff}} = \frac{1}{\tau_{bulk}} + \frac{S_{front}}{W} + \frac{J_{0s}}{q\, n_i^2\, W}\, \Delta n \tag{2.18}$$

with an assumed injection-independent S_{front} and an injection-dependent rear side. Then, $1/\tau_{eff}$ is linearly dependent on Δn, with a slope *s* according to the slope method first proposed by Kane et al. [23] from which J_{0s} can be extracted:

$$s = \frac{J_{0s}}{q\, n_i^2\, W} \tag{2.19}$$

For each carrier density Δn, τ_{eff} can be corrected by the intrinsic lifetime τ_{int} ($\tau_{int}^{-1} = \tau_{Aug}^{-1} + \tau_{SRH}^{-1}$) to $\tau_{eff,corr}$, using models for calculating the radiative [24] and Auger recombination [25], leading to the formula:

$$\frac{1}{\tau_{eff,corr}} = \frac{1}{\tau_{eff}} - \frac{1}{\tau_{intr}} = \frac{1}{\tau_{SRH}} + \frac{S_{front}}{W} + \frac{J_{0s}}{q\, n_i^2\, W}\, \Delta n \tag{2.20}$$

where by the slope *s* of the function, J_{0s} can be calculated.

2.5. Back surface field and local back surface field

Surface recombination have a detrimental impact on the short-circuit current and on the open-circuit voltage. At the top of the surface, high recombination rates have special impact on the short-circuit current, since top surface also corresponds to the region of highest carriers generation in the solar cell. To decrease the high top surface recombination the number of dangling silicon bonds at the top surface must be reduced by using a passivating layer on the top surface. With this purpose, electronics industry usually relies on the use of a thermally grown silicon dioxide layer to passivate the surface due to the low defect states at the interface [26.]. But for commercial solar cells, silicon nitride is commonly used as dielectric layer.

Under the top surface contacts the effect of the surface recombination can be diminished by increasing the doping. A back surface field consists of a higher doped region at the rear surface of the solar cell. In both cases, between the high and low doped regions there is an interface which behaves like a p-n junction. There, an electric field is formed and introduces a barrier to minority carrier flow to the rear

surface (Figure 2.11). In 1963 it was proposed to do that with the introduction of a *drift field* caused by non-uniform doping of the bulk p-base material [27]. Later developments, however, have been shown that a *p-p+* junction at the back of the cell are far easier to implement than non-uniform doping through the bulk of the device. The *p-p⁺* junction creates a strong electric field in the same direction that of the *n-p* junction.

With the reduction of solar cells thickness, back surface field becomes more and more interesting in order to decrease the back surface recombination velocity and to increase collection efficiency. Screen-printed aluminum-doped *p*-type (Al-*p⁺*) regions formed on crystalline silicon wafers are mainly used as back surface field in *p*-type crystalline silicon solar cells [28-30].

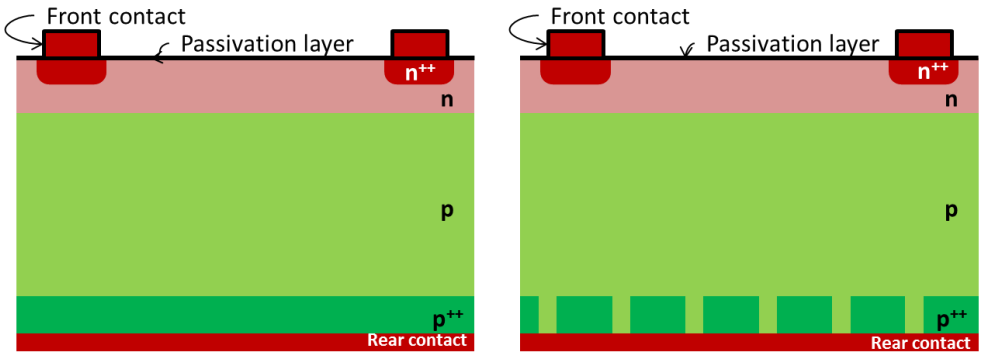

Figure 2.11. p-type silicon solar cell with BSF (left) and LBSF (right).

Summing up, to avoid a high surface recombination rate:

- A good surface passivation is required.
- Heavy doping under contacts keeps minority carriers away from high recombination front contact.
- Heavy doping at rear of cell keeps minority carriers (electrons in this case) away from high recombination rear contact.

The aluminum BSF starts during the process of formation of front and rear contacts. The steps of the process are described in the following points and depicted in Figure 2.12.

a. The aluminum paste is composed of aluminum particles with diameters from 1 to 10 µm, metal oxides, organic agglutinant and solvents. The firing process starts with the burning out of organic solvents from the paste.

b. Because of the fact that temperature is high and there is an oxygen containing atmosphere, the aluminum oxide shells of the particles are thickened. The particle matrix is then stabilized and not destroyed during the firing process [31]. Aluminum melts at 660ºC and dissolves silicon from the surface to form a liquid Al-Si-phase with a temperature dependent percentage of silicon related to the liquidus curve L(T) of the phase diagram (Figure 2.13).

c. While temperature is increasing, more amount of silicon is dissolved in the liquid Al-Si phase. To compensate the process, aluminum diffuses into the wafer surface.

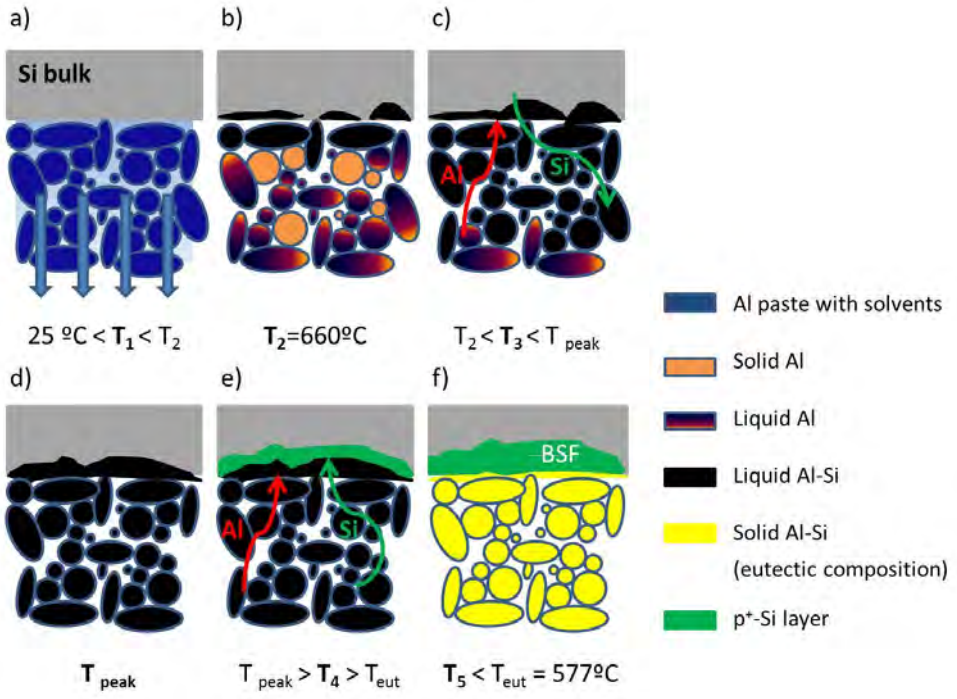

Figure 2.12. Scheme of the alloying process described in the text.

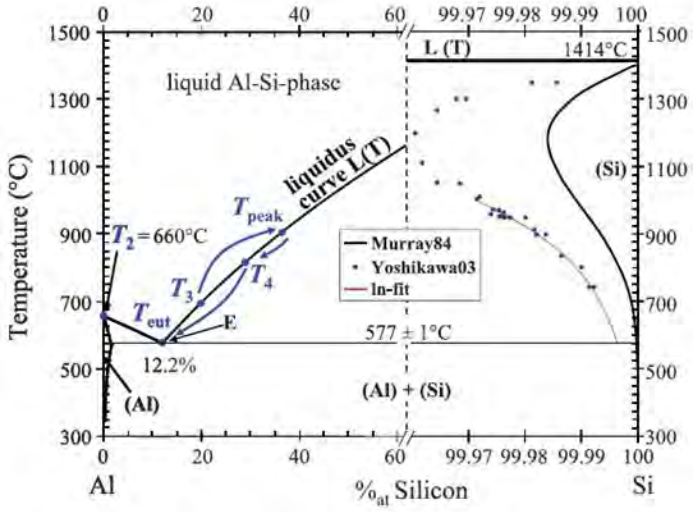

Figure 2.13. Al-Si binary phase diagram [32].

d. At peak temperature (T_{peak} in Figure 2.12), the maximum concentration of silicon in the liquid phase is reached (almost the 40% of liquid phase is silicon) and so the maximum amount of dissolved silicon. Therefore the weight of dissolved silicon $m_{Si,dis}$ and the corresponding thickness $d_{Si,dis}$ can be calculated with the weight of deposited aluminum m_{Al} according to [33]:

$$d_{Si,dis} = \frac{m_{Si,dis}}{A\rho_{Si}} = \frac{m_{Al}}{A\rho_{Si}} \frac{L(T_{peak})}{100 - L(T_{peak})} \tag{2.21}$$

where A is the printed area, ρ_{Si} the density of silicon and L(Tpeak) the percentage of Si in the liquid Al-Si phase at peak temperature T_{peak}.

e. Cooling process is the opposite of step c. While cooling down, Si is rejected from the liquid phase and crystallizes at the liquid-phase/silicon interface. According to the solid solubility (Figure 2.13 right), which decreases with falling temperature in the relevant temperature range, Al atoms are incorporated into the Si lattice. Because of that, the peak doping concentration is situated at the former liquid-phase/ silicon interface with decreasing doping concentrations in direction to the final surface of the p^+-layer.

f. When the eutectic temperature (T_{eut}) of 577ºC is reached, the remaining liquid phase solidifies in a short time, being (theoretically) the silicon weight percentage of this mixture 12.6%. Therefore, a called 'eutectic layer' remains between the surface of the p^+-layer and the paste matrix, consisting of nearly pure aluminum and about 12.6% (weight) in the typical lamella structure [34] of eutectic alloys. The porous

layer of paste particles at the external surface (paste residuals) consists of a solid Al–Si mixture.

This eutectic layer becomes important due to two main reasons:

- The rear inner reflectivity of the PV cell depends on this layer.
- The bowing of the PV cell depends on this layer thickness.

Regarding the bowing of the wafers (Figure 2.14), it is mainly produced when thin wafers are used with the aim to reduce costs. The thinner the wafer is the more susceptible is to bowing caused by the influence of the metallization on the front and the rear side caused by the screen printing of aluminum pastes.

With the aim to reduce the bowing, local back surface fields can be applied creating local metal contacts. To form these local metal contacts, the dielectric layer used to passivate has to be locally removed before the Al screen printing, by techniques such as laser or chemical etching. But there is another alternative which is the fire through contact method studied in this thesis. This method allows the p^+-layer formation without the necessity of including any step of laser or chemical etching in the process. The Al-Si diffusion is reached after the firing of the aluminum structures printed directly on the passivating layer.

Figure 2.14. Bowing of the wafers.

2.6. Printing technologies

In this work, two techniques were used to create the back surface field on p-type crystalline silicon wafers with aluminum pastes: screen printing and drop on demand. While the first one is widely applied by the photovoltaic industry, the second one is quite new and only used with the purpose of creating front contacts with silver pastes.

2.6.1. Screen printing

Screen-printed solar cells were first developed in the 1970's and they currently dominate the market for photovoltaic modules. Related to PERC solar cells, the full area BSF is replaced by a dielectric passivation, which normally is locally opened for contact formation. These rear contacts are formed by physical vapor deposition (CVD) of Al or screen printed Al [35-37].

The key advantage of screen-printing is the relative simplicity of the method. This process is shown in Figure 2.15. First of all, a pattern is photographically defined on a screen (in the industry it is used normally a stainless steel mesh for metallization process) by means of an emulsion layer which has been tailored for solvent resistance, durability and exposure characteristics. The consistence of the material to be screen printed is a very important factor to have in mind, and depending on it, the screens can change. A squeegee is used to move the paste through the patterned screen to deposit onto the silicon wafer. The squeegee provides shear stress to the paste to reduce viscosity and allows it to flow through the screen.

After printing, the printed wet film is dried at certain temperature and time, both dependent on the properties of the paste.

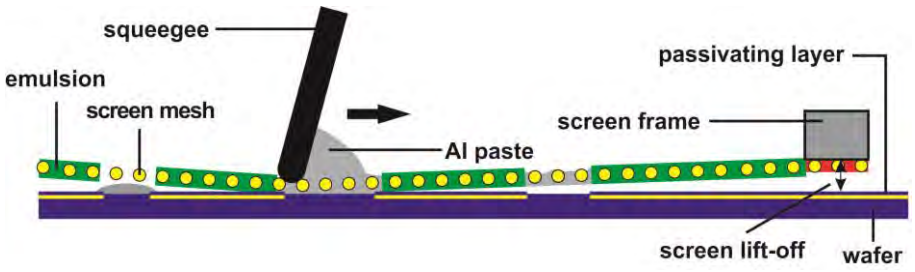

Figure 2.15. Screen-printing scheme for aluminum structures.

Important screen printing parameters are the mesh number of the screen (number of meshes per inch), the distance between the screen and the substrate and the pressure and speed of the squeegee.

In this work, screen-printing has been used to create aluminum structures on silicon wafers with the aim to form the eutectic layer and the BSF. Therefore different layouts were designed (see Appendix B).

2.6.2. Drop on demand (dispensing technology)

Dispensing technology offers an alternative to screen printing according to metallization process. It has the advantage of forming contacts without mesh marks and paste spread. Moreover, thin silicon wafers are a way to reduce costs in the raw material, but the bowing of such wafers after metallization causes its breaking in most of the cases and also *microbreaks* in the structure affecting to the lifetimes and to the efficiency of the final solar cell. This effect can be reduced by using non-contact metallization techniques like dispensing technology as many authors reported for obtaining the front electrodes with silver paste [38-41]. Since the contact formation process remains the same, screen printing pastes only require minor adaptation to be suitable for dispensing technology.

On the other hand, the application of this technique to form the BSF in silicon solar cells was not used as far as it is known. In this work, this technique was applied for that aim using different aluminum pastes which were also suitable for screen printing process. A scheme of the used equipment is depicted in Figure 2.16.

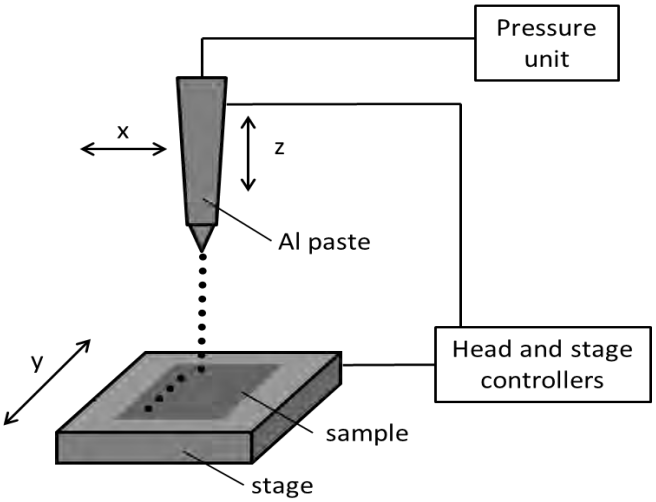

Figure 2.16. Scheme of the dispensing equipment.

2.7. Thin film deposition methods

Thin films were created on silicon in this thesis to analyze the interfaces and study the quality of the passivation. Two thin films deposition techniques were used: PECVD and magnetron sputtering.

2.7.1. Plasma enhanced physical vapor deposition (PECVD)

PECVD is an excellent alternative for depositing films for solar cells passivation at lower temperatures than those utilized in CVD reactors, without settling for a lesser film quality. For example, for silicon dioxide films, much higher temperatures are necessary using CVD to produce similar quality films. This technique is widely used in the photovoltaic industry to create SiN_x and Al_2O_3 layers for passivating the solar cells surface and then enhance the efficiency [42, 43], but also for SiO_x or SiN_x antireflection coatings [44,45].

PECVD uses electrical energy to generate plasma in which the energy is transferred into a gas mixture. This transforms the gas mixture into reactive radicals, ions, neutral atoms and molecules, and other highly excited species. These atomic and molecular fragments interact with a substrate and, depending on the nature of these interactions, either etching or deposition processes occur at the substrate. Since the formation of the reactive and energetic species in the gas phase occurs by collision in the gas phase, the substrate can be maintained at a low temperature. Some of the desirable properties of PECVD films are good adhesion, low pinhole density, good step coverage, and uniformity.

In this work, PECVD technique was used to deposit thin films composed by silicon nitride and silicon rich oxy-nitride at Fraunhofer ISE and Isofoton S. A.

2.7.2. Magnetron sputtering

Sputtering is commonly used for thin-film deposition apart from etching or analytical techniques [46]. It is widely used in the photovoltaic industry to grow amorphous silicon (a-Si:H) for passivating surfaces [47]. This is a process based in the intense bombardment of a material (target) with the ions created in plasma. Therefore, atoms are ejected from that target and deposited on the substrate (see Figure 2.17).

The target material and the substrate are placed in a vacuum chamber. A voltage is applied between them being the target the cathode and the substrate attached to the anode. Then, plasma is created by ionizing a sputtering gas (Argon in this work), the sputtering gas bombards the target at high energies and sputters off the desired material to deposit. This process is called *diode sputtering*.

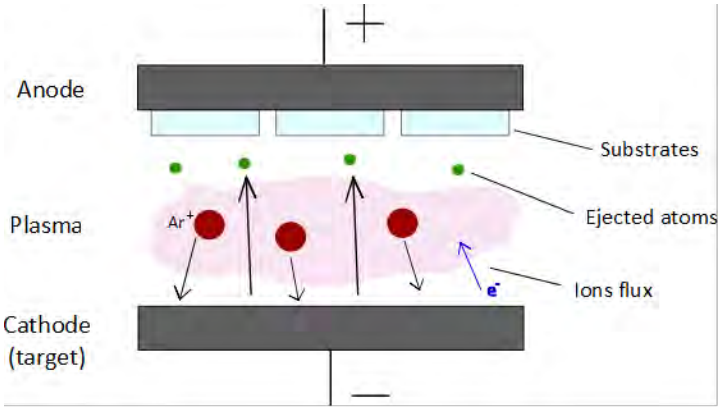

Figure 2.17. Scheme of diode sputtering process.

On the other hand, diode sputtering has two major problems: the deposition rate is slow and the electron bombardment of the substrate is extensive and can cause overheating and structural damage. The development of *magnetron sputtering* copes with both of these problems simultaneously. Using magnets behind the cathode allows trapping the free electrons in a magnetic field directly above the target surface (Figure 2.18). Then, these electrons are not as free to bombard the substrate as in diode mode. Moreover, the extensive, circuitous path carved by these electrons when trapped in the magnetic field, improve their probability of ionizing a neutral gas molecule by several orders of magnitude. This increase in available ions significantly increases the rate at which target material is eroded and subsequently deposited onto the substrate.

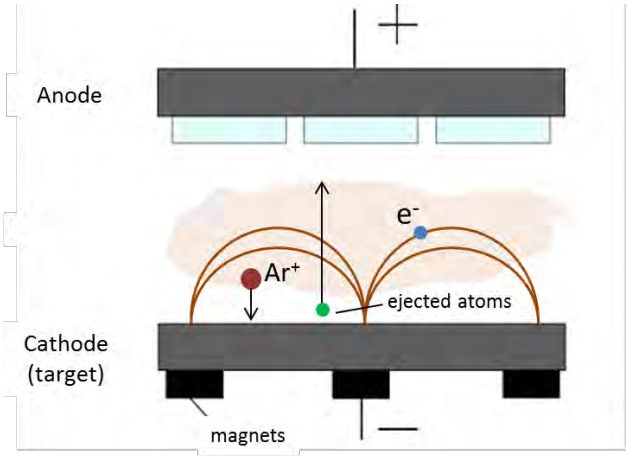

Figure 2.18. Scheme of magnetron sputtering process.

In this thesis, magnetron sputtering has been used to create thin films of silicon nitride, aluminum oxide and zinc oxide on p-type monocrystalline silicon wafers at different parameters of temperature, pressure and power supply.

3

Thin films on silicon

In this chapter, dielectric passivation layers were created by diverse techniques of thin films deposition. Lifetimes were extracted for layers obtained by PECVD and the study of the interface and morphology was done for the layers grown by magnetron sputtering.

3.1. Introduction

Dielectric passivation layer (or layers) on the rear side surface is as essential as in the front side to minimize recombination losses. It has to be enough thick to allow high carrier lifetime and therefore low saturation current densities, like was theoretically explained in section 2.4. These layers require low back-surface recombination velocity (BSRV) and work as optical back-surface mirrors, producing high internal reflectance [48]. There were deposited different types of layers by thermal oxidation and PECVD on p-type silicon wafers (Figure 3.1). After that, the carrier lifetime τ and saturation current density J_0 were measured and compared using the QSSPC technique (see section 2.4.1).

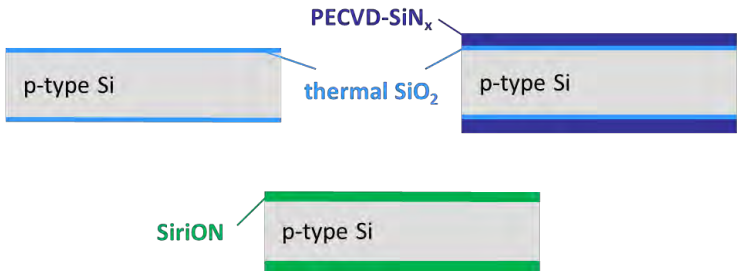

Figure 3.1. Some types of passivation layers obtained in this chapter.

Alumina films have been deposited by various technologies in bibliography, such as plasma-enhanced chemical vapor deposition [49], atomic layer deposition (ALD) [50] or metal organic chemical vapor deposition [51]. On the other hand, the most used technique to grow SiN_x layers is PECVD [52]. Al_2O_3/SiN_x stacks have been usually prepared by PECVD and ALD in the photovoltaic industry [53-55], and a considerable improvement related to the thermal stability during firing is achieved for the stacks compared to a single Al_2O_3 layer [56]. But recently, sputtering technique is used in greater range. In fact, it seems to be a promising technique due to several intrinsic advantages over the PECVD process, such as elimination of toxic gases, low operating temperature, low cost, flexibility of sequential deposition, simple regulation of the deposition rate and finally a simpler deposition system. Moreover, the classical ALD systems use to have very low deposition rate. The process parameters, such as deposition temperature, work pressure and gas flow can be easily modulated in order to get solid thin films with the magnetron sputtering. Low temperatures during film preparation also allow the implementation of a large variety of substrates and open the possibility of using Al_2O_3/SiN_x based materials as transparent films in flexible devices. On the other hand, SiN_x films deposited by PECVD are currently the industrial standard for ARCs (antireflection coatings) on crystalline silicon substrates [57.58].

But this method is a high cost chemical process in spite of its layer uniformity, high precision and high rates of deposition.

The knowledge of the Al_2O_3/SiN_x nanostructured interface is important to determine the possible applications of the films, but most of the works related to these stacks simply quantify the lifetime to describe the quality of the passivation on silicon. In this chapter, the comparison among single layers of Al_2O_3 and SiN_x with stacks of Al_2O_3/SiN_x prepared on Si <100> by magnetron sputtering under room temperature is presented, correlating the interfaces (thickness) and changes in the optical properties with the microstructure variations induced by the deposition time. A large number of characterization techniques have been used in order to fully understand the behavior of both single layers and stacks.

Zinc Oxide (ZnO) has deserved much attention during the last years since it is a promising material in solar cell applications requiring antireflection coatings and transparent conducting materials for front contacts [59]. The doping of ZnO with group III elements, like Al and Ga, has emerged as a way to obtain a promising high quality transparent conductive oxide (TCO) [60]. Its high carrier concentration and wide optical band gap energy of 3.37 eV has made it a suitable material for thin film solar cells [61], heterojunction solar cells [62,63], optoelectronic devices and for the next generation of UV light emitting diodes due to the large exciton binding energy (~60meV), which allows efficient excitonic emission at room temperature [64-66]. Moreover, its nanostructures have attracted great attention as a promising functional material. Focusing on the transparency and conductivity of the AZO (Al-doped ZnO) films, they are being used in photovoltaic industry as TCO for heterojunction solar cells, being these layers an alternative to other TCO studied like the ITO [67]. In this work, undoped ZnO and Al:ZnO films are deposited onto silicon wafers and glass by magnetron sputtering with the aim to analyze the layers as TCO for heterojunction silicon solar cells.

3.2. SiO_2 thermal oxidation

To achieve a good passivation with dielectric layers made by thermal oxidation, a highly clean surface is required. Thin silicon dioxide films, thermally grown into silicon surfaces as dielectric passivation layer, have been used since the integrated circuits industry began in the early 60's [48].

There are two main ways to carry out the thermal growth of SiO_2: wet and dry oxidation. During the wet oxidation of the silicon, the wafer is under water vapor

atmosphere. Wet oxides speed grown is rather higher than dry oxides, being this the major advantage, following the chemical reaction:

$$Si\ (s) + 2\ H_2O\ (g) \rightarrow SiO_2\ (s) + 2\ H_2$$

Due to its water content, wet oxide films exhibit a lower dielectric strength and more porosity to impurity penetration than dry oxides. Therefore, wet oxidation is used when the electrical and chemical properties of the film are not critical.

Comparing with wet oxidation, dry oxidation provides a high quality silicon dioxide. This last method was used in this thesis to study SiO_2 and SiO_2/SiN_x layers for rear surface passivation of solar cells. The oxidation process temperature was 840°C for 5 min, with a successional post oxidation anneal for 30 min at the same temperature. Before and after the oxidation process the furnace was heating up and cooling down. The oxide layer was grown in a dry atmosphere by pure oxygen as it can be shown in the following reaction:

$$Si\ (s) + O_2\ (g) \rightarrow SiO_2\ (s)$$

The growth of a thin SiO_2 layer consumes only a few nanometers of the silicon surface with a thickness approximated to 45 % of the thickness of the SiO_2 layer grown [68]. The growing rate of the oxide depends on the crystal orientation [69].

The thickness of the obtained SiO_2 layer was estimated by ellipsometry, and got a value of 12 nm. The carrier lifetime was 25.55 µs, at a specific minority carrier density (MCD) of 5 10^{14} cm^{-3}. Therefore, the carrier lifetime with only one layer of SiO_2 is too low for a solar cell and it is necessary to add another layer of SiN_x to improve it.

3.3. Layers obtained by PECVD

As it was explained in chapter 2, plasma enhanced chemical vapor deposition is a useful technique to obtain thin and homogeneous films on silicon wafers. In this chapter, silicon nitride and silicon rich oxynitride (SiriON) layers were coated on Cz (Czochralski) p-type monocrystalline silicon wafers with the aim to passivate the surface and decide which layer would be the most suitable for the passivation of the wafer.

Lifetimes were measured just after the passivation, without any step of firing or thermal annealing. All the layers coated in this section 3 were carried out in the PV-Tech laboratories of Fraunhofer ISE during the internship realized there.

3.3.1. SiO_2 thermal oxidation + SiN_x PECVD

With the aim to improve the quality of passivation it was added a capping layer of SiN_x to the previous thermal growth SiO_2 layer. Using PECVD technique, SiN_x deposition was carried out by the chemical reaction between silane (SiH_4) and ionized ammoniac (NH_3) releasing hydrogen:

$$SiH_x\ (g) + NH_x\ (g) \rightarrow SiN_x\ (s) + H_2$$

The thickness of the SiO_2/SiN_x stack was estimated by ellipsometry giving a value of 79.4 nm. The carrier lifetime reached was 38.51 μs at a specific minority carrier density (MCD) of 5 10^{14} cm^{-3}.

3.3.2. SiN_x

SiN_x layers made by PECVD are used as antireflection coating (ARC) for many authors [70,71], but this layers also can act as passivation ones in silicon solar cells [72,73]. In this section, the second utility was studied. There were deposited 96.2 nm of SiN_x on silicon by PECVD. The carrier lifetime reached was 42.65 μs at a specific minority carrier density (MCD) of 5 10^{14} cm^{-3}.

3.3.3. SiriON (silicon-rich oxynitride)

SiriON layers were prepared according to the work developed at Fraunhofer ISE [74], where a PECVD double layer of SiriON capped with SiN_x yielded an excellent thermally stable surface passivation layer system for crystalline silicon:

$$1º)\ SiH_4 + N_2O \rightarrow a\text{-}SiO_xN_y{:}H$$

$$2º)\ SiH_x\ (g) + NH_x\ (g) \rightarrow SiN_x\ (s) + H_2$$

The thickness was estimated by ellipsometry, and got a value of 85 nm. The maximum lifetime was 126.84 μs, measured at the center of the wafer at a specific minority carrier density (MCD) of 5 10^{14} cm^{-3} (Figure 3.2). The minimum was 74 μs, measured at the edge of the wafer.

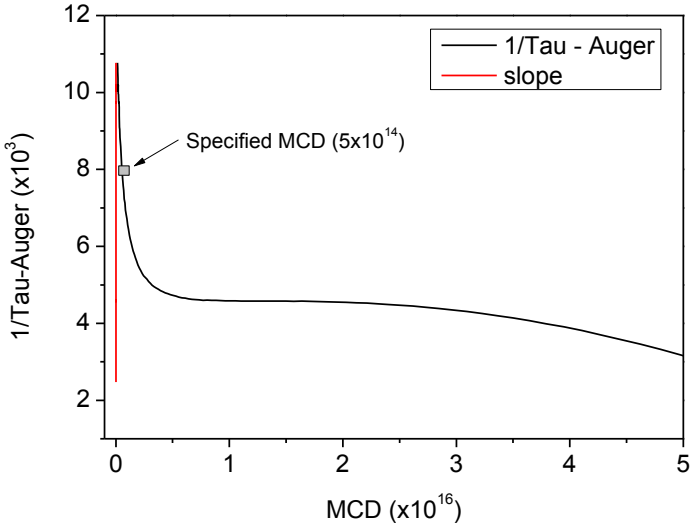

Figure 3.2. Auger corrected inverse lifetime versus minority carrier density (MCD) after SiriON deposition

Comparison

According to the single layers of SiO_2 and SiN_x, it was needed much higher thickness of SiN_x deposited by PECVD to reach similar carrier lifetime than with thermal grown SiO_2 (Figure 3.3). On the other hand, SiriON layers lead to the best passivation results. All the results shown in Table 3.1 and Figure 3.3 were obtained as deposited in QSSPC mode. However a rapid thermal anneal (RTA) is beneficent for the passivation quality, being the effects major in multicrystalline wafers [75].

For the best option for passivation, which was SiriON, FZ (Float Zone) wafers were used to obtain even better results. After deposition, the surface passivation was activated by a high temperature step at a temperature of 880ºC and a rate of 5200 mm/min. Therefore lifetime value was highly improved reaching 1238 µs. After that, the sample was introduced in a furnace to carry out a forming gas annealing and the lifetime then was enhanced to 1477 µs.

	Lifetime at Spec. MCD (µs)	Sheet Resistance (Ω/sq)	Measured Resistivity (Ω-cm)	J0 (A/cm^2)	Doping (cm^{-3})
Thermal SiO_2	26	146	1.70	$-3.8\cdot10^{-13}$	$8.6\cdot10^{15}$
SiO_2/SiN_x	39	135	1.57	$-2.1\cdot10^{-12}$	1.510^{16}
SiN_x	43	135	1.57	$-1.9\cdot10^{-12}$	1.510^{16}
SiriON	127	173	2.01	$-6.6\cdot10^{-13}$	7.210^{15}

Table 3.1. Results obtained from QSSPC measurements for all the layers analyzed in this section.

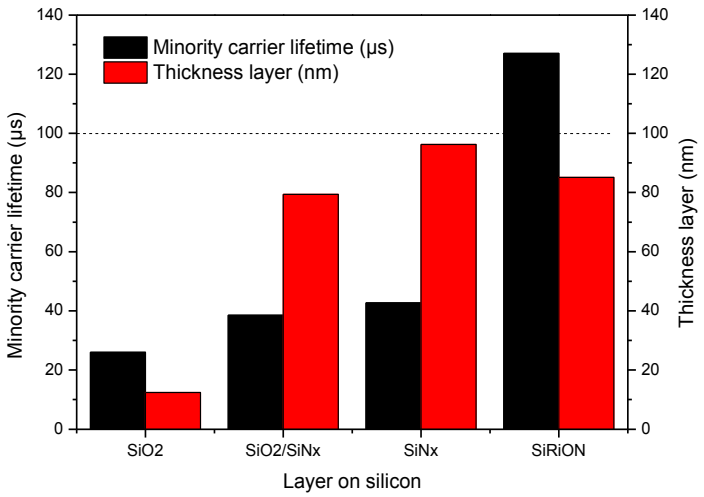

Figure 3.3. Minority carrier lifetime on monocrystalline silicon wafers and thickness of the respective passivation layer

Pictures of the wafers taken after passivation with a light microscope from *Leica* are shown in Figure 3.4 for SiN_x, SiO_2/SiN_x and SiriON layers, where the homogeneity of the surface is confirmed. Wafers got a blue color when oxygen was present during passivation, while the nitride gives a yellow color. Black squares are related to the pyramids formed after texturing.

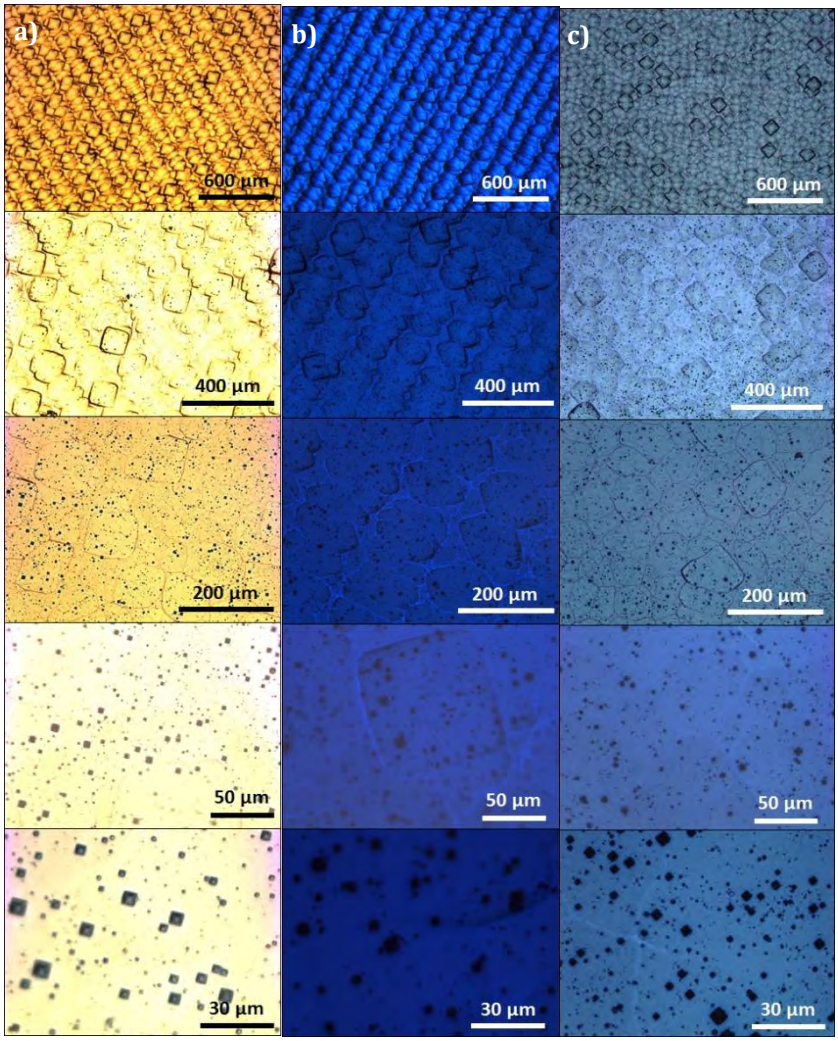

Figure 3.4. Light microscope images of three passivation layers on silicon: SiN_x (column a), SiO_2/ SiN_x (column b) and SiriON (column c).

3.4. Thin films obtained by magnetron sputtering

Silicon nitride and aluminum oxide films have been usually prepared by PECVD, but recently, sputtering technique is being used in greater range in photovoltaic industries. In fact, it seems to be a promising technique due to several intrinsic advantages over the PECVD process, such as elimination of toxic gases, low cost,

flexibility of sequential deposition, simple regulation of the deposition rate and, finally, a simpler deposition system.

Magnetron sputtering has been one of the favorite ways to grow ZnO films because of its low cost, simplicity, and the possibility of working at low temperature. The process parameters like deposition temperature, pressure and doping concentration can be easily controlled in order to get low resistivity TCO films [76]. The preparation of high-quality single crystal ZnO films is also achieved using the appropriate substrate temperature-rf power combination [77]. The relatively low temperatures that can be achieved during the film preparation allow the use of a large variety of substrates and opens the possibility of using ZnO based materials as transparent electrodes in flexible electronics [78].

3.4.1. SiN_x

3.4.1.a) Sample preparation

For the following analysis, <100>-oriented Cz as-cut textured silicon wafers with a resistivity of 1-3 Ωcm and a thickness of 180 μm were used. Furthermore, <100>-oriented Cz polished p-type silicon wafers with a resistivity of 11-25 Ωcm and a thickness of 625 μm were used to carry out SNMS, XRD and ellipsometry measurements. Moreover, glass substrates were also used to carry out the optical measurements. All silicon samples were cleaned in a short HF dip before sputtering process at 150W, room temperature and 12 sccm of Ar flow. Glass substrates were cleaned with propanol and acetone in an ultrasonic bath. A SiN_x ceramic target from *Able Target* was used as source. The work pressure at the main chamber was $1.2 \cdot 10^{-4}$ mbar.

3.4.1.b) Results

Figure 3.5 shows the C 1s, Si 2p, O 1s and N 1s XPS spectra of the SiN_x films obtained by magnetron sputtering during two different times: 30 and 60 minutes. C 1s peak related to the contamination of the sample shows more intensity for the 60 min sputtered sample than for the 30 min one, in spite of the 16 minutes of Ar ions etching carried out for the first one. The same issue was observed for the O 1s peak. Therefore, the signals of the Si 2p and N 1s peaks related to the layer grown during 30 minutes are more intense. For both films deposited during 30 and 60 minutes, Si 2p signal was adjusted at 101.8 eV, typical binding energy of Si in nitrides [79]. Otherwise, N 1s peak was centered at 397.7 and 397.4 eV for samples made during 30 and 60 minutes of magnetron sputtering respectively, characteristic binding energy for silicon nitride. Regarding the O 1s peak, it was centered at 531.8 and 531.4 eV for 30 and 60 minutes samples respectively. It was related to silicon hydroxide [80]. In

Table 3.2, the percentage of atomic concentration is shown for each element. Since hydrogen is not detected, these atomic percentages exclude this element. Obviously, the results also confirm the more amount of oxygen in the sample with more time of SiN_x sputtering deposition. Then, the more time the sample is inside the vacuum chamber while sputtering deposition, the more amount of carbon contamination and oxygen are in the surface. This is associated to the oxygen attached to the wall of the chamber which adds also to the plasma and then contributes to the coated layer too. EDX mappings were carried out to confirm the fact that the oxygen content in the samples was higher as the sputtering deposition time increased (Figure 3.6). In these pictures, it seems that elements are deposited on the right side of the pyramids, but it is caused by the position of the SEM detector. It could be checked turning the samples 180º, and the most amounts of elements were again on the right side.

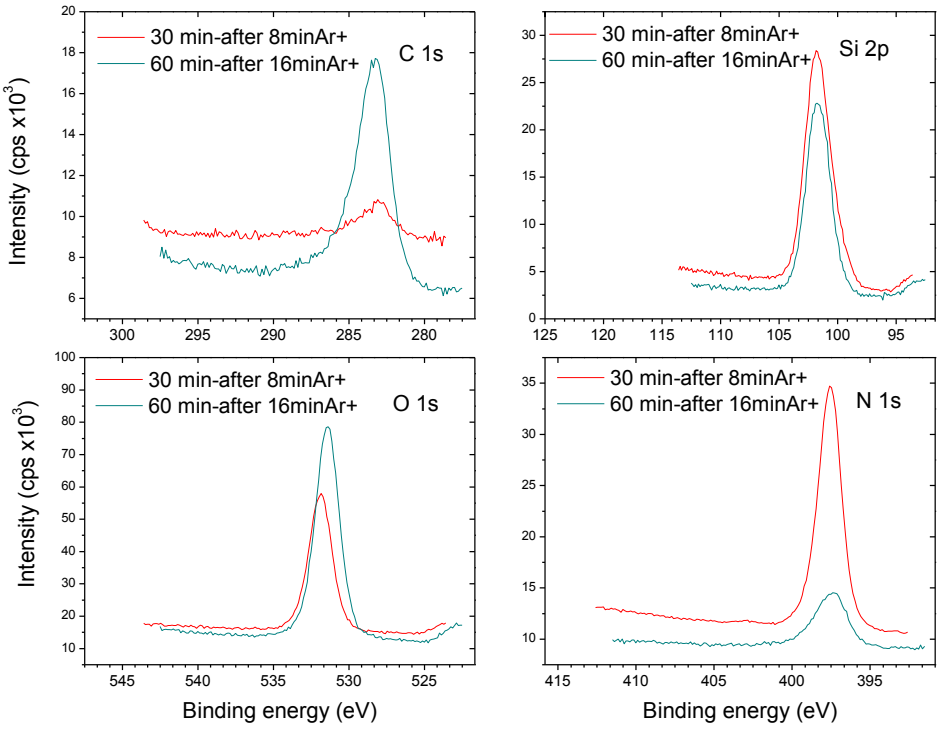

Figure 3.5. XPS spectra for sputtered SiN_x films prepared during 30 and 60 minutes.

% atomic concentration	30 min sputtering sample	60 min sputtering sample
Si 2p	51.0	33.3
O 1s	**25.4**	**36.7**
N 1s	19.0	6.1
C 1s	4.6	21.9

Table 3.2. Atomic concentration (%) of the elements deduced by XPS measurements for both samples made with SiN_x sputtering deposition.

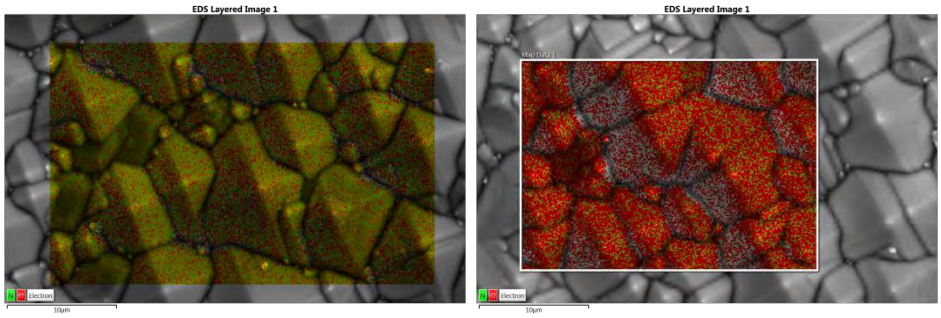

Figure 3.6. EDX mappings for films prepared during 30 minutes (left) and 60 minutes (right) of sputtering on textured silicon (O: red, N: green). The higher content of O and N on the right side of the pyramids in these pictures is caused by the position of the SEM detector (in reality all sides of pyramids were homogeneously coated).

The thickness of layers was estimated by ellipsometry measurements, obtaining a value of ca. 46 nm for samples with 30 minutes of sputtering deposition and ca. 160 nm for 60 minutes samples.

SNMS depth profiles for polished samples were carried out in order to check the thickness measured by ellipsometry. It is shown in Figure 3.7, where the signals correspond to the main elements (N, O and Si). A clear step can be appreciated looking at the line of silicon, from which the thickness could be estimated in 47 nm for samples grown during 30 minutes and 126 nm for samples grown during 60 minutes. A SEM-Fibs instrument was used to confirm also the thickness, taking similar values (55 and 122 nm, respectively).

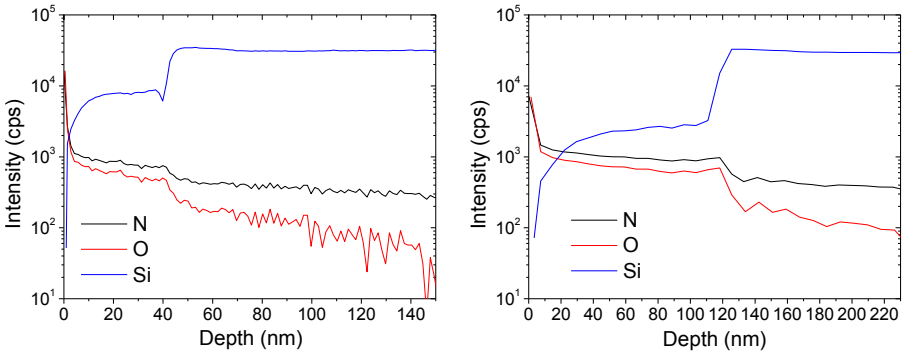

Figure 3.7. SNMS measurements confirm the thickness analyzed by ellipsometry for samples with 30 (a) and 60 minutes (b) of sputtered SiN_x layer on polished silicon.

ARCs (antireflection coatings) can effectively enhance the transmission of light. SiN_x has been used as ARC in the photovoltaic industry for many years. That is why optical properties of silicon nitride layers deposited by sputtering were analyzed in this work. The optical transmittance in the wavelength range 250-1100 nm was obtained by depositing SiN_x films on glass substrates at different times (Figure 3.8). The spectra show a good optical transparency in the Vis-NIR regions for the SiN_x films, giving a transparency in the maximum of the visual efficiency (550 nm) of 91.6% for the samples grown during 30 minutes and 87.3% for the ones deposited during 60 min.

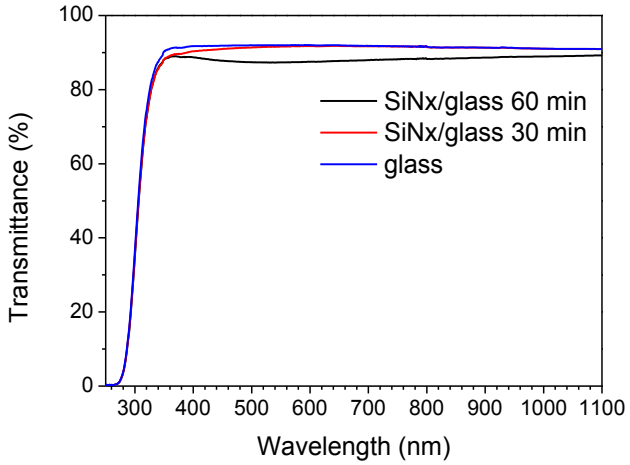

Figure 3.8. Transmittance spectra for the SiN_x layers deposited on glass.

In order to gain knowledge about the created ARCs, the refractive index, n, was estimated from the obtained values of ellipsometry. The refractive index is a function of wavelength, and the usual value referred for any material corresponds to 633 nm. In Figure 3.9 the spectral refractive index is shown in the range 250-950 nm, where

the database curve for a reference sample of SiN_x is presented together with the two curves related to the samples prepared during 30 and 60 minutes of SiN_x magnetron sputtering. For these curves there was carried out a regression supposing a first layer of SiO_2 and using the Cauchy model. For the 30 minutes sample, the thickness estimated by the fitting was 25 nm of SiN_x plus 19 nm of SiO_2, which is in accordance with the thickness calculated by ellipsometry (46 nm). In the case of the 60 minutes sample, it was of 58 nm of SiN_x plus 79 nm of SiO_2, also in accordance with the values obtained by ellipsometry (160 nm). The refractive index is better for the sample prepared during 30 minutes than for the sample prepared during 60 minutes (1.91 vs 1.82) and is close to the refractive index of Si_3N_4 reference (2.02). As it was shown with XPS and EDX measurements, the 60 minutes film has more content in oxygen and that is detrimental for the values obtained of refractive index as Figure 3.9 shows and also to the transmittance values observed previously.

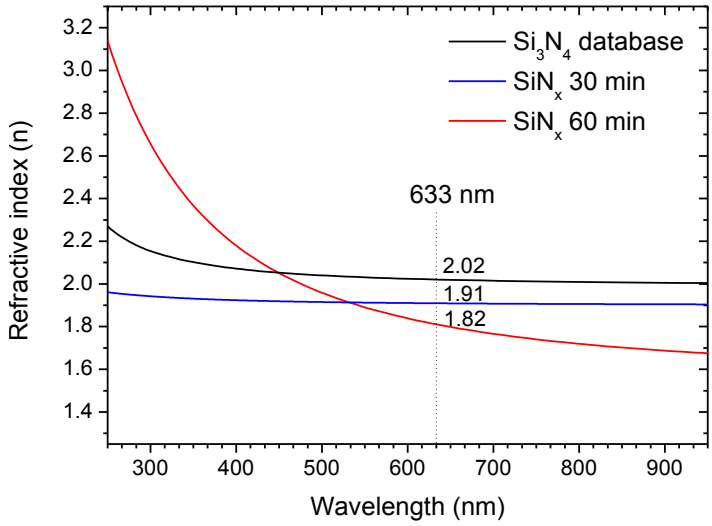

Figure 3.9. Refractive index for the SiN_x layers deposited by magnetron sputtering.

3.4.2. SiO_xN_y

3.4.2.a) Sample preparation

Samples were prepared with the same conditions as in section 3.4.1 (room temperature, 150 W of supplied power, work pressure of $1.2 \cdot 10^{-4}$ mbar and SiN_x

ceramic target) on the same type of polished silicon substrates, but adding different oxygen flows, concretely 1, 2 and 3 sccm.

After preparation of the samples, textured ones were fired in a tubular oven at 880ºC for QSSPC measurements. Structural characterization was carried out for polished samples, while morphology was analyzed for textured ones.

3.4.2.b) Results

XRD reveals the deposition of amorphous silicon nitride, showing only the peaks related to the crystalline silicon for all the samples, with no distinction on the sputtering deposition time and neither the oxygen flow rate (Figure 3.10).

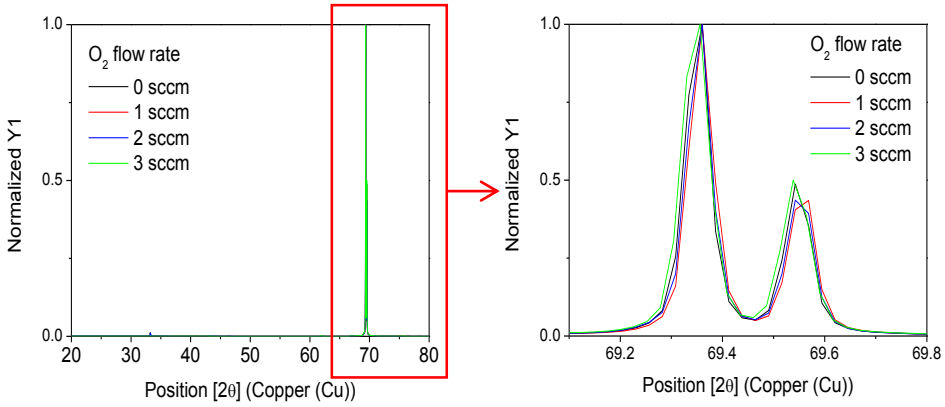

Figure 3.10. XRD spectra for 60 minutes of sputtering samples. An amorphous silicon nitride is revealed as it can be only noticed the peak of the silicon.

In the case of XPS, all the polished silicon samples with different oxygen flows and sputtering times were analyzed after 18 seconds of Ar^+ ion etching with the aim to know the stoichiometry of the coated layers. Figure 3.11 shows the O:Si and N:Si ratios for samples with oxygen flow between 0 and 3 sccm and sputtering times of 30 and 60 minutes. It is noticed that obviously samples with high O_2 flows have high O:Si ratios compared to samples made without oxygen flow. Anyway, these samples also have a high O:Si ratio. Regarding the N:Si ratio, it seems to decrease with the increasing of oxygen flow, although this variation could be considered as minimal.

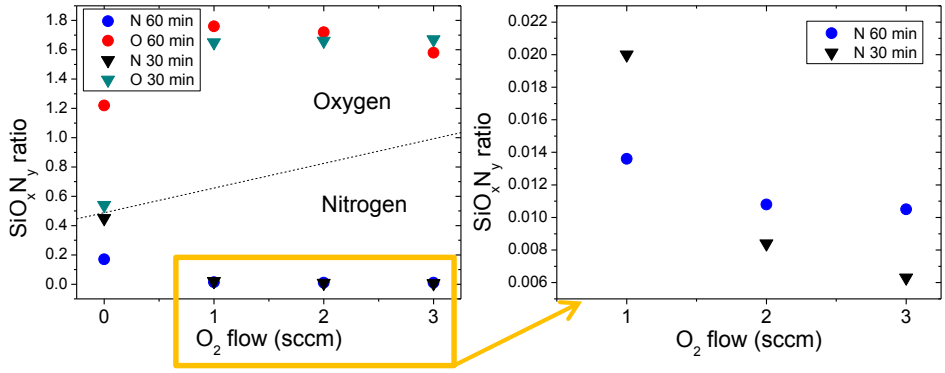

Figure 3.11. O and N ratios for SiO_xN_y samples deposited at different oxygen flows and sputtering times of 30 and 60 minutes. Results were extracted by XPS measurements after 18 seconds of Ar^+ ion etching for polished samples.

QSSPC measurements were carried out in Isofoton S. A. to the textured samples, but good results were not achieved. The reason could be that the films prepared by sputtering were not as dense as the ones prepared by PECVD (see section 3.3), as SEM images of Figure 3.12 reveal.

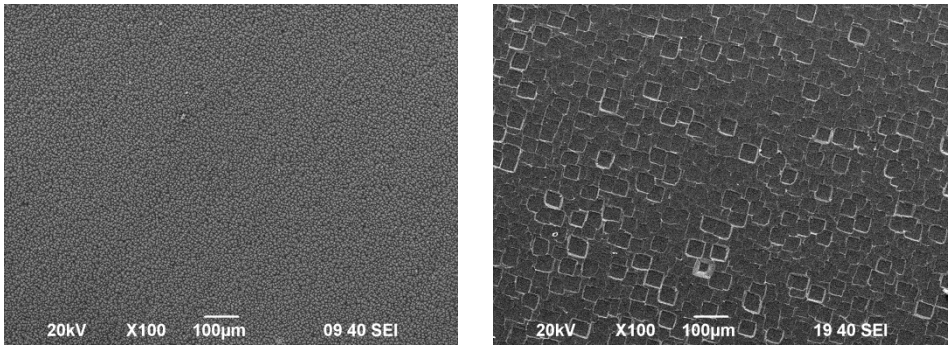

Figure 3.12. SEM pictures of the surface of SiNx sputtered sample during 60 minutes (left) and SiN_x PECVD sample (right).

3.4.3. SiO_2/SiN_x

3.4.3.a) Sample preparation

The same type of silicon wafers were used in this section. A first SiO_2 layer was obtained by thermal oxidation under air atmosphere at 950ºC in a tubular furnace, before the deposition of SiN_x by magnetron sputtering at room temperature and 150

W of supplied power. A ceramic SiN_x target from *AJA International* was used as source, and no additional N_2 or O_2 fluxes were added. The work pressure was $1.2 \cdot 10^{-4}$ mbar.

3.4.3.b) Results

SNMS spectra (Figure 3.13) show the depth profile of the thermally grown SiO_2 (left) and SiO_2/SiN_x layer (right) in the SiN_x/SiO_2/Si-substrate interfaces. A thickness of ca. 83 nm is obtained for the thermally grown SiO_2 by ellipsometry. When SiN_x layer was deposited on the SiO_2 layer, the thickness was increased reaching ca. 200 nm. It is also noticeable in this spectra the ca. 75 nm of thickness of the SiO_2 layer between the silicon substrate and the sputtered SiN_x layer.

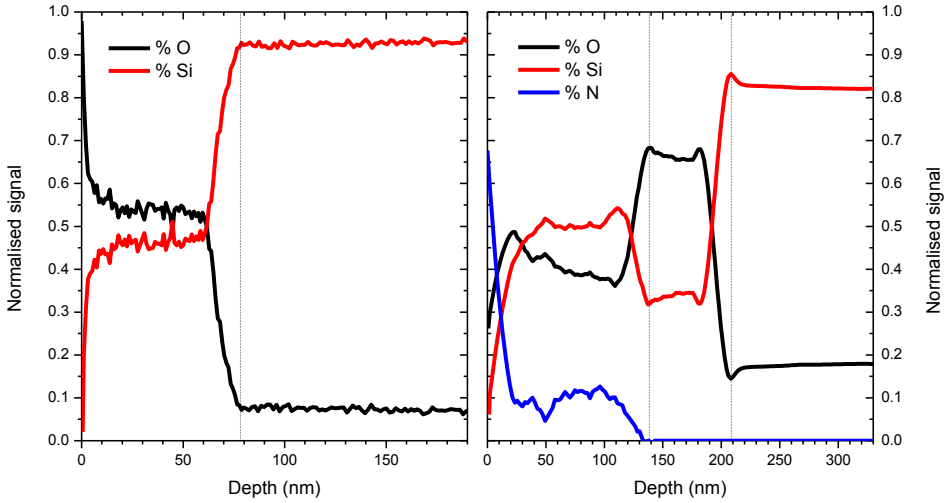

Figure 3.13. Depth profile of thermally grown SiO_2 on silicon (left) and SiN_x film prepared during 60 minutes of magnetron sputtering on thermal grown SiO_2 (right).

3.4.4. SiO_2/ZnO stacks

The ZnO is a common material used in commercial manufacture and research due to its low cost and wide availability being a direct wide bandgap semiconductor (Eg = 3.37eV) considered a promising electronic material for optoelectronic devices, solar cells and for the next generation of UV light emitting diodes because it has a large exciton binding energy (~60meV), which allows efficient excitonic emission at room temperature [65,66,81]. Zinc oxide films have been obtained onto thermal grown silicon dioxide.

3.4.4.a) Sample preparation

Now, <100>-oriented Cz as-cut silicon wafers with a resistivity of 1-3 Ωcm and a thickness of ca. 200 μm were used to grown, in a first place, the thermal silicon dioxide with a thickness of ca. 80 nm after the properly wet chemically cleaning. Then, a ceramic target of ZnO (99.9%) from *AJA International* was used as source for the deposition into the magnetron sputtering chamber under a work pressure of $1.2 \cdot 10^{-4}$ mbar. A power of 150 W was applied to the target and the deposition was carried out at room temperature, with an Ar flow of 12 sccm. Two different thicknesses for the ZnO layers were obtained.

3.4.4.b) Results

Figure 3.14 shows the depth profile of two samples of SiO_2/ZnO stacks on silicon with different thickness of the ZnO film obtained by XPS measurements taking into account that the argon ions sputter 3.5 nm of layer per minute. The thicknesses of the ZnO film would be around 150 and 200 nm observing the abrupt change in the slope of the Zn2p3 curve which adding to the 80 nm of the thermal grown silicon layer, the total thickness of the stacks would be 230 and 280 nm.

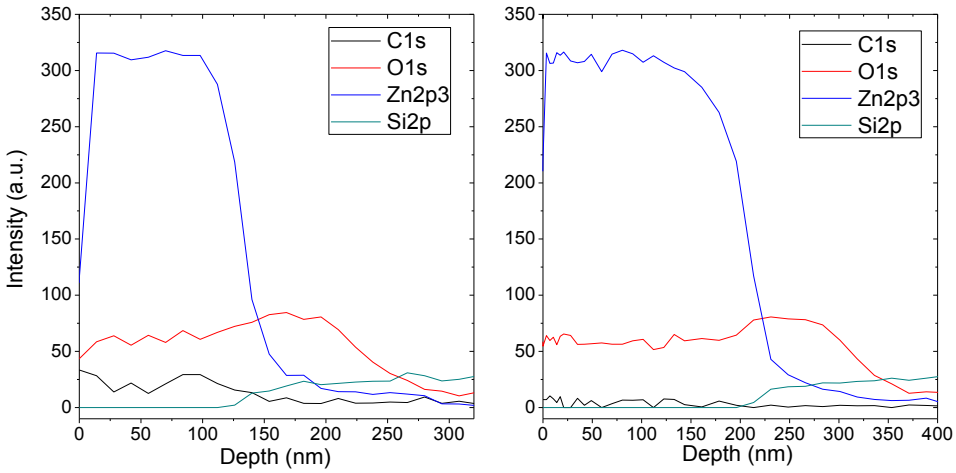

Figure 3.14. XPS depth profile for ZnO/SiO_2 stacks showing two different thicknesses of the ZnO layer.

3.4.5. Al_2O_3

Al_2O_3 layers have been deposited in bibliography using different techniques, such as ALD, PECVD and reactive sputtering, as commented in previous sections. In particular,

it was demonstrated that it is ideally suited to the rear passivation of PERC solar cells, as parasitic shunting is completely absent thanks to the fixed negative charges [82].

In this chapter, aluminum oxide layers have been grown by magnetron sputtering from a ceramic target composed by Al_2O_3, not by reactive sputtering such in bibliography. Therefore, there is not necessary an oxygen flux to carry out the process. To enable carrier lifetime testing, aluminum oxide was deposited on both sides of a wafer to create a symmetrical structure.

3.4.5.a) Sample preparation

For this section, <100>-oriented Cz textured silicon wafers with a resistivity of 1-3 Ωcm and a thickness of 180 µm were used. Additionally, <100>-oriented Cz polished p-type silicon wafers with a resistivity of 11-25 Ωcm and a thickness of 625 µm were used to carry out SNMS, XRD and ellipsometry measurements. All samples were first cleaned in a short HF dip and then sputtering process was carried out at 150W, room temperature and 12 sccm of Ar flow. The work pressure was $1.2 \cdot 10^{-4}$ mbar. An Al_2O_3 ceramic target from *AJA International* was used as source. Different sputtering times were set. Structural characterization was carried out for polished samples, while the morphology was analyzed for textured ones.

3.4.5.b) Results

Layers were composed by amorphous Al_2O_3, as XRD measurement reveals (Figure 3.15), where it is only appreciated the peaks related to the silicon.

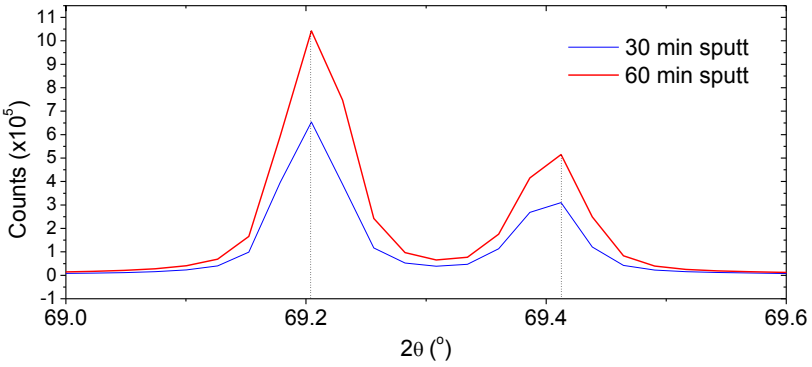

Figure 3.15. XRD measurements for samples grown during 30 and 60 minutes. An amorphous aluminum oxide is revealed as it can be only noticed the peaks related to the silicon.

For XPS measurements, a superficial acquisition was performed, followed by 18 seconds of Ar^+ etching. XPS spectra are shown in Figure 3.16, where it can be noticed

how the carbon peak, which can be a product of contamination, disappears after the Ar^+ etching. However, after this 18 seconds of etching, the rest of the elements (Si 1s, O1s and Al2p) are more appreciated, without influence of the sputtering deposition time. Peaks of O 1s at 531 eV and Al 2p at 74 eV reveal the formation of Al_2O_3. The stoichiometry of alumina was confirmed by XPS analysis, taking a value of $Al_2O_{2.9}$ after 18 seconds of Ar^+ etching.

The thickness of the Al_2O_3 layers was determined by ellipsometry and confirmed by SNMS. For 30 minutes of sputtering deposition samples, the thickness estimated by ellipsometry was 19 nm. On the other side, for samples with the double time of deposition (60 minutes), the thickness was also around the double, taking a value of 38 nm. SNMS depth profiles for these samples (Figure 3.17) support the thickness analyzed by ellipsometry.

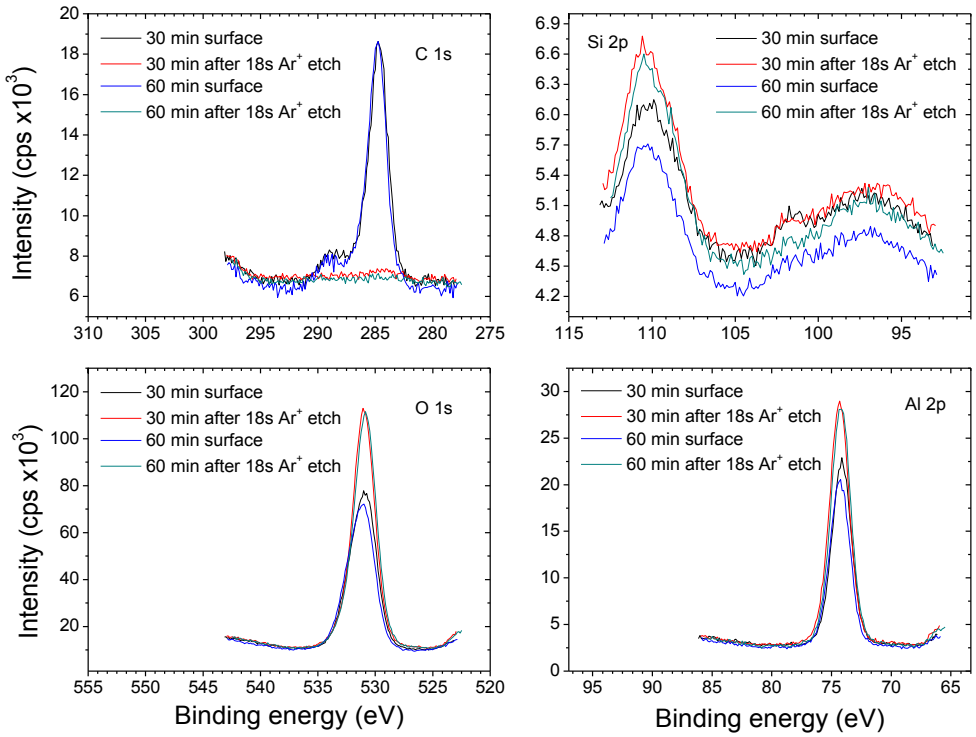

Figure 3.16. XPS spectra of aluminum oxide coated polished silicon samples during 30 and 60 minutes of sputtering. Superficial and after 18 seconds of Ar^+ ion etching acquisitions were performed.

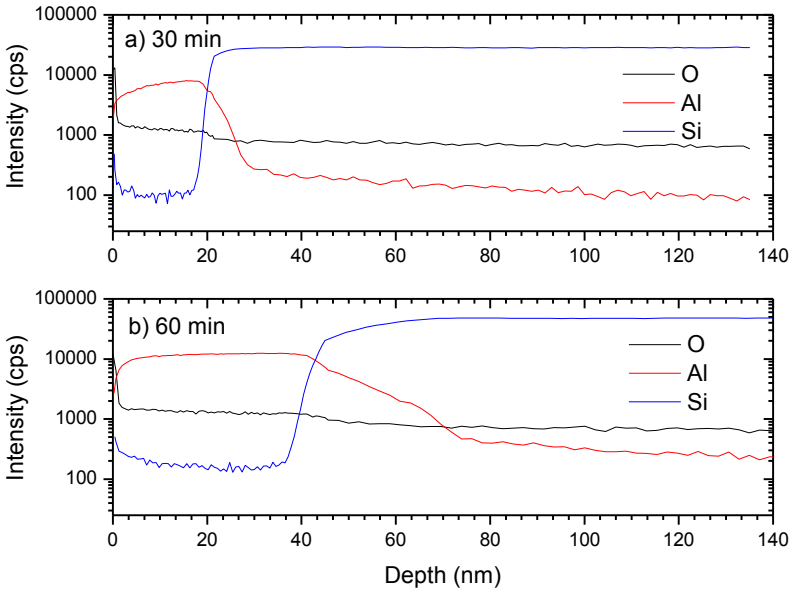

Figure 3.17. SNMS depth profiles registered for samples with sputtering times of Al_2O_3 of 30 (a) and 60 minutes (b).

To study the quality of the passivation, QSSPC measurements were carried out and lifetimes were extracted. Neither Al_2O_3 sample (30 and 60 minutes of sputtering) offered result for the lifetime. Then, after the firing the surface of the samples were enhanced with an annealing at 400ºC under nitrogen atmosphere during 30 minutes in a tubular furnace. The lifetime value for the best wafer prepared during 30 minutes of magnetron sputtering was 18 µs, while for the 60 minutes wafer decreased to 9.16 µs.

3.4.6. Al_2O_3/SiN_x stacks

A SiN_x capping layer on top not only protects the Al_2O_3 layer from the aluminum metallization but also improves the thermal stability of the surface passivation. By optimization of the SiN_x deposition, an enhanced thermal stability of these films is achieved [83].

Al_2O_3/SiN_x stacks were prepared with the magnetron sputtering striking a power of 150 W for the ceramic targets of SiN_x and Al_2O_3 during 60 minutes in the case of Al_2O_3 and 30 and 60 minutes for the SiN_x at room temperature under Ar flow of 12 sccm and working pressure of $1.2 \cdot 10^{-4}$ mbar. SNMS profiles were carried out with the aim to

analyze the created interfaces (Figure 3.18). The thickness reached for the Al_2O_3 layer was around 40 nm (see blue color in (b) and (d), agreed also with Figure 3.17b.

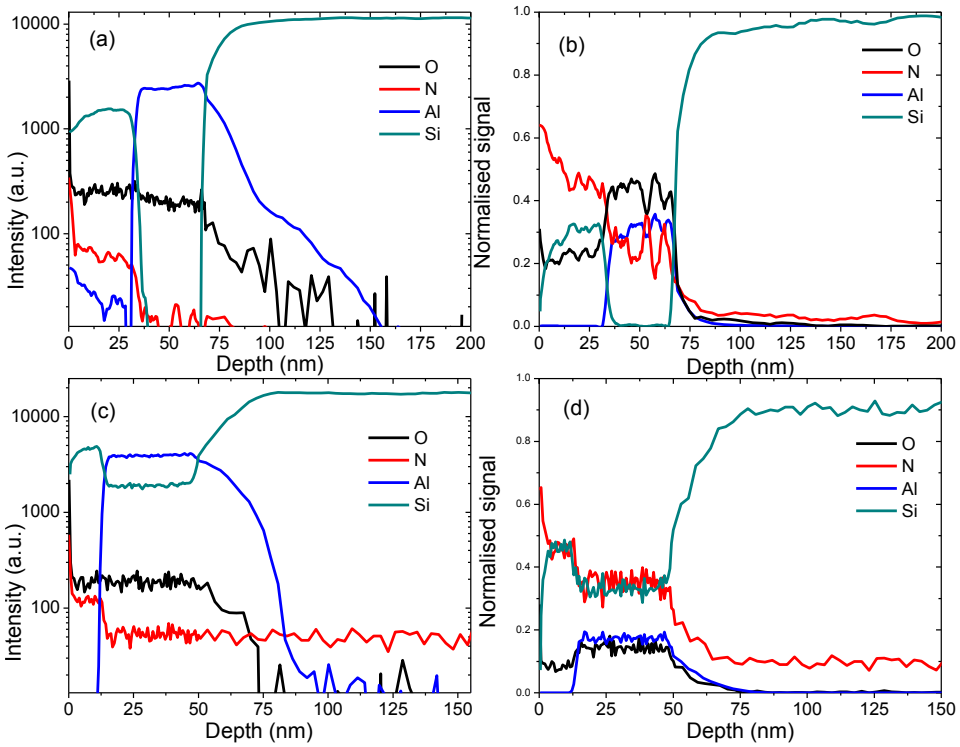

Figure 3.18. Depth profiles, obtained by SNMS, of Al_2O_3/SiN_x stacks prepared during 60 min Al_2O_3 + 60 min SiN_x of magnetron sputtering (a and b) and 60 min Al_2O_3 + 30 min SiN_x of magnetron sputtering (c and d).

However, the thickness of SiN_x layer deposited on Al_2O_3 was not the same when deposited on silicon. In the case of the stack, the thickness for the SiN_x layer was thinner than in the single layer. As it was remarked before, for 30 and 60 minutes of sputtering deposition on silicon, the SiN_x layer got a thickness of 55 and 122 nm respectively. Deposited on the alumina, the thickness of SiN_x layer was estimated by ellipsometry in 17 and 30 nm for 30 and 60 minutes of sputtering deposition respectively. It is explained with the roughness of the deposition surface. Figure 3.19 shows the AFM images of polished silicon (left) and alumina on polished silicon (right) and reveals the surface roughness. The recorded AFM data indicated that the average of maximum height was 0.12 nm for the silicon and 0.44 nm for the alumina. Consequently the medium roughness for the alumina was higher, taking a value of 0.448 nm versus 0.190 nm for the silicon. Therefore, when SiN_x layers were deposited on alumina, the growing rate by sputtering was lower because the roughness of the

deposition surface (alumina) makes the SiN_x particles spread on a bigger surface, in contrast with layers deposited on silicon.

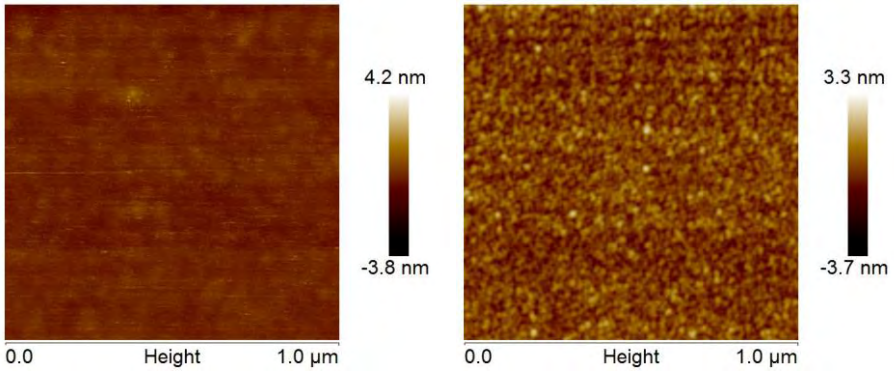

Figure 3.19. AFM image of polished silicon (left) and a thin layer of Al_2O_3 (60 min) on polished silicon (right).

Comparing the growth rate of 30 and 60 minutes for SiN_x sputtering on the Al_2O_3 layer, after 60 minutes of SiN_x sputtering (Figure 3.18 a-b), the sample shows higher concentration of oxygen, approximately the double than the one after 30 minutes. In the first case, the Al/O ratio is 0.7, close to the stoichiometry of Al_2O_3 (2/3=0.67). For the 30 minutes SiN_x sample, the Al/O ratio increases to 0.8. Then, to ensure a more exact stoichiometry of the Al_2O_3, it is needed 60 minutes of SiN_x sputtering in these conditions so that the oxygen content increases and the aluminum does not. While SiN_x target is striking, the oxygen attached to the wall of the chamber goes also to the plasma and this way contributes to the coated layer too. The profiles show also a sharper Si/stack interface for the samples prepared during 60 minutes of SiN_x magnetron sputtering.

3.4.7. Al-doped ZnO thin films (AZO)

In this section, undoped ZnO and Al:ZnO films are deposited onto silicon wafers and glass by magnetron sputtering, with the aim to analyze the layers abilities as TCOs for heterojunction silicon solar cells.

3.4.7.a) Sample preparation

Undoped and Al-doped ZnO thin films have been deposited by RF magnetron sputtering on p-type polished Si wafers after the proper wet-chemically cleaning (see Appendix A). Quartz substrates were also coated for the transmittance, Raman and resistivity measurements. Two types of ceramic targets from *AJA International, Inc* were employed: undoped ZnO (99.99%) and Al_2O_3 (99.9%). The doping percentage was regulated by the power supplied to the Al_2O_3 target (20, 30, 40, 50 and 55 W),

while the power for the ZnO target was set at 150 W. Table 3.3 shows the nomenclature of the samples. The working pressure into the vacuum chamber was maintained at 1.4 x 10^{-2} mbar with a high purity (5.0) Ar gas, regulated by a mass flow controller at 12 sccm. The substrate temperature was maintained constant at 300ºC, and all the samples were deposited during 20 minutes, except for the samples prepared for the RAMAN analysis, which were synthetized during 3 hours for the least and the most doped sample (Z-A20 and Z-A55 respectively).

X-Ray Diffraction (XRD), Secondary Neutrons Mass Spectroscopy (SNMS), SEM-FIB images, transmittance and conductivity measurements were carried out to the 20 minutes samples.

Name	Composition	Al_2O_3 supplied power
Z	ZnO	0 W
Z-A20	Al:ZnO	20 W
Z-A30	Al:ZnO	30 W
Z-A40	Al:ZnO	40 W
Z-A50	Al:ZnO	50 W
Z-A55	Al:ZnO	55 W

Table 3.3. Nomenclature of the samples prepared by RF magnetron sputtering.

3.4.7.b) Results

XRD was carried out to analyze the crystallinity of the samples. First of all, the peaks 004 related to the silicon were aligned to study the rest of the peaks. Undoped and doped films prepared on silicon crystallize in the hexagonal zincite structure, and are highly oriented perpendicular to the substrate surface (Figure 3.20).

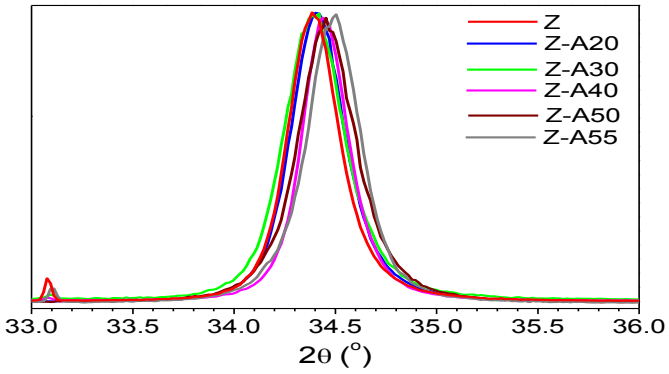

Figure 3.20. Zincite peak obtained by XRD measurements for undoped and doped samples, prepared during 20 min of RF magnetron sputtering.

The three most doped samples (Z-A40, Z-A50 and Z-A55) show zincite peak, the only peak that appears, shifts to the right of the undoped sample. The width of those peaks at medium high (FWHM) is shown in Figure 3.21. They do not follow any tendency but for the three first samples (Z, Z-A20 and Z-A30), whose peaks are wider when increasing the doping.

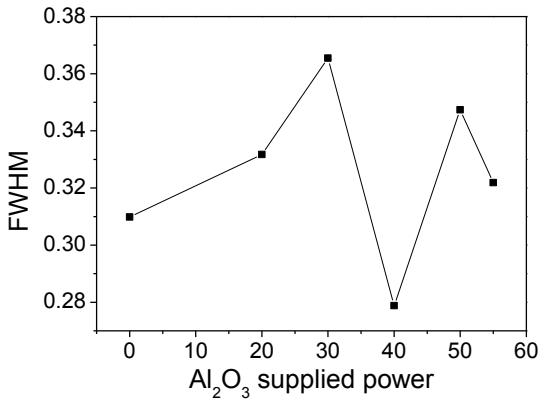

Figure 3.21. Variation of FWHM with the doping for the samples prepared during 20 minutes of RF magnetron sputtering.

SNMS depth profiles for the less and most doped samples (Z-A20 and Z-A55) are shown in Figure 3.22. The aluminum amount remains constant along the thickness of the film for the less doped sample. Regarding the most doped sample, there is a tendency for the aluminum amount to increase near the interface. This aluminum amount seems to be ca. 10 times higher for the most doped sample, being the ratio Al/Zn 0.002 for the less doped sample and 0.02 for the more doped sample. The thickness of the interfaces is very similar for both samples. It can be easily appreciated the abrupt change of slope of the silicon curve, which increases the concentration in detriment of the concentration of Zn and O.

SEM-FIB equipment was used to carry out cross-sections of all the samples to measure their thickness, which did not follow any tendency with doping (Table 3.4).

The resistivity was measured with the four probe method and the obtained values are presented in Figure 3.23. The conductivity of the samples increases with the doping, showing a mayor variation for the less doped samples. The lowest resistivity was reached for the most doped sample (Z-A55), achieving a value of 4.15 mΩ x cm, while the undoped sample achieved the highest resistivity with a value of 46.9 Ω x cm.

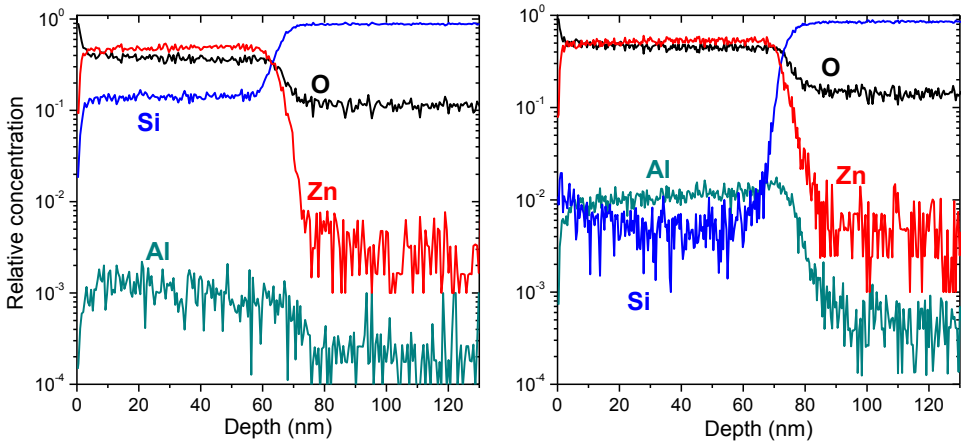

Figure 3.22. Depth profile of samples Z-A20 (left side) and Z-A55 (right side).

Sample	Average thickness (nm)
Z	63.82
Z-A20	69.67
Z-A30	58.42
Z-A40	66.46
Z-A50	80.85
Z-A55	73.34

Table 3.4. Average thickness of the films created.

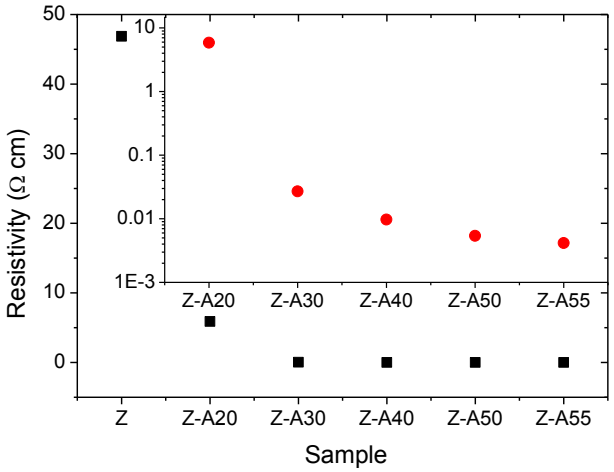

Figure 3.23. Variation of the resistivity with the doping plus zoom for the doped samples.

The optical properties of the films prepared onto quartz substrates have been studied by optical transmittance experiments, which were carried out within the wavelength range 200-2500 nm, thus covering the full visible spectrum (Figure 3.24). The spectra exhibit a sharp ultraviolet absorption edge, independently of doping, and a transmittance of about 77% for the ZnO and ca. 80% for the most doped samples at the maximum of visual efficiency (550 nm). Hence, doping supports the transparency of the films, an important result considering their potential applications as TCOs.

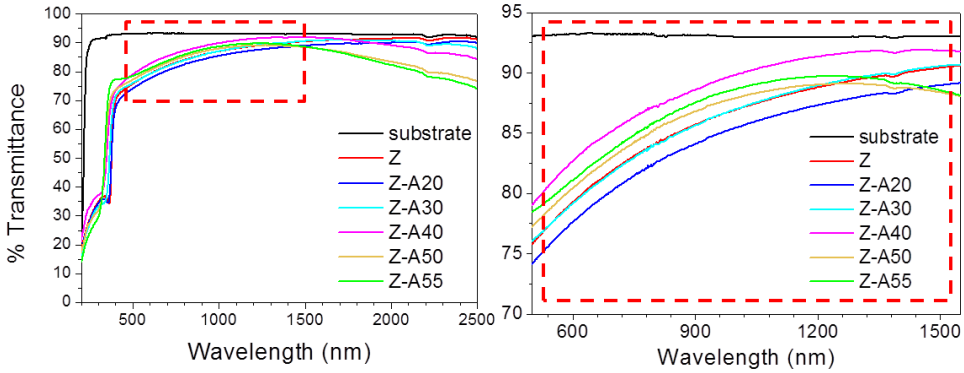

Figure 3.24. Transmittance spectra for samples prepared during 20 minutes onto quartz substrates.

The band-gap values can be directly estimated from these optical measurements. The optical band-gap energy, E_g, was determined using the equation

$$(\alpha h\nu)^2 = C(h\nu - E_g), \tag{3.1}$$

where C is a constant that depends on the electron-hole mobility, and $h\nu$ is the photon energy. The band-gap (E_g) was calculated by extrapolating the linear portion to the energy axis in the $(\alpha h\nu)^2$ vs. $h\nu$ graph. This graph is shown in Figure 3.25, together with the obtained results for the undoped and doped samples. The band-gap values increase with doping reaching a maximum value of 3.57 eV for the most doped sample (Z-A55), while the obtained result for the undoped film was 3.23 eV, which is in accordance with previous research [84]. The shift in the band gap of the doped ZnO films has been widely observed and ascribed to the Burstein-Moss shift due to the increase in carrier concentration [85], although some researchers mention the presence of enhanced stress in Al-doped films as a possible origin of this shift [86]. The most pronounced shift is observed for the two most doped films (Z-A50 and Z-A55).

That increasing of the band-gap for the two most doped samples matches with a change in the film morphology, which is shown in Figure 3.26 and Figure 3.27 with more detail.

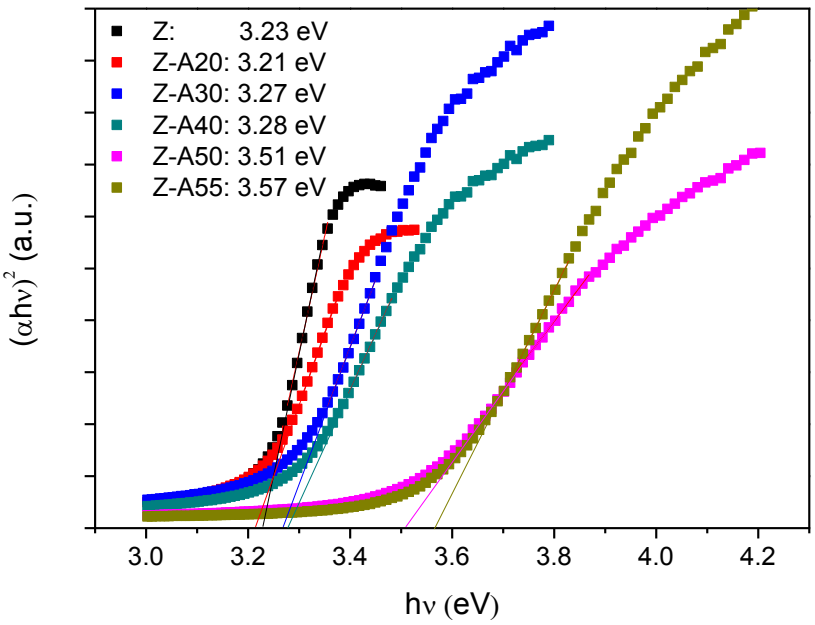

Figure 3.25. Estimation of band-gaps for the undoped film (black) and doped films (rest of colors)

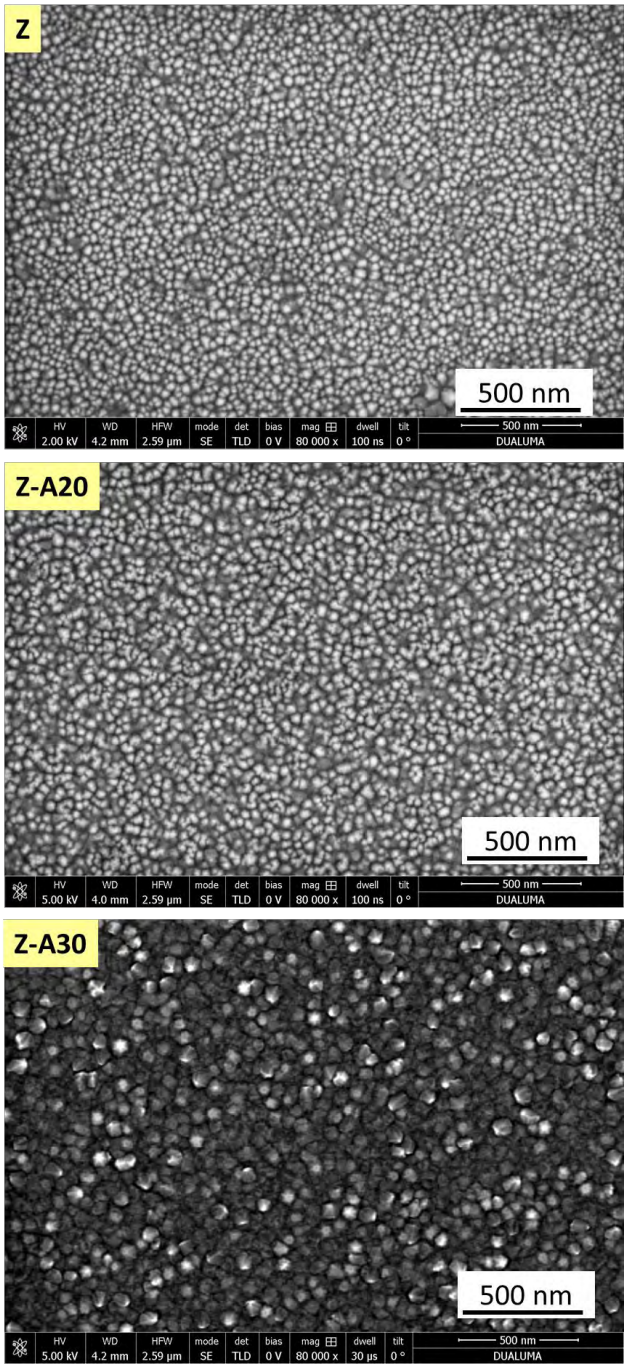

Figure 3.26. FESEM surface images at the same magnification of films prepared on silicon substrates during 20 minutes.

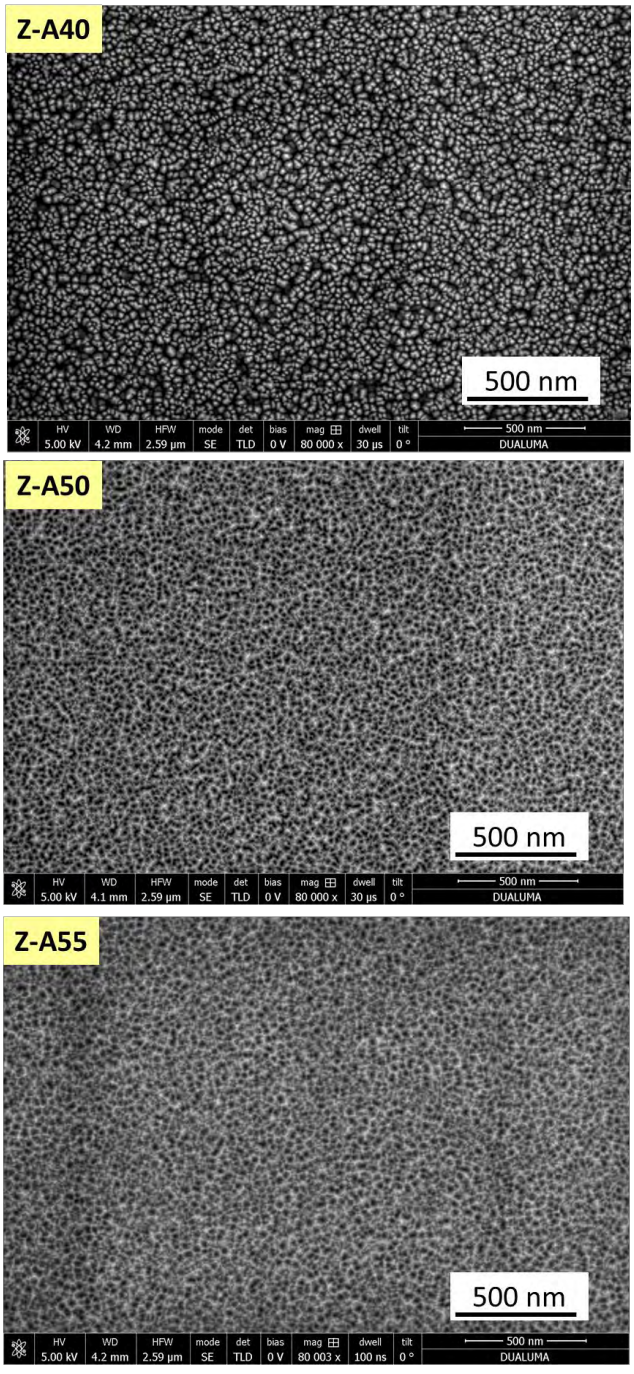

Figure 3.27. FESEM surface images at the same magnification of films prepared on silicon substrates during 20 minutes.

AFM images of ZnO and AZO thin films (Figure 3.28) exhibits granular films with good homogeneity and no cracks were observed. The root mean square (RMS) roughness of the ZnO and AZO films is represented in Figure 3.29, which reveals that RMS roughness of the AZO films is smaller than that of ZnO. The general decrease in surface roughness with Al doping may be caused by Al segregation at the non-crystalline region in the boundary [87] and the non-linearity of the decreasing of the RMS roughness is in agreement with other results [88].

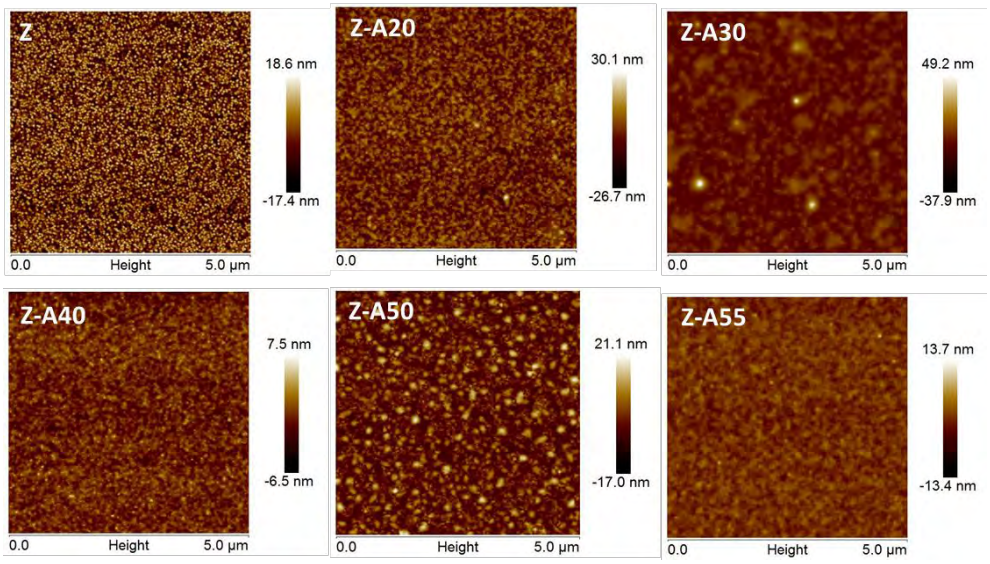

Figure 3.28. AFM images of 5 x 5 µm sections of ZnO and AZO thin films.

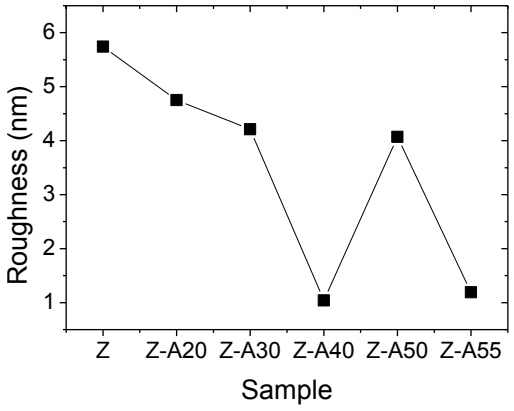

Figure 3.29. RMS roughness for ZnO and AZO films.

HRTEM images (Figure 3.30) were obtained from cross-sections of the non-doped sample (Z), the least and the most doped samples (Z-A20 and Z-A55 respectively). Towards the Z plane, pointed ended prismatic columns are shown with 60-70 nm of length for the three studied samples. For the non-doped sample (Z), these columns are sharper, which is in accordance with the roughness measured by AFM measurements. Figure 3.31 shows some particles for the least and the most doped samples. It can be noticed more crystallinity of the particles for the most doped samples, which could be attributed to the doping.

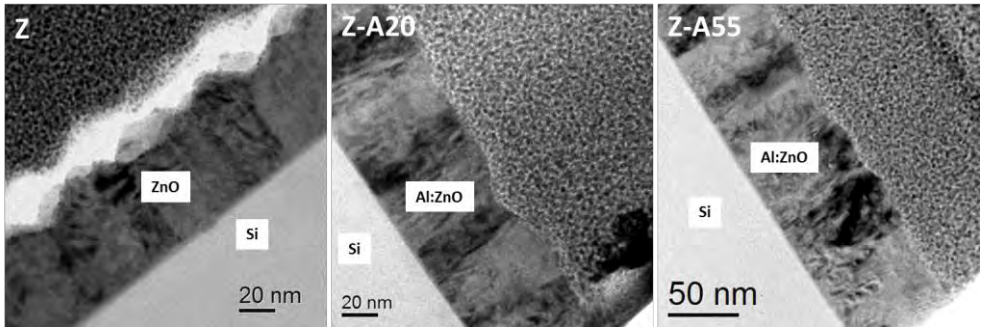

Figure 3.30. HRTEM images of cross-sections of samples Z, A-A20 and Z-A55.

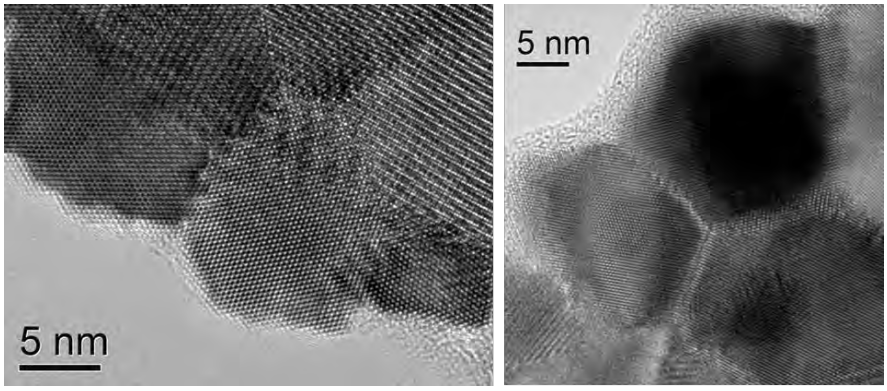

Figure 3.31. Plan-view HRTEM images of samples Z-A20 (left) and Z-A55 (right).

Thicker films of Z-A20 and Z-A55 were specially grown during 3 hours onto glass substrates for the Raman measurements because silicon substrates mask the spectrum of the films. Raman spectra for these samples are shown in Figure 3.32. In both cases, substrate signal has been deducted, but in spite of that, for the most doped sample there is a significant background contribution. This may be due to phonon scattering induced by defects in crystalline lattice, mostly the dopant Al ions.

In backscattering Raman spectra the presence of E_2(low) and E_2(high) modes and the absence of TO modes are a fingerprint of ZnO films oriented along the (0 0 0 1) direction, as reported previously [84,89,90]. For the most doped sample, Z-A55, E_2(high) mode is shifted, 441.5 cm^{-1} vs. 437.6 cm^{-1}, compared to that of the least doped sample.

A_1(TO) mode, which is forbidden for ZnO oriented films, appears due to the translational symmetry breaking induced by doping. The appearance of forbidden B_1 modes is also induced by doping and is commonly observed for III group dopants. E_1(LO), A_1(LO) and B_1(high) modes seem to appear in different proportion for these doped samples. There are some additional peaks in the spectra which deserve attention. Small peak at 58.36 cm^{-1} is an experimental artefact. There are two peaks centred at 329.9 and 303.8 cm^{-1}, for the less and more doped samples respectively, which have not been seen before, but it could be related to the aluminum impurities.

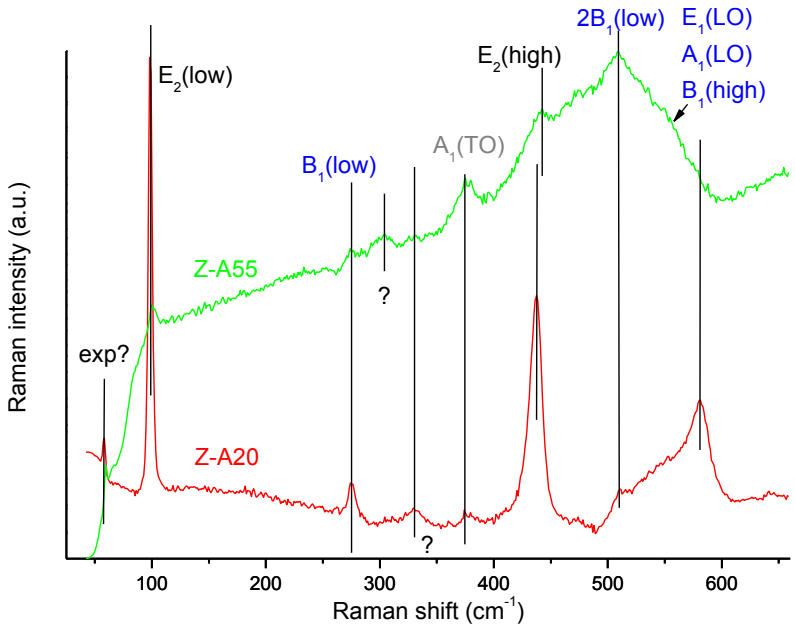

Figure 3.32. RAMAN spectra for the least and the most doped samples (Z-A20 and Z-A55 respectively) prepared during 3 hours of RF magnetron sputtering.

4

Screen-printed local Al-alloyed structures

In this chapter, screen-printed local Al-alloyed structures are analyzed on Cz and FZ silicon wafers with the aim to create a LBSF. The electrical properties of the local contacts were studied. An analysis of the microstructure was also carried out. Firstly, results by automatic screen printing at Fraunhofer ISE are presented using the FTC method with different passivating layers. Afterwards, a manual screen printer was used with the same purpose.

4.1. Introduction

Passivating the rear surface is beneficial for the efficiency of silicon solar cells, but it requires local contact openings to form the electrical contact. The opening for local contacts usually requires a laser or other technological processes, which raise the price of the process [91-93]. In this chapter, the aim is to obtain a LBSF without the necessity of doing any etching and neither using any expensive laser. For that reason, LBSF has been obtained by screen-printing technique using aluminum pastes with frites to allow the penetration of the dielectric passivation layer during firing. This technology is called fire-through contact (FTC), and is quite new comparing with the other techniques. With the FTC approach, only screen-printing is needed, apart from the PECVD used for the passivation layer [94,95]. This is advantageous for industrial production, due to the smaller number of technologies on which the FTC method depends, as well as the fact that screen-printing is already widely used for solar cell manufacturing. With the strongly growing interest in solar cells featuring local contacts at the rear side, FTC technology gains importance.

In this chapter, we evaluate the FTC technology with different aluminum pastes for local contact formation in silicon solar cells. Compared to previously results [95,96], a significant increase of the actually contacted area is achieved.

Summing up, the FTC mechanism presented employs a local penetration of the aluminum paste through the dielectric passivation layer during contact firing, requiring only printing technology.

4.2. Local contact formation on Cz silicon wafers

4.2.1. Experimental

Quasi-squared Cz silicon p-type wafers of base resistivity 1-3 Ωcm, 200 μm diameter and 175 μm thickness were first wet chemically cleaned and then symmetrically passivated with silicon rich oxy-nitride (SiriON) stacks [74] of ca. 80 nm. Then, screen-printing of different structures (Figure 4.1) was carried out with an Al paste named B, to print two layers on the wafers; after that, the paste was dried in a belt furnace at 220ºC. After firing process in an industrial belt furnace (890ºC at 5200 mm min^{-1}), the BSF is obtained due to the fire through contact process. The lifetime samples were treated with HCl/H_2O_2 and forming gas annealing in order to fully remove the rear Al structure and then enable a QSSPC measurement. TLM measurements were carried out to the resistance samples to study the influence of the difference structures on the

effective specific contact resistance. Optical and scanning electron microscopies were used to study the morphology of the rear contacts.

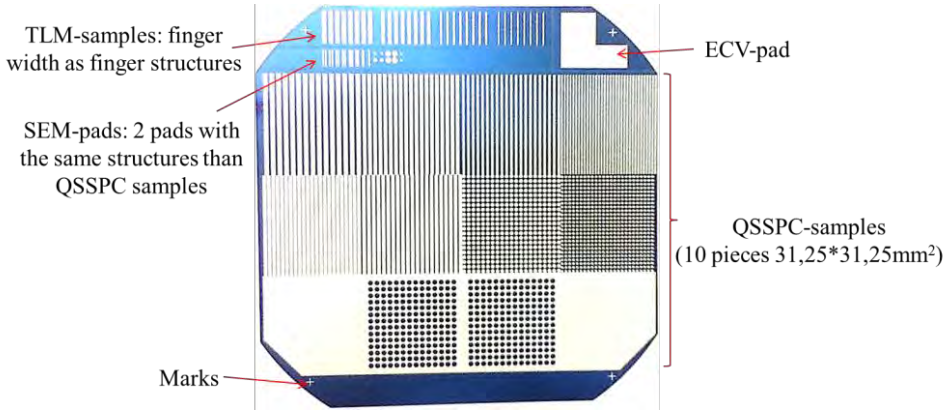

Figure 4.1. Aluminum printed wafer with the different structures.

4.2.2. Electrical properties

Low recombination is an important property for local rear contacts, but low contact resistance is also essential. To allow for a comparison of different structures (Table 4.1), the emitter saturation current density J_{0e} and the effective specific contact resistance ρ_{eff} were measured. As the lifetime samples are symmetrical (see Figure 4.2), the emitter saturation current density J_{0e}

$$J_{0e} = S_{eff} \frac{q\, n_i^2}{\Delta n + N_A} \tag{4.1}$$

S_{eff}: effective surface recombination velocity, n_i: intrinsic carrier concentration, Δn: excess carrier of electrons, N_A: concentration of aceptor atoms is calculated using the effective lifetime τ_{eff}, measured after samples were treated with HCl/H_2O_2 in an ultrasonic bath in order to remove the Al residuals, followed by a forming gas annealing step to recover the surface passivation quality and thus enable the QSSPC measurement. Figure 4.3 shows the correlation between J_{0e} and ρ_{eff} for the different investigated contact structures. Strong deviations are shown due to inhomogeneity in surface passivation quality. The effective specific contact resistance was measured for the resistance samples (structures 1-4 in Table 4.1) to allow the comparison of the results with the emitter saturation current density. The specific contact resistance decreases with the rise of area covering.

Structure	Pitch (µm)	% Al coverage
1	2000.0	70
2	1600.0	70
3	1500.0	50
4	900.0	50
5	1300.0	80
6	1500.0	70
7	1500.0	50
8	1200.0	30
9	(full area)	100
10	2000	50
11	2000	50
12	(full area)	100

Table 4.1. Contact geometries for the different aluminum structures. (SiriON + Al paste)

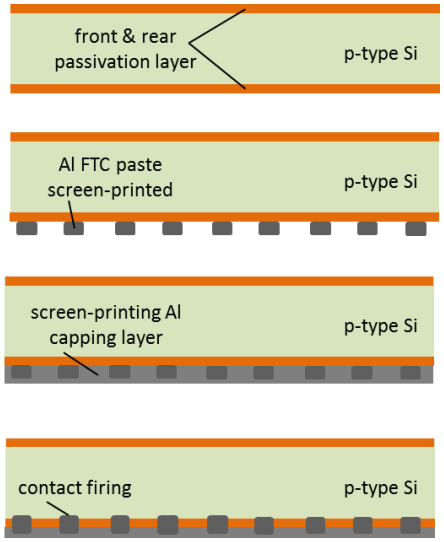

Figure 4.2. Schematic process flow for the fire-through contact (FTC) approach of this work.

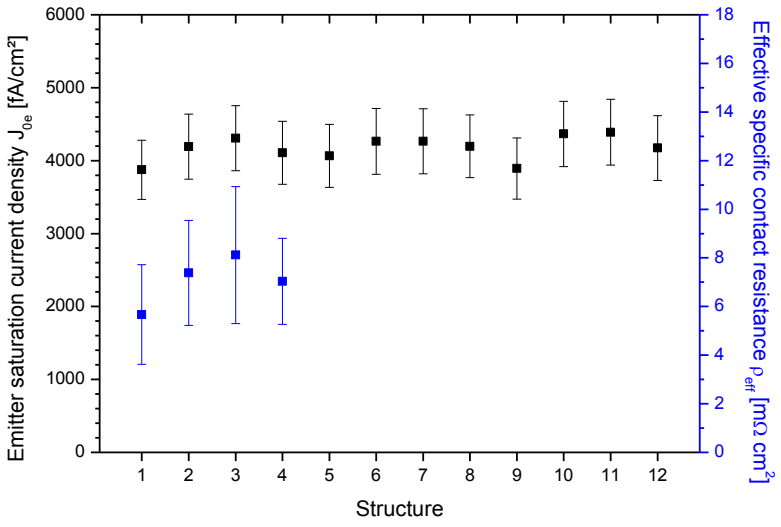

Figure 4.3. Dependency of the emitter saturation current density J_{0e} and the effective specific contact resistance ρ_{eff} on the printed structure on SiriON.

4.2.3. Microstructure analysis of the local contacts

With the aim to test the aluminum paste as fire-through paste, a thin SiriON layer of ca. 80 nm was carried out by PECVD method on textured p-type silicon wafers to act as passivation layer. Then, two layers of aluminum paste B were screen printed followed by a fast firing. A microstructure analysis was carried out to gain knowledge about the contact formation, and also the Al-Si alloying formed after firing for SiriON passivated silicon wafers. The cross-section of the wafer (Figure 4.4-a) confirms the successful penetration of the passivation layer by the aluminum paste, and the resulting local alloying of Al into Si. The inverted pyramid shape is caused by the texturing of the wafers with the orientation (111).

Optical micrograph of an aluminum printed line of 632 µm width (Figure 4.4-b), carried out after Al paste removal shows a contact density that differs on the area covered by the Al paste. However, this study demonstrates a clear progress compared to former results [95]. Specific contact resistance of different line widths depicted in Figure 4.3 confirms the high contact density shown in Figure 4.4-b, showing a decreasing of that resistance with the rise of the area coverage (lines width) for lines with a pitch of 2 mm, reaching a minimum value of 5 mΩcm² for lines width of ca. 1200 µm.

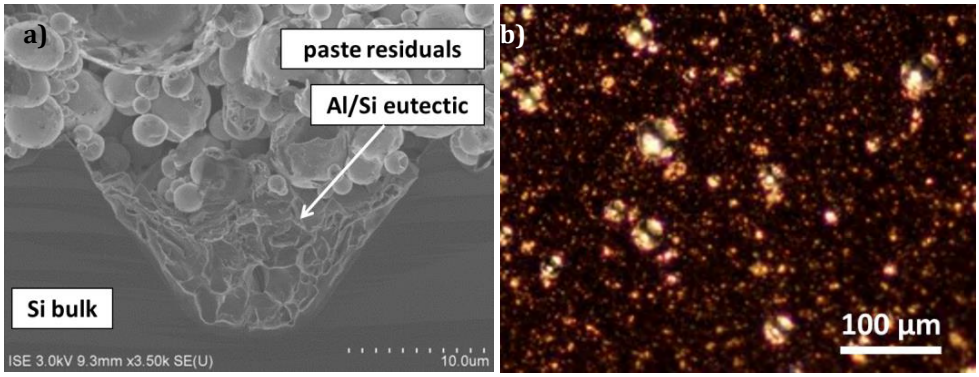

Figure 4.4. (a) FESEM micrograph of a FTC cross-section. The Al-Si eutectic penetrates the p-type silicon in a pyramidal shape. (b) Optical micrograph of FTC area after Al removal of a 632 µm width line.

4.3. Local contact formation on FZ silicon wafers

The screen-printing of different structures was carried out to the samples with two different fire-through aluminum pastes (paste A, from *Toyo Aluminum K.K,* and paste B, from *Ferro*) before contact firing in an industrial belt furnace under different firing conditions. Different areas with test structures on symmetrical passivated samples were screen-printed designed for the following measurements (QSSPC or Transmission Line Method (TLM)). The results were published as a conference proceeding in the 28th EUPVSEC [97].

4.3.1. Experimental

Monocrystalline FZ silicon wafers of 200 µm thickness and 125 mm edge length, boron-doped with a specific resistivity of 0.8 Ωcm were used. The studied passivation layers were SiN_x and silicon rich oxy-nitride (SiriON) stacks [98] of about 80 nm, both formed by plasma-enhanced chemical vapor deposition (PECVD) after the wet-chemically cleaning of the wafers. The paste was locally applied onto the passivated rear followed by full area printing of the Al capping layer. After metallization with two different pastes (A and B), the wafers were exposed to a typical contact-firing step in a fast firing oven. The process-scheme was shown in Figure 4.2. Afterwards, the characterization of the contact conductivity and recombination velocity was carried out by TLM and QSSPC measurements, respectively. For QSSPC, the samples were etched with an ultrasonic-assisted HCl etching in order to remove the aluminum residuals and annealed in forming gas atmosphere afterwards to re-activate the passivation after the ultrasonic treatment. A morphological study was also carried out by optical microscopy and SEM for studying the contact area and the penetration of the aluminum pastes through the passivation layers, respectively.

4.3.2. Electrical properties

The results achieved so far demonstrate the potential of the FTC approach. A novel FTC paste (paste A) shows clear advantages compared to formerly used paste systems. Additionally, this paste shows high process stability with low dependency on the passivation layer and the firing conditions in comparison to the reference paste B (Figure 4.5). The contact density observed after Al paste removal was higher for paste A (Figure 4.6-a) than for B (Figure 4.6-c). This is confirmed by the measured contact resistance (Figure 4.5).

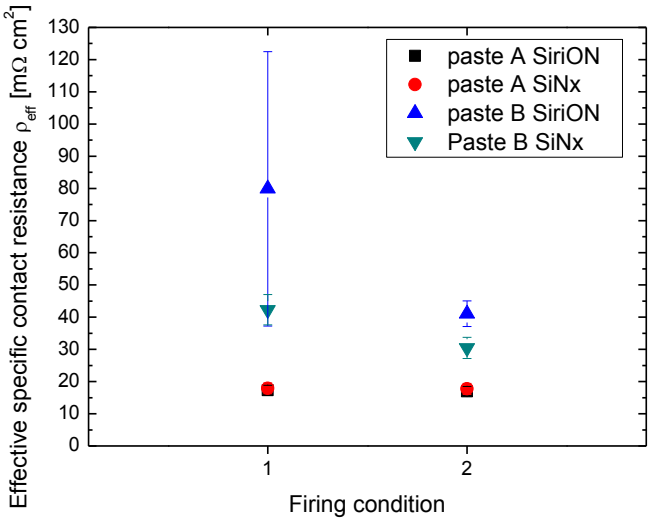

Figure 4.5. Effective specific contact resistance and its standard deviation for the two different firing conditions: 1) 890°C - 5200 mm/min and 2) 890°C - 4500 mm/min. Each point represents the mean of two samples with different line widths and a pitch of 2 mm.

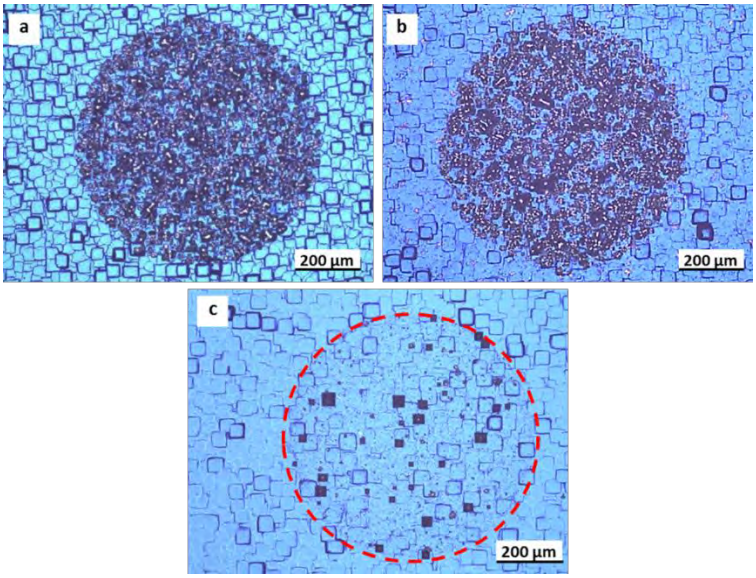

Figure 4.6. FTC area after Al removal of SiN_x passivated wafers for a) paste A without Al capping layer, b) paste A with Al capping layer, c) paste B without Al capping layer. For paste B, smaller contact density is observe; this explains the increased contact resistance of paste B depicted in Figure 4.5 and also $S_{met,eff}$ of Figure 4.7.

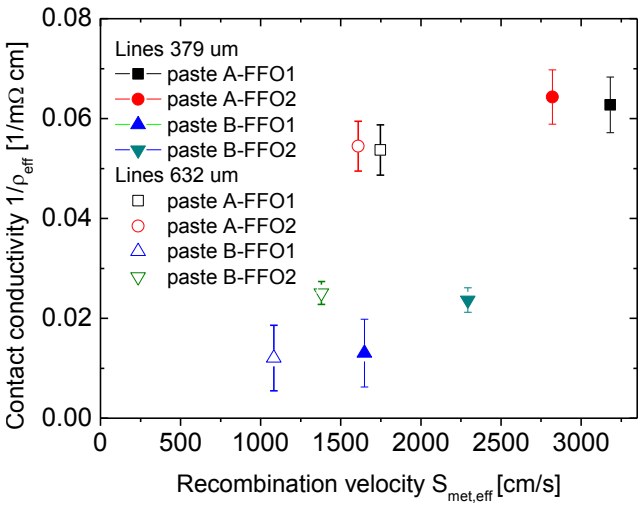

Figure 4.7. Contact conductivity $1/\rho_{eff}$ and recombination velocity $S_{met,eff}$ referred to the contact area for SiriON passivated samples. Results for paste A and B are shown, as well as firing conditions 1 and 2 (FFO1 and FFO2 respectively). Paste A delivers better contact conductivity than paste B for the same recombination velocity and firing condition.

In contrast to previously published results [95,96], no influence of the capping Al layer was observed, as optical microscopy reveals (Figure 4.6-a-b). The contact density in the FTC area for paste A demonstrates a clear progress compared to former results [96].

The highest recombination velocities were found for samples with lines width of 379 µm (Figure 4.7) on SiriON passivated samples. Comparing the same recombination velocity and firing condition for pastes A and B, the first one delivered better contact conductivity.

4.3.3. Microstructure analysis of the local contacts

Cross-sections of the samples passivated with SiN_x were carried out in order to study the formed eutectic layer after the alloying (Figure 4.8), demonstrating also the formation of a p^+ layer in the case of paste A. The thickness of that layer is ca. 1.4 µm, while the Al-Si eutectic maximum thickness is 14.4 µm. The Al-Si eutectic is more homogeneous in the case of paste A (Figure 4.8-a).

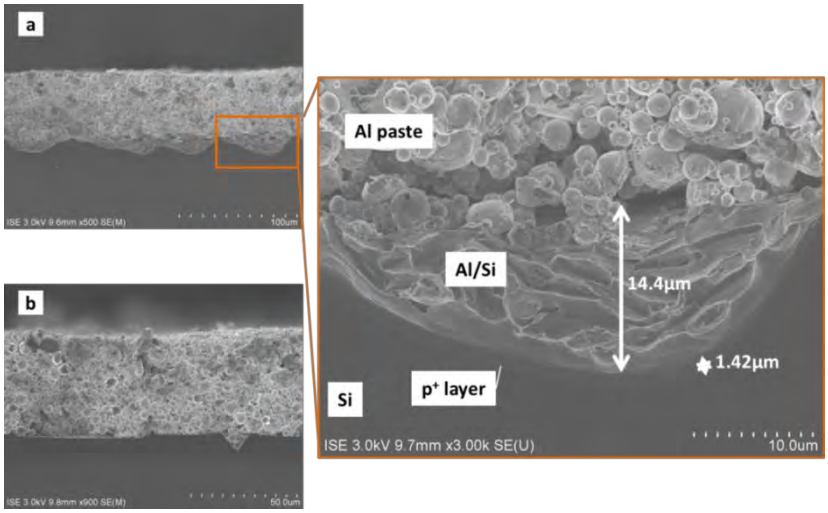

Figure 4.8. SEM picture of an FTC cross section for paste A (a) and paste B (b) with Al capping layer. The samples were fabricated with a SiN_x passivation layer and firing condition 2 (890°C at 4500 mm/min). The Al-Si eutectic penetrates the p-type silicon and creates a homogeneous p^+ layer of ca. 1.4 µm thickness in the case of paste A. For paste B, no p^+ layer could be observed with the SEM micrograph.

SEM micrograph for paste B (Figure 4.8-b) shows that the Al-Si eutectic penetrates the p-type Si bulk in a pyramidal shape. These structures are not continuous along the sample. That is corroborated by the optical micrograph (Figure 4.6-c), where the real contact area (dark areas) is much smaller than the area covered by the aluminum paste (red broken circle). Then, the SEM analysis confirms the formation of a homogeneous Al-BSF for paste A which leads to an outperformance in contrast to paste B.

The contact density area and thus the specific contact conductivity are higher for the newly developed paste A than for formerly investigated pastes. Furthermore, paste A delivers better contact conductivity than paste B for the same recombination velocity and firing condition. This could be attributed to the formation of a homogeneous local p^+-layer in case of paste A by microstructural analysis.

4.4. Manual screen printing

A manual screen printer was used to create a local back surface field with aluminum structures, carried out with different aluminum pastes on several substrates (silicon wafers and dielectric layers deposited on silicon).

4.4.1. Back surface field

First of all, a back surface field was created from a full pad, with the aim to compare it when created on polished silicon and on textured silicon.

4.4.1.a) Experimental

After the wet-chemically cleaning of the wafers (see Appendix A), they were printed by screen printing. Two layers of aluminum paste B were printed on 4 cm^2 p-type monocrystalline polished and textured silicon wafers (ρ=1Ωcm). The screens used to carry out the screen printing had a mesh with 48 μm polyester fine wires with 77 wires per cm^2. After printed, all the samples were dried in a muffle furnace at 250 °C for 10 minutes in order to burn the organic solvents from the paste before the firing process which was carried out at 890 °C in a 10 meters long belt furnace (from Isofoton S. A.) with a rate of 500 cm min^{-1}. Table 4.2 shows the range of temperatures inside the belt furnace. After the firing process, the cross-section of the samples was analyzed by FESEM (Field Emission Scanning Electron Microscope) images without encasing them into any resin to avoid resin signals. EDX (Energy Dispersive X-ray spectroscopy) was used to distinguish the aluminum to the silicon in the interface. SNMS (Secondary Neutral Mass Spectroscopy) was also carried out in order to corroborate the thickness measured with the SEM cross-section, and also to know the Al/Si atomic ratio concentration along the interface.

Temperature (°C)										
Z1	Z2	Z3	Z4	Z5	Z6	Z7	Z8	Z9	Z10	Z11
250	275	300	325	350	400	450	500	650	800	890

Table 4.2. Range of temperatures set in the 10 meters long belt furnace with 11 equal length zones.

4.4.1.b) Microstructure analysis

A silicon substrate screen-printed with aluminum paste B was used to carry out an EDX measurement after firing process (Figure 4.9). Two levels of brightness can be observed in the eutectic layer, as well as in the paste residuals, where the brightest zones belong mainly to aluminum and the darkest zones to silicon, which is in agreement with other experiments [99]. EDX measurements carried out on the

aluminum paste reveals silicon diffusion in the direction of this paste, apart from the obvious aluminum diffusion in the direction to the wafer surface forming the p^+ layer. On the other hand, the upper aluminum paste residuals were composed mainly by aluminum.

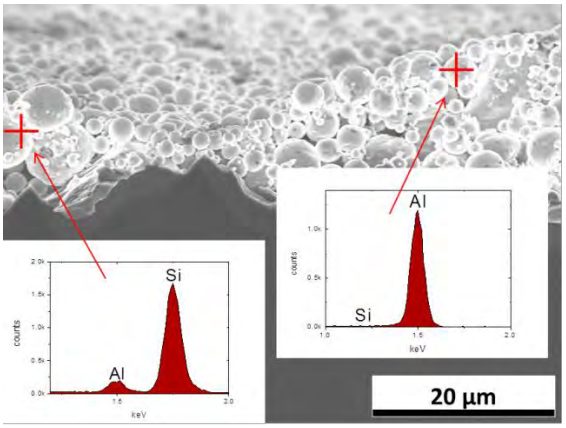

Figure 4.9. EDX of textured silicon screen-printed with aluminum paste B.

An EDX mapping of the cross-section of a polished silicon sample covered by aluminum paste and fired was carried out to analyze the distribution of the elements (Figure 4.10). A cavity of ca. 40 μm^2 was etched with gallium ions injection on the surface of the aluminum residuals paste with an enough depth to find the eutectic and p^+ layers. The displayed elements were silicon, aluminum and oxygen. Absorbed carbon was also presented, but was eliminated of the image to perform a better understanding of the rest of the elements. After firing, a compact and non-homogeneous eutectic layer between the BSF and the paste residuals was obtained. Aluminum was found in the paste residuals and the eutectic layer due to diffusion after firing peak temperature. Silicon was found also in the paste residuals due to the diffusion during heating up.

SNMS depth profile (Figure 4.11) confirms the presence of the silicon and aluminum during the interface, down the 20 µm of aluminum paste residuals, for a polished silicon sample. Oxygen was also found, forming part of the aluminum oxide shells of the paste particles due to high temperatures and an oxygen containing atmosphere during the firing step [32]. The normal percentage for the eutectic layer of Al-Si (12-88%) was not found in the SNMS graphic (Figure 4.11), due to the fact that the aluminum paste is composed by aluminum but also other organic solvents and glass frits, and it is not possible to the SNMS equipment to show only the signal of the aluminum.

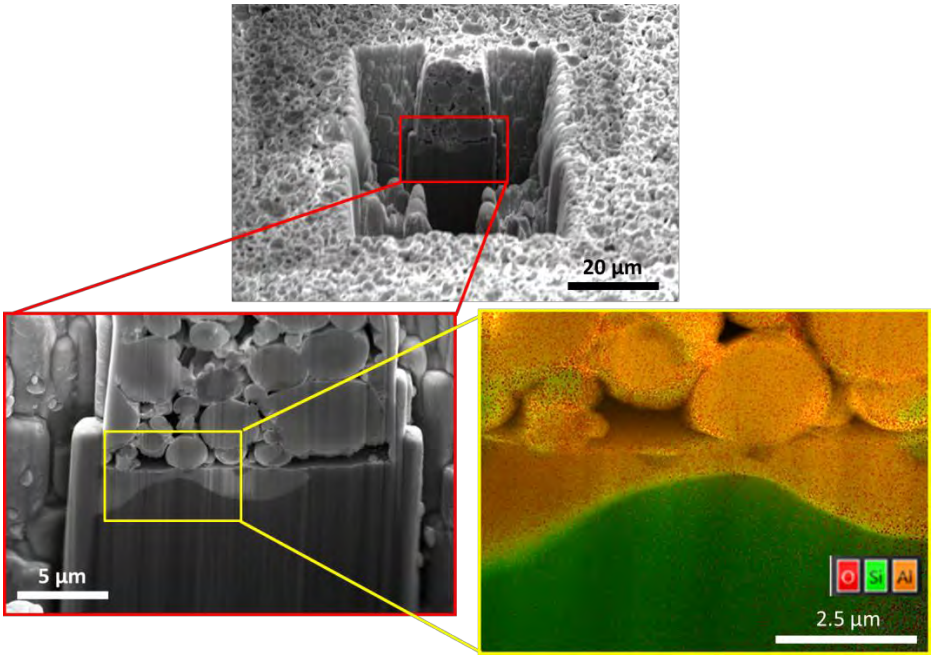

Figure 4.10. FESEM image of cross-section and EDX mapping for a polished p-type silicon sample with aluminum paste screen-printed and fired.

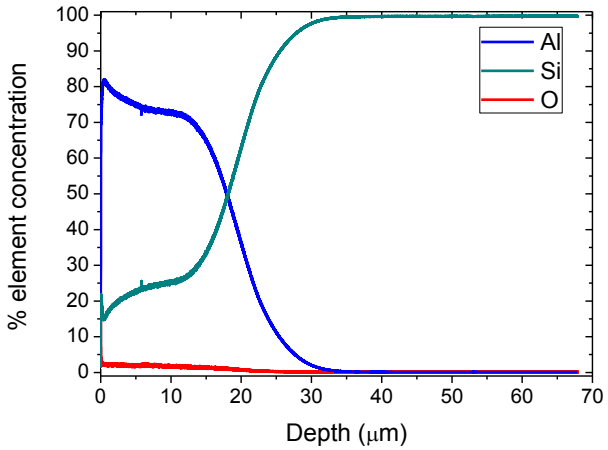

Figure 4.11. Depth profile registered for a polished silicon sample. Aluminum concentration decreases with the depth while silicon concentration increases. At ca. 20 µm (interface between paste residuals and eutectic layer) silicon concentration begin to be higher than aluminum.

4.4.1.c) Comparison between polished and textured p-type silicon

Cross-sections of aluminum printed samples were measured after firing by FESEM to confirm the presence of the p^+-layer below the eutectic one. In the case of polished silicon wafers (Figure 4.12), a non-uniform eutectic layer below the paste residuals is shown with a maximum thickness of 4.1 µm. The p^+-layer was detected in a regular shape under the eutectic *islands* reaching a thickness of 1.2 µm. For textured silicon wafers (Figure 4.13), uniform layers of eutectic and p^+-layer are shown, reaching 6.47 µm of thickness. Comparing textured with polished wafers, the thickness of the Al paste residuals after firing was higher for textured samples than polished ones due to the more ability to spread on polished wafers while the sample was drying. For that reason, there were obtained also higher thickness of p^+-layer for textured silicon wafers. Furthermore, for polished silicon, the diffusion of the paste could be more difficult due to the process of polishing of the surface.

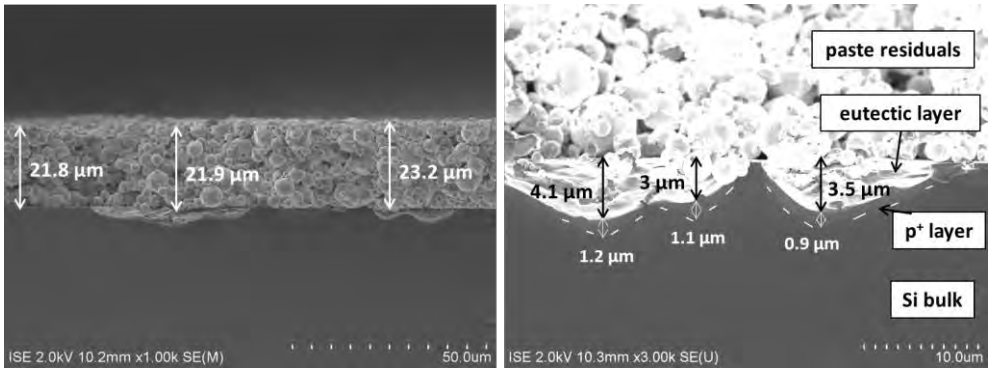

Figure 4.12. FESEM images of an aluminum screen-printed polished p-type Si.

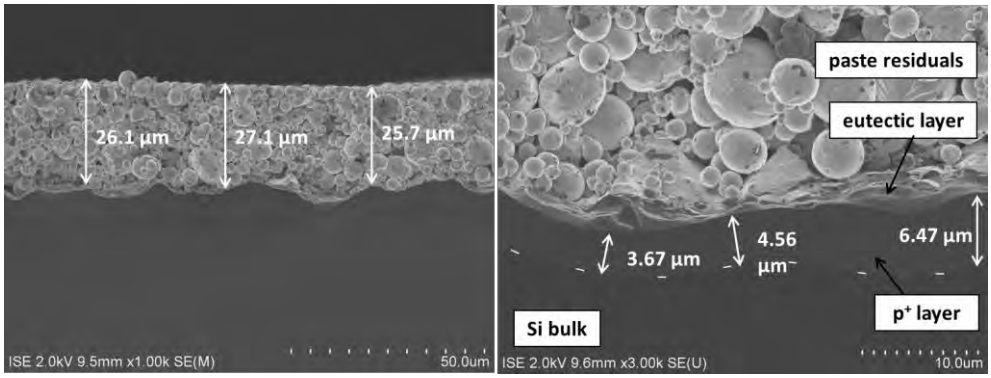

Figure 4.13. FESEM images of an aluminum screen-printed textured p-type Si.

4.4.2. Local contact formation.

After back surface field was created (section 4.4.1), different layouts (see APPENDIX B) were developed with diverse structures, with the aim to form a local back surface field. To corroborate that, contact resistance were measured and FESEM pictures were taken as well.

Subsequently the wet-chemically cleaning (see Appendix A) of the different p-type silicon <100> textured and as-cut wafers (with 180-190 and 200 µm thickness respectively and 1-3 Ohm cm), some of them were used as substrates to print on them aluminum lines by screen-printing method, and others were coated before printing with diverse dielectric layers using thermal treatments and magnetron sputtering technique.

In general, screen-printing was carried out onto the different substrates using layouts whose line widths varied from 0.35 to 1.5 mm and three aluminum pastes called B, T1 and T2. Then, the samples were dried in a muffle at 250ºC during 10 minutes and the process was repeated. In that way, every line was printed with two layers of aluminum paste. The mass deposited after drying, shown in Figure 4.14, increases with the line width, as it was expected. After the lines were dried, the firing of the samples was carried out at 950ºC in a tubular furnace.

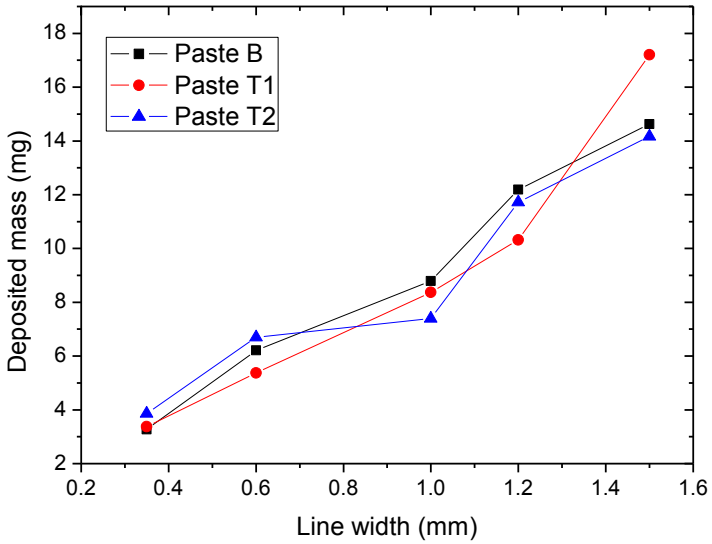

Figure 4.14. Deposited mass of aluminum after drying the samples.

The morphology of the lines was studied after carrying out optical microscope pictures, which were used to measure the real width and length of the aluminum lines after printing. These values were essential to calculate the specific contact resistance of the metal contacts formed. This resistance was determined by the TLM method. Every sample was made twice, that is, it was repeated so that a good accuracy of the process could be reached.

FESEM images were taken to some samples to observe the relationship between the p^+-layer obtained below the Al-Si eutectic and the specific contact resistance values. Because of that, cross-sections were first prepared cutting the samples manually and introducing them this way into the microscope, without encasing in any resin to avoid other undesirable signals.

4.4.2.a) Silicon wafers as substrates

At first, as-cut p-type silicon wafers were used as substrates to carry out the screen printing onto them. A wide range of line widths was studied: 0.35, 0.6, 1, 1.2 and 1.5 mm. Images taken with an optical microscope are shown in Figure 4.15. It is observed that the two layers are well assembled one over the other. With pastes T1 and T2, blue zones appeared around the aluminum lines, but it did not occur when printing with paste B. To study this, EDX measurements were carried out to those samples.

Figure 4.16 shows a graphic of the oxygen concentration weight percentage against the distance from the end of one aluminum line to the beginning of the following, overlapped on the optical image of the studied sample, in which aluminum lines were printed with paste T1. It can be noticed an increment of oxygen concentration in the blue zones. As the only change compared with other samples is the aluminum paste, it could be attributed to the more quantity of oxygen in pastes T1 and T2 due to the oxidation of the aluminum particles. To corroborate this, EDX measurements of samples printed with paste B were carried out and no oxygen was found between the aluminum lines; it was composed only by silicon (Figure 4.17).

Line width (mm)	Paste B	Paste T1	Paste T2
0.35	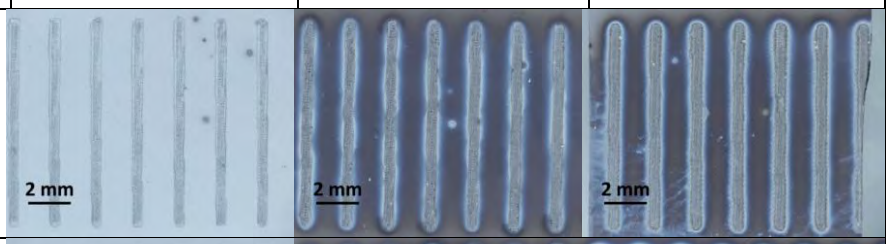		
0.6	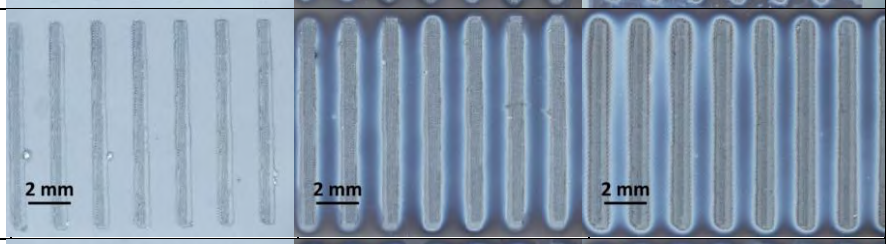		
1	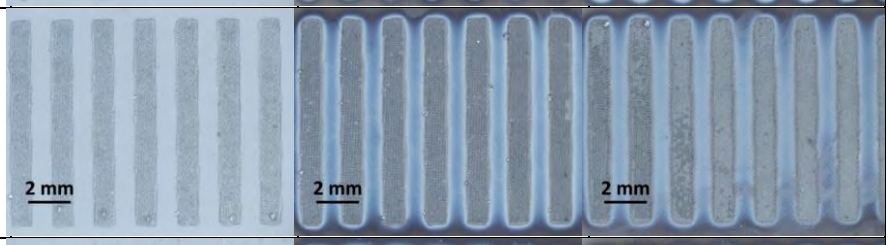		
1.2	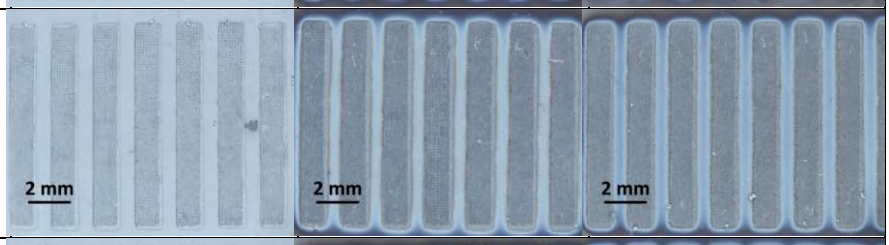		
1.5	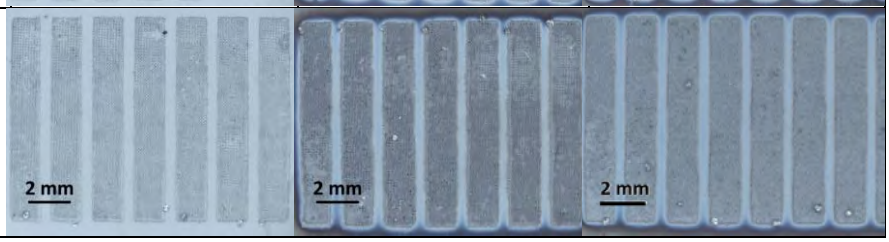		

Figure 4.15. Optical microscope images for the different line widths using the three aluminum pastes on as-cut silicon substrates.

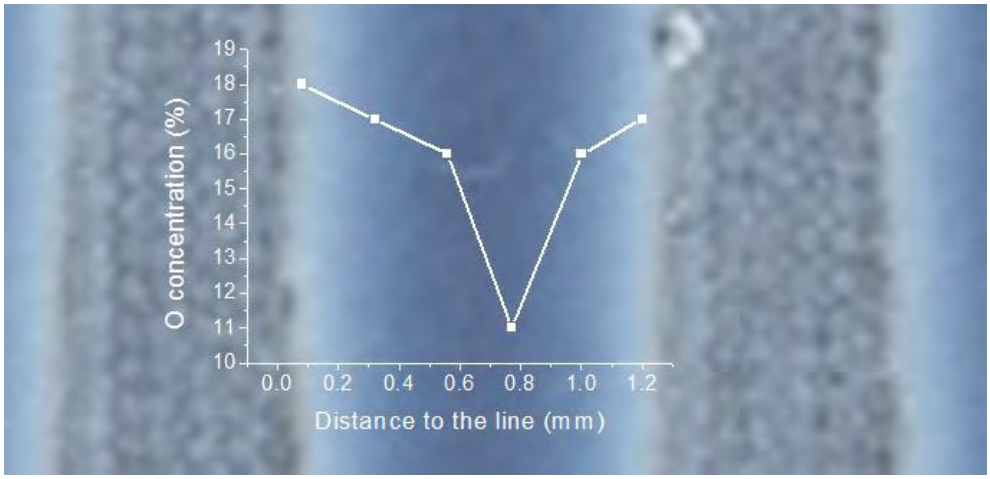

Figure 4.16. Oxygen concentration (weight %) on the silicon zone between two aluminum lines of 0.6 mm width printed with paste T1 on as-cut silicon obtained by EDX.

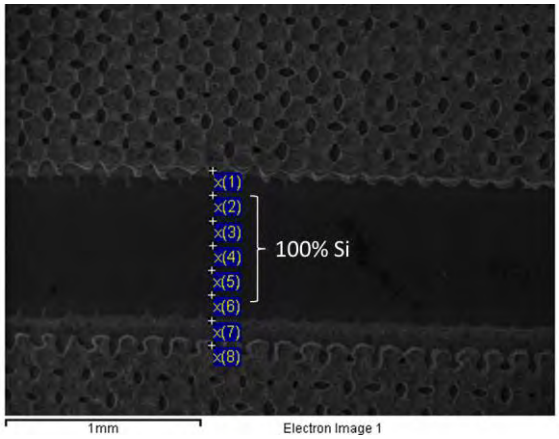

Figure 4.17. For samples printed with paste B, the oxygen concentration between the aluminum lines was 0% weight, being this part composed only by silicon. Example of lines of 1.2 mm printed on as-cut silicon with paste B.

Cross-sections of the samples were carried out in order to study the formed eutectic layer after the alloying (Figure 4.18). The formation of a p^+-layer is demonstrated in these FESEM images as well, being uniform along the line as it is shown on the lefts side of the Figure for the three pastes. On the right side, a zoom of the eutectic-p^+-layer region is detailed, where the thickness of the LBSF obtained was around 12 μm for the three aluminum pastes.

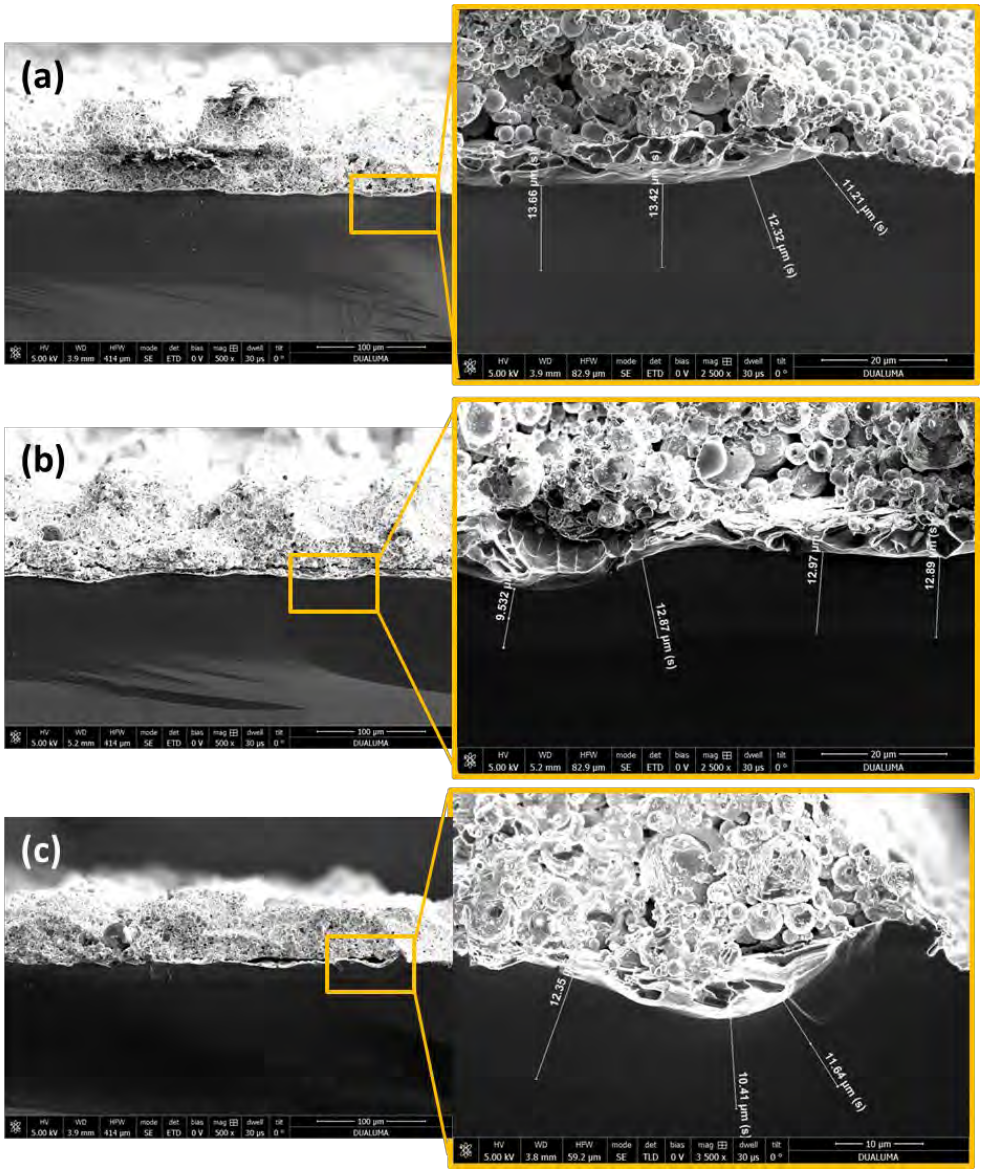

Figure 4.18. FESEM images for aluminum lines of 1.5 µm of width printed with pastes B (a), T1 (b) and T2 (c).

Specific contact resistance was calculated by the TLM method for the different line widths and aluminum pastes. The medium and best results are represented to prove the reproducibility of the process (Figure 4.19). The results are comparable with others obtained by the use of the automatic screen-printing method and it can be

confirmed that manual screen-printing is a low-cost feasible technique to create local contacts.

For the two pastes B and T1, the best contact resistance was obtained with line width of 1.2 mm. That is why in the next section it was taken this line width to compare the local back surface field obtained by usinf of different dielectric layers.

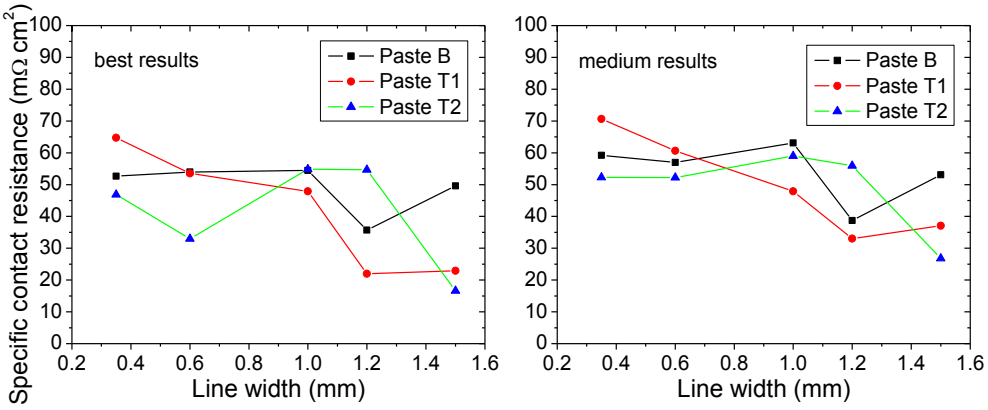

Figure 4.19. Specific contact resistance for aluminum lines printed on as-cut silicon with three different pastes.

4.4.2.b) FTC method to create LBSF using different dielectric layers

At first, monocrystalline p-type silicon wafers were used as substrates to be coated by several dielectric layers following different techniques, which are described below:

- SiO_2: this layer was created onto the silicon wafers by the thermal oxidation at 950ºC during 90 minutes in a tubular furnace under air atmosphere. The thickness of the layer created was ca. 80 nm.

- SiO_2/ZnO: on a first thermally grown SiO_2 layer, a ZnO ceramic target was used as source to sputter the sample and obtain a homogeneous layer of ZnO, with a thickness of 140 nm deduced by XPS profile. A pressure of $1.2 \cdot 10^{-4}$ mbar was maintained in the magnetron sputtering main chamber during deposition, and a power of 150 W was set, at room temperature. The thickness of the created stacks was ca. 220 nm.

- SiriON: these stacks were created by PECVD at the Fraunhofer ISE laboratories as described in section 3.3.3. The thickness of the stack was ca. 85 nm.

Once the dielectric layers were created, the screen-printing of lines was carried out to the samples with the three same fire-through aluminum pastes used in the previous section, named B, T1 and T2. The samples were printed twice between each drying, and afterwards were fired in a tubular furnace at 950ºC. As the previous medium results on as-cut silicon wafers proved that the best specific contact resistances were obtained with lines of 1.2 mm width, this time it was compared this width for all the pastes and the different dielectric layers created.

Optical microscope was used to obtain pictures of the different structures (Figure 4.20). Blue zones was observed for the samples printed with pastes T1 and T2, but also for the sample coated with the SiO_2/ZnO stack by magnetron sputtering. Now, this oxygen is belonged to the dielectric layer due to the high amount of this element in the composition of the stack.

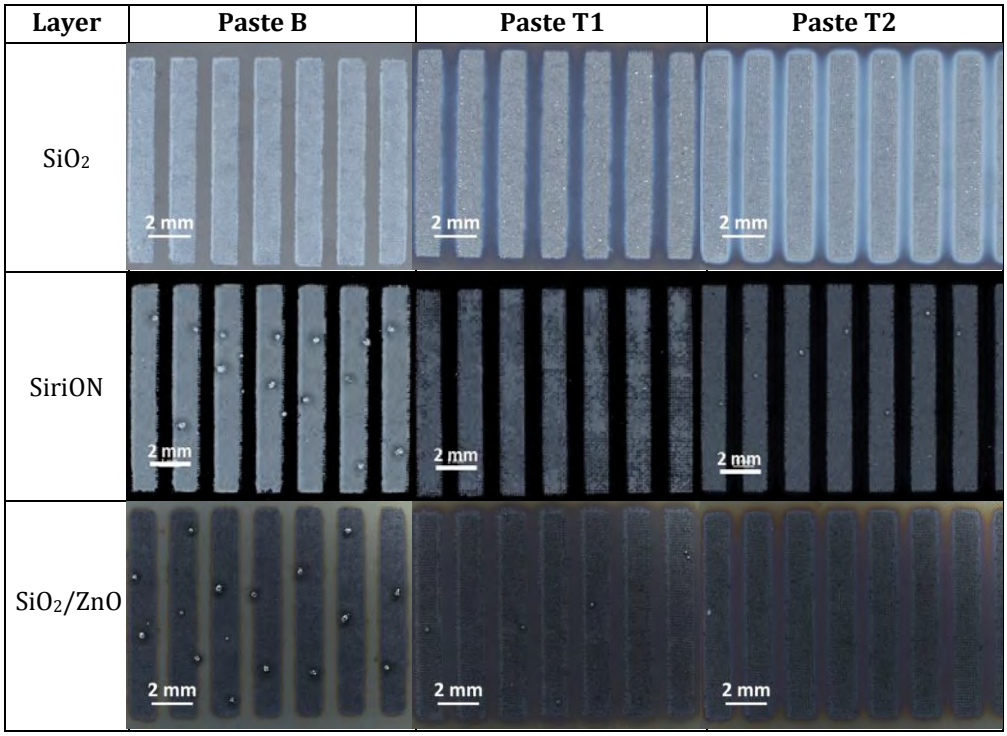

Figure 4.20. Optical microscope images for 1.2 mm of line width printed with the three aluminum pastes on several dielectric layers.

The specific contact resistance was calculated for aluminum structures with line width of 1.2 mm and 10 mm long, printed with the three different aluminum pastes on the dielectric layers previously created by magnetron sputtering (Figure 4.21). It can be observed that paste T2 shows advantages compared to the other two pastes.

Regarding the dielectric layers, the best specific contact resistance is reached for lines printed with paste T2 using SiriON and SiO_2 as passivating layers. Then, having in mind that SiriON layers lead to the best passivation results (see section 3.3.3), it could be concluded that the best results regarding the contact resistance and also the quality of the passivation are achieved when using paste T2 and SiriON as passivation layer.

Moreover, FESEM images were taken for printed lines of 1.2 µm of width on the three dielectric layers studied (Figure 4.22). The p^+-layer is clearly seen in the three pictures and its thickness may be related to the specific contact resistances measured before, and shown in Figure 4.21. For the best specific contact resistance (lines printed on the SiO_2 layer), the p^+-layer obtained was uniform and the thickness was the highest in comparison with the other two samples (lines printed on SiriON and SiO_2/ZnO layers). For lines printed on SiriON, the p^+-layer was less uniform and, finally, for the lines printed on the SiO_2/ZnO stacks, this p^+-layer was obtained in a non-uniform way, with the lowest value of thickness regarding the others. Then, the uniformity of the p^+-layer was related to the specific contact resistance.

Additionally, the specific contact resistance obtained by using manual screen-printing is comparable when using automatic screen-printing (Figure 4.23), in relation with the SiriON dielectric layer and 1.2 mm of line width printed with paste B.

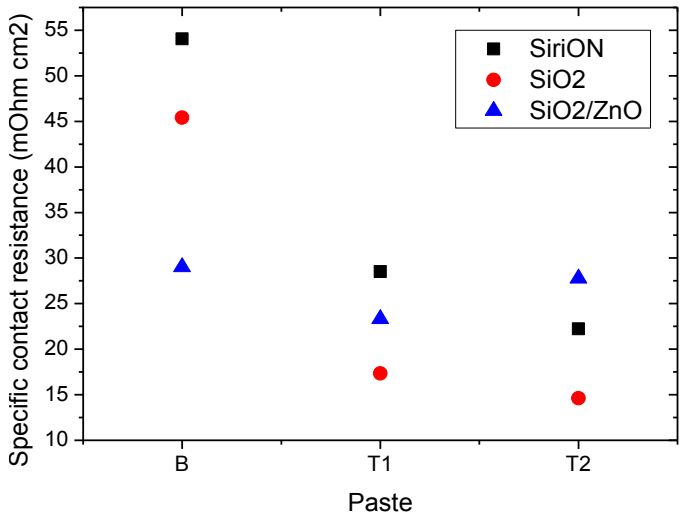

Figure 4.21. Best results for the specific contact resistance for aluminum structures of 1.2 mm width printed on different dielectric layers by the FTC method.

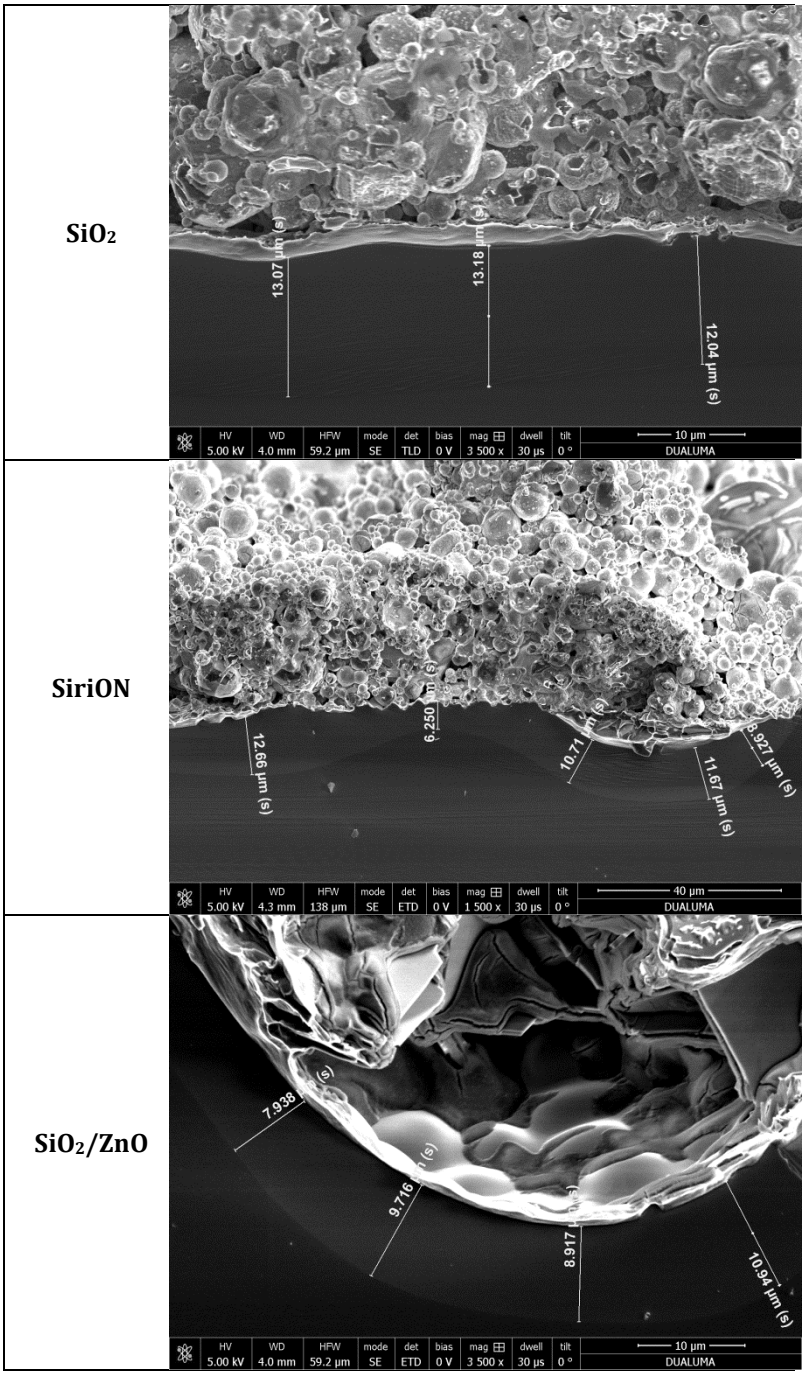

Figure 4.22. FESEM cross-sections for lines of 1.2 mm width printed with paste T2 on different layers on silicon.

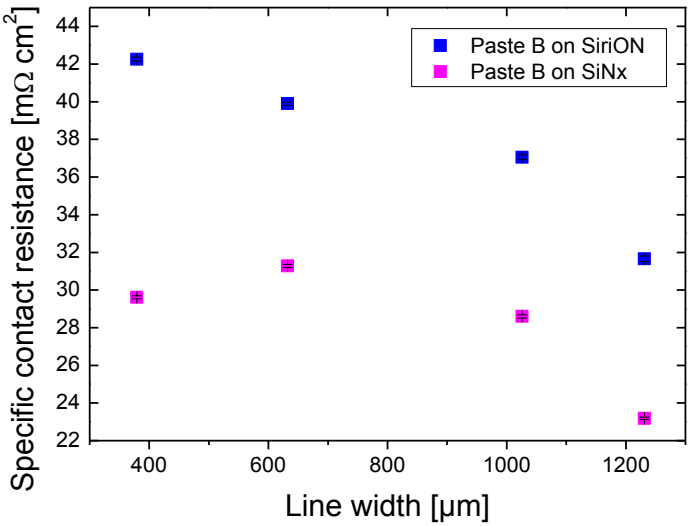

Figure 4.23. Specific contact resistance for paste B on SiriON and SiN_x passivation layers using automatic screen-printing during the stay at Fraunhofer ISE.

5

Dispensing-printed local Al-alloyed structures

In this chapter, a dispensing robot was used to create aluminum structures on silicon wafers, with the same target when screen printing was used in previous chapters. A local back surface field was created and its thickness was measured. The contact resistance was compared for different aluminum pastes. To complete the study, a microstructure analysis was carried out.

5.1. Introduction

Thin silicon wafers are a way to reduce costs in the raw material, but the bowing of such wafers after metallization causes its breakage in most of the cases and also *microbreaks* in the structure affecting to the lifetimes and to the efficiency of the final solar cell [100,101]. This effect can be reduced by using non-contact metallization techniques like dispensing technology as many authors reported for obtaining the front electrodes with silver paste [38, 39,102].

In this chapter, dispensing technology is demonstrated to be feasible for the formation of local back surface field (LBSF) on different silicon p-type substrates (textured and polished) by the use of three different aluminum pastes. Different dielectric layers were coated on silicon substrates using thermal oxidation and magnetron sputtering, with the aim to print aluminum lines on these layers and obtain the LBSF formed by the fire-through contact method. The specific contact resistance for the different structures was obtained to verify the formation of the p^+-layer, and for the possible use of this structures as back local contacts in silicon solar cells. The microstructural interface obtained between aluminum and silicon is also presented, to verify the p^+-layer formation and compare the thickness of the eutectic layer obtained for the different substrates and aluminum pastes.

5.2. Aluminum pastes

The function of the rear side conductor is to act as a second electrode in the photovoltaic solar cell. Aluminum thick film technology is used to generate a p-type region with aluminum doped silicon sites, which function is acting as a back-surface field, enhancing the efficiency of the cell.

Aluminum pastes are being used in photovoltaic industry with the aim to reduce costs versus silver pastes. In this point, the different aluminum pastes used in the following work are compared. These aluminum pastes were used for the formation of the BSF in p-type silicon wafers by the FTC method. There are glass frits present in these Al pastes to obtain better sintering properties of the contact layer [32], due to these glass frits influence the Al-Si interaction modifying the surface tension of the molten liquid of Al [103], and homogenizing the diffusion process. They are also important to allow the paste go throw the passivation layer, without the requirement of any etching of this layer. Some elements like Bismuth, Calcium and Magnesium, at low concentration (i.e. Bi~0.3 at%, Ca~1.5 at%, Mg~3.5 at%) are able to almost half the surface tension of liquid Al [104-106].

The same aluminum pastes applied in section 4.4 were used to create aluminum structures by dispensing technology. No modifications were made in order to change the composition of the pastes.

A specific amount of each aluminum paste was first casted in a glass, and then heated at 250°C to allow the measurement with the scanning electron microscope. Pictures are shown in Figure 5.1. The aluminum paste named T2 has bigger size of particles than the other two pastes. Concretely, paste T1 has <5% weight of lead-free frits, while T2 has 1-10%. This fact makes difficult the path of this paste through the nozzle of the dispensing robot to print the aluminum structures. For this reason, this paste was heated before printing by the immersion of the syringe with the paste inside, in a water bath at 80ºC during 5 minutes.

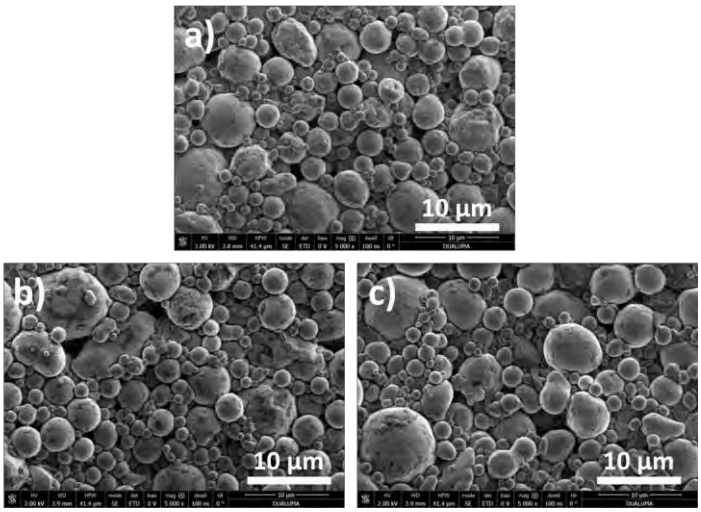

Figure 5.1. FESEM images of paste B (a), T1 (b) and T2 (c)

5.3. Program

The robot used to carry out the dispensing printing (drop on demand technique) was the model F7900N, from Fisnar. The main unit is connected to a 'teach pendant' (Figure 5.2), and to the frequency unit to supply the air at the chosen pressures.

Before programming the robot to dispense a dot of material, the dispensing nozzle must be jogged to the desired XYZ location. When a program is set, the series of instructions are stored in the main unit memory and each instruction is stored in a

numbered memory address. When a program is run, the robot steps through each memory address in sequence and executes the instruction found there.

In this thesis, lines of different aluminum pastes were printed by the dispensing of very close dots so that the final appearance was a line. The instructions sent to the robot to run the program are described in Table 5.1.

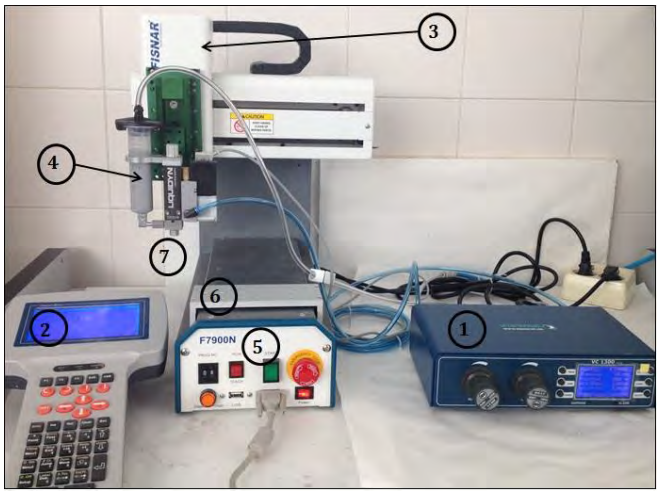

1. Frequency unit

2. Teach pendant

3. Dispensing head

4. Syringe with Al paste

5. Robot main screen

6. Wafer holder

7. Dispensing nozzle

Figure 5.2. Dispensing robot equipment

`001 Line Speed`	Sets the speed of the dispensing head
`002 Line Start`	Related to the XYZ position to start the line
`003 Line Passing`	XYZ position in the middle of the line
`004 Line End`	XYZ position related to the end of the line
`005 Step & Repeat Y`	Sets the number and the distance between the lines
`006 End Program`	Step to end the program

Table 5.1. Program to print lines with a desired distance between them

5.4. First dispensing on polished and textured silicon

The aluminum paste B was used to compare the thickness of the p^+-layer, obtained on textured and polished monocrystalline p-type silicon wafers after the proper wet chemically cleaning (see Appendix A). Lines of 1.5 mm width were printed on these wafers by dispensing technology.

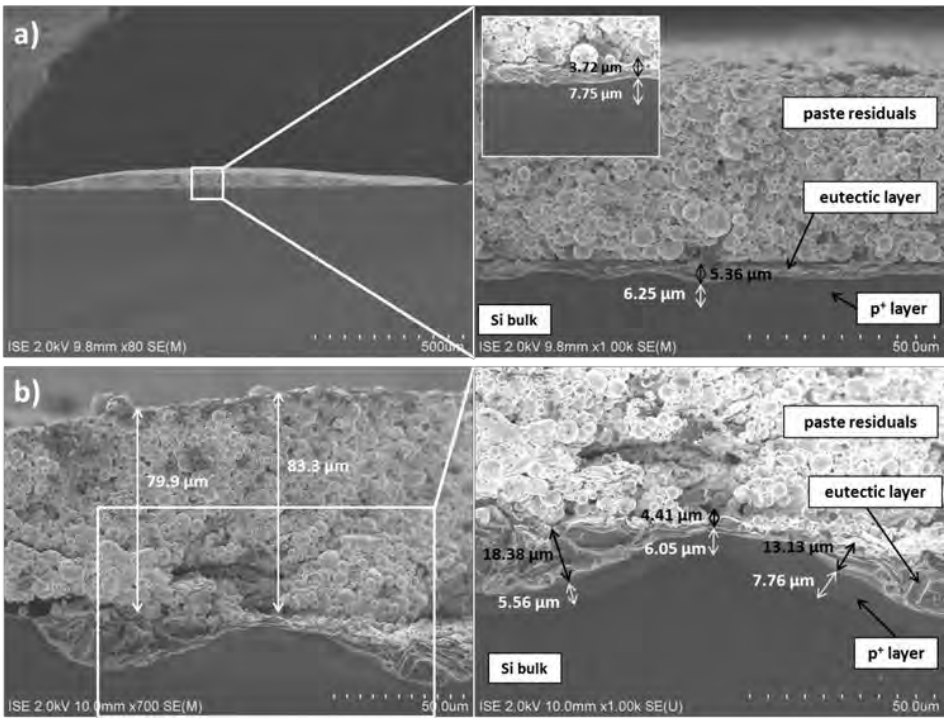

Figure 5.3. FESEM micrographs of cross-sections of polished (a) and textured (b) p-type Si wafer dispensing-printed with aluminum paste B

As FESEM micrographs reveal (Figure 5.3), the p^+-layer was formed both on textured and polished wafers below the eutectic layer, taking a similar value for both type of substrates, even though the thickness of aluminum residuals after firing was thinner for polished wafers.

5.5. Al-printed lines

Different aluminum pastes were used to print lines on silicon p-type wafers after the wet chemically cleaning (see Appendix A). The pastes were named as B (from *Ferro*), T1 and T2 (both from *Toyo Aluminum K.K.*). The mass of the deposited aluminum paste was measured after deposited and also after drying (Table 5.2). It was deposited more amount of mass of paste when using paste T1 and paste T2, due to their higher particles size.

Aluminum paste	Mass of wet paste (mg/cm²)	Mass of dried paste (mg/cm²)
B	13.0	9.62
T1	25.6	20.2
T2	32.6	28.7

Table 5.2. Specific mass of aluminum paste deposited for the three different pastes and the diameter of the nozzle of 150 µm.

The ability of the equipment to print dots allows the printing of lines by setting the frequency of such dots and the speed of the dispensing head, as it is shown in Figure 5.4 and Table 5.3, for dots and lines printed on p-type monocrystalline silicon with paste B using a nozzle with 250 µm of diameter. Pictures were taken with an optical microscope after drying the paste and a process of firing at 950ºC.

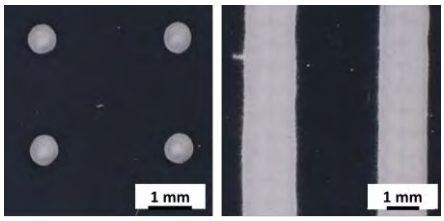

Figure 5.4. Optical microscope images for dots and lines printed with paste B using a nozzle of 250 µm of diameter.

Structure	Air pressure (Bar)	Frequency (Hz)	Diameter/line width (µm)
dots	3.42	27	772
lines	3.55	150	1470

Table 5.3. Program parameters and geometry of the printed structures showed in Figure 5.4.

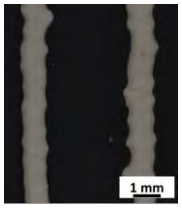

Figure 5.5. Optical microscope image for lines printed with paste B using a nozzle with 150 µm of diameter.

With the aim to reduce costs a nozzle with 150 µm of diameter was used, spending less amount of aluminum paste. Then, the width of the lines becomes smaller (Figure

5.5), taking a value in this case of 920 µm vs the 1470 µm of the line printed with the nozzle of 250 µm of diameter.

5.6. LBSF formed on monocrystalline p-type silicon wafers

In this section, the three aluminum pastes described in Table 5.2 are used to create a local back surface field on as-cut and textured silicon wafers, both monocrystalline p-type Si <100>, 1-3 Ωcm resistivity and 180-190 µm thickness. First of all, a proper wet-chemically cleaning was carried out (see Appendix A). Specific contact resistance was calculated and compared between the different pastes, and optical microscope and SEM pictures were taken as well to check the formation of the LBSF.

After the firing at 950ºC, the optical microscope was used to take pictures of the obtained structures with the three aluminum pastes using the 150 µm diameter nozzle on as-cut silicon wafers (Figure 5.6). The lines remain attached to the silicon substrates in the three cases. For the B paste, as it is more liquid than the others, the lines become wider and spread better onto the substrate.

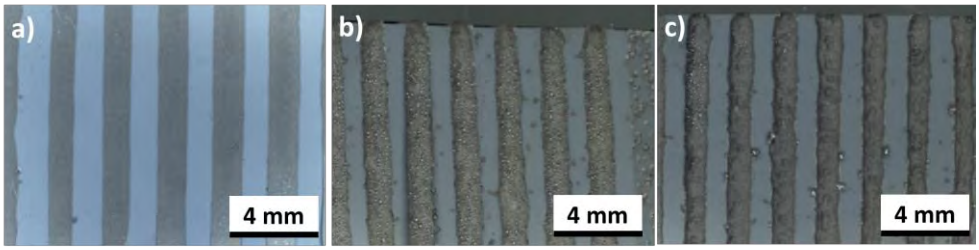

Figure 5.6. Optical microscope images for lines created on as-cut silicon substrates with paste B (a), T1 (b) and T2 (c).

Specific contact resistance was obtained by TLM (Transmission Line Measurement) and gave the best value to the aluminum paste T2 (Table 5.4). Comparing the pastes T1 and T2, the second one offered the best contact resistance on silicon. SEM pictures were taken with the aim to measure the thickness of the eutectic layer for the best samples, printed with T1 and T2 pastes (Figure 5.7). As it is shown in the picture for the paste T2, that paste was removed unintentionally from the silicon after the sample was encapsulated in resin to allow the cut for obtaining the cross-section to take the picture. The eutectic layer was measured for both samples, taking a value of 62 µm and 74 µm for the samples printed with paste T1 and T2, respectively.

Al paste	Line width (mm)		ρ_c (mΩcm²)	
	Average value	Best value	Average value	Best value
B	1.222	1.178	193	132
T1	1.250	1.236	258	202
T2	1.126	1.137	146	96

Table 5.4. Specific contact resistance measured for the three different aluminum pastes on as-cut silicon substrates.

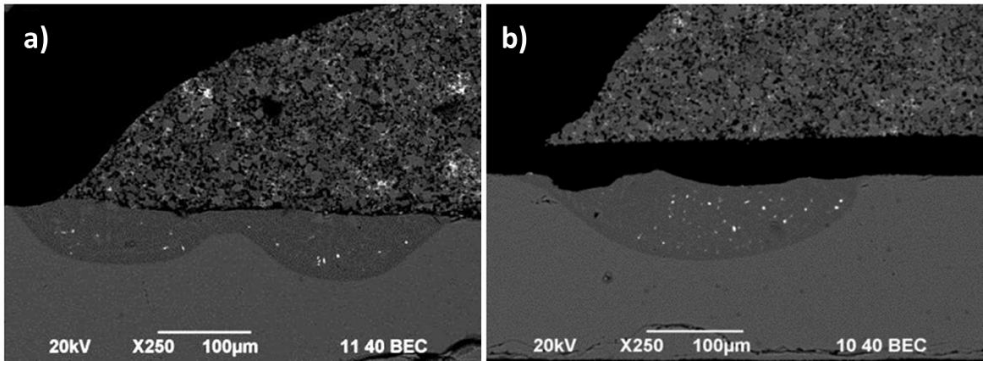

Figure 5.7. SEM picture of a cross-section obtained after printing with paste T1 (a) and paste T2 (b) on as-cut silicon substrates.

The same procedure to print lines was carried out on textured silicon substrates, with the same three aluminum pastes. Lines created with paste B were unstacked from the substrate after the firing, so the electric parameters were only measured with the samples printed with pastes T1 and T2 (Table 5.5).

Al paste	Line width (mm)	ρ_c (mΩcm²)	
		Average value	Best value
T1	1.202	146	111
T2	1.218	54	54

Table 5.5. Specific contact resistance measured for two aluminum pastes on textured silicon substrates.

SEM images shown in Figure 5.8 exhibit both cross-sections for lines formed with pastes T1 and T2. As it can be noticed in Figure 5.8 (b), the line formed with paste T2 was unstacked from the substrate after the insertion of the sample in a resin for the measurement. In the other case, the image was taken with a FESEM and the measurement was carried out without insert the sample in any resin. The thickness of the eutectic layer formed after firing at 950ºC was measured by SEM, and took a value of 35 µm and 103 µm for paste T1 and T2 respectively, which is in accordance with the

values of specific contact resistivity shown in Table 5.5. In Figure 5.9, a zoom of the eutectic region is shown for a sample printed with paste T2 on textured silicon, where the p^+-layer is clearly seen below the eutectic. The more the eutectic layer became, the more the contact between aluminum and silicon is, and thus the contact resistivity decreases. As it can be seen in Figure 5.10, the Al/Si ratio in the p^+-layer was similar for samples printed with both pastes T1 and T2. These ratios were obtained by EDX measurements.

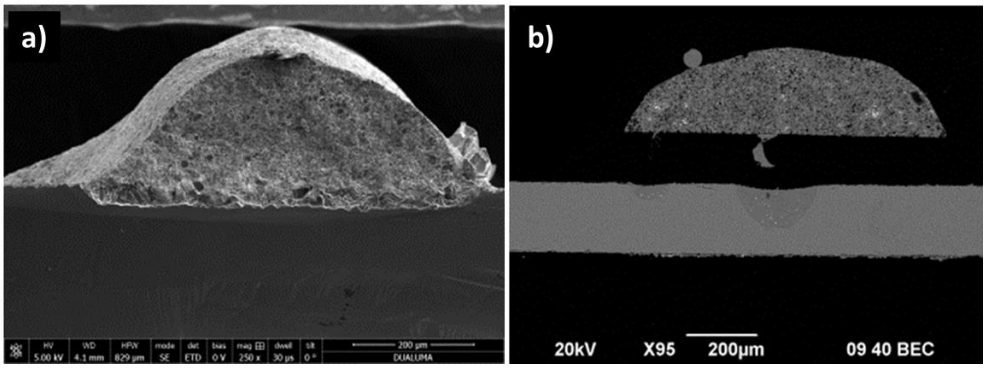

Figure 5.8. SEM picture of a cross-section obtained after printing with paste T1 (a) and paste T2 (b) on textured silicon substrates.

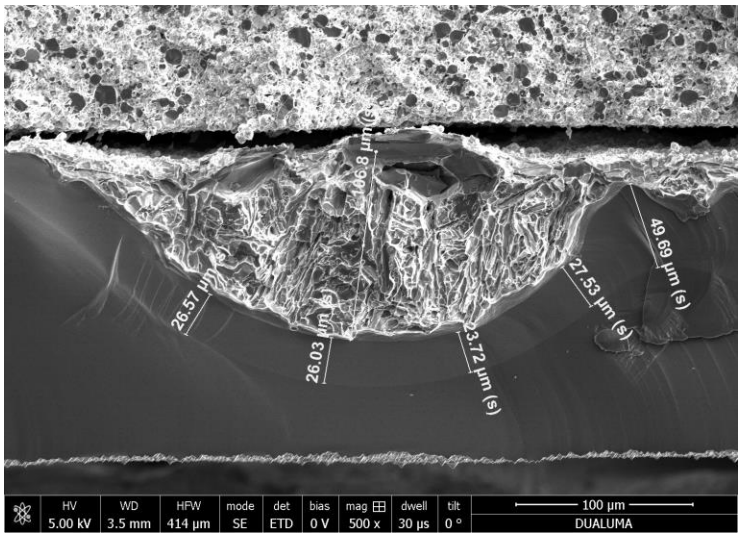

Figure 5.9. Zoom of the eutectic and p^+-layer regions of a sample printed with paste T2 on textured silicon.

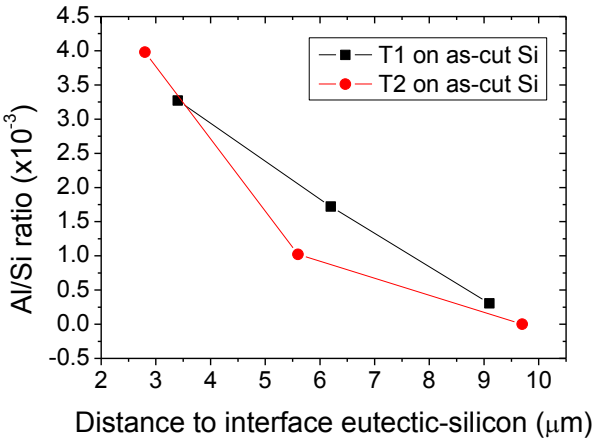

Figure 5.10. Comparison of Al/Si ratios of p⁺-layer for lines printed with aluminum pastes T1 and T2 on as-cut silicon substrates obtained by EDX measurements.

Summing up, for both as-cut and textured silicon, the aluminum paste T2 allowed the obtaining of the best specific contact resistance. Comparing the resistance values for aluminum lines printed on textured silicon and as-cut silicon, there was obtained lower values for lines printed on textured silicon. This result is also evidenced by the EDX study carried out for samples printed with paste T2 (see Figure 5.11), where for the same distance between the EDX point and the interface eutectic-silicon (p⁺-layer), for textured samples it is reached a higher value of Al/Si ratio.

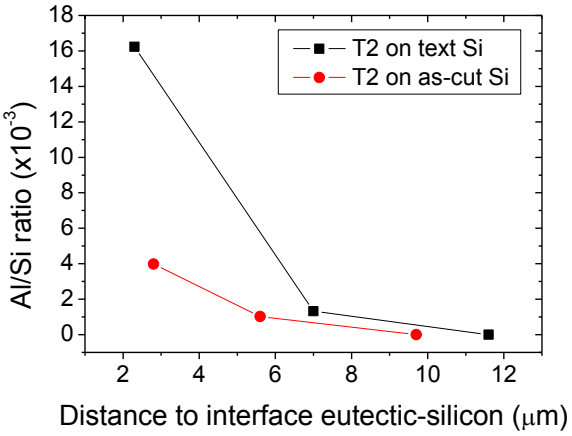

Figure 5.11. Comparison of Al/Si ratios of p⁺-layer for lines printed with aluminum paste T2 on textured and as-cut silicon substrates.

5.7. LBSF formed by fire through contact method

Dielectric layers were created on silicon wafers with the aim to passivate the surface. These layers were obtained by using different methods such thermal oxidation, magnetron sputtering and plasma enhanced chemical vapor deposition (PECVD). Then, aluminum lines were printed with the dispensing equipment on the layers created, using the three pastes described in Table 5.1, and a firing process was carried out after that making use of the fire through contact (FTC) method, with the aim to create local metal contacts.

5.7.1. LBSF on SiO_2/SiN_x stack

Thermal silicon oxide was grown on textured p-type monocrystalline silicon wafers, at 900ºC, during 90 minutes under atmospheric pressure in a tubular furnace. After the thermal oxide growth, the magnetron sputtering was used to create SiN_x layers on the silicon oxide during 60 minutes, at room temperature, by a ceramic SiN_x target as source. The process was carried out with a power supplied of 150 W and a working pressure of $1.2 \cdot 10^{-4}$ mbar.

After the dielectric layer was created, a nozzle of 150 µm of diameter was used to print lines on it (Figure 5.12). For the paste T1, the air pressure was fixed at 3.46 bars and the frequency at 160 Hz, printing the lines at a speed of 45 mm/s. On the other side, for paste T2, the air pressure was similar (3.84 bars), but the frequency had to be decreased to 140 Hz and the speed was increased to 60 mm/s. This fact is due to the size of the particles in paste T2, which is bigger than the ones in paste T1. Thus, the paste T2 needs more speed to spread in a proper way on the substrate. Lines were printed with both pastes, with 2 mm of distance between them. After printing, the samples were dried and fired at 950ºC in a tubular furnace.

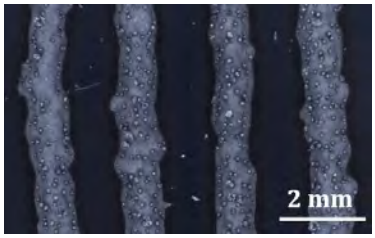

Figure 5.12. Optical microscope image for lines printed on SiO_2/SiN_x stack with the aluminum paste T2.

For the same line length of 11 mm for both aluminum pastes, the results are shown in Table 5.6. Best contact resistance value was achieved for paste T2, for similar line

widths. The p^+-layer obtained with this paste was homogeneous under the eutectic Al-Si, as Figure 5.13 shows, which confirms the existence of the LBSF.

Al paste	Line width (mm)	ρ_c (mΩcm^2)
T1	1.273	459
T2	1.125	195

Table 5.6. Specific contact resistance measured for two aluminum pastes on SiO_2-SiN_x layers.

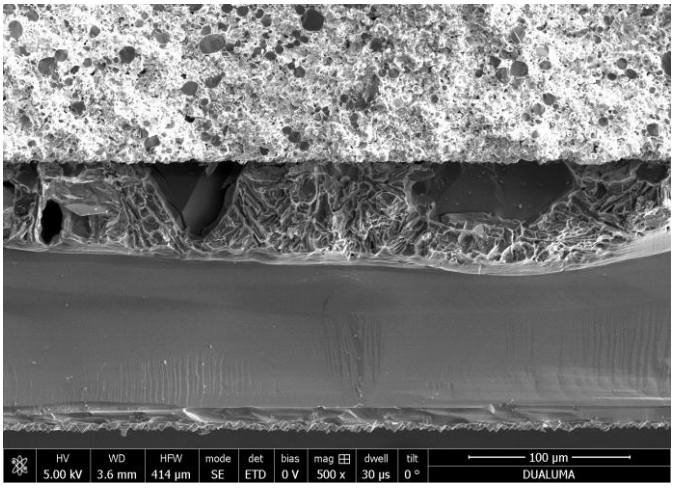

Figure 5.13. Zoom of the eutectic and p^+-layer regions of a sample printed with paste T2 on SiO_2/SiN_x layer on silicon.

5.7.2. LBSF on SiriON stacks

SiriON (silicon-rich oxynitride) layers capped with SiN_x were grown on p-type monocrystalline silicon wafers by the PECVD method, at Fraunhofer ISE facilities (see section 3.3.3) during the stay of the author of this thesis there. Lines of 11 mm length were printed with the two aluminum pastes T1 and T2 on these stacks, and the contact resistance was calculated from the TLM technique results (Table 5.7). The best value was achieved for the paste T2, and it could be related to the detachment of the lines from the substrate when the paste T1 was used, as can be seen in Figure 5.14. The eutectic and the p^+-layer shown in Figure 5.15, where the aluminum line is not shown due to the detachment after preparing the sample for the SEM picture, confirm the existence of the LBSF.

Al paste	Line width (mm)	ρ_c (mΩcm^2)
T1	1.218	320
T2	1.221	92

Table 5.7. Specific contact resistance measured for two aluminum pastes on SiriON layers.

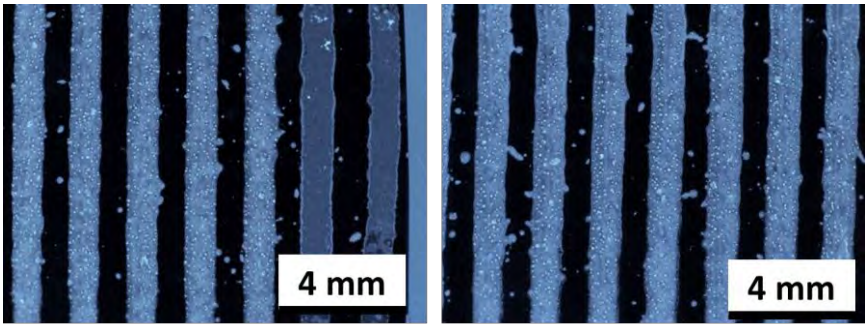

Figure 5.14. Optical microscope images of printed lines usint paste T1 (left) and paste T2 (right) on SiriON stack.

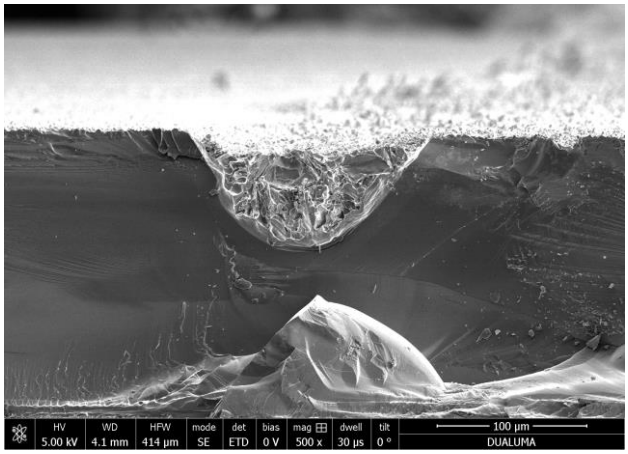

Figure 5.15. Zoom of the eutectic and p⁺-layer regions of a sample printed with paste T2 on SiriON layer on silicon. Note that the aluminum line was detached after cutting the sample for the cross-section measurement.

In summary, a variety of dielectric layers have been employed as substrates to compare the specific contact resistance for lines width of 1.2 mm, dispensed with a nozzle of 150 µm with the aluminum pastes T1 and T2. Figure 5.16 shows lower contact resistance values for paste T2 for all the dielectric layers used. With regard to

the results, the SiriON stack passivation layer outperforms the SiO_2/SiN_x stack in order to the specific contact resistance, using either two aluminum pastes. Moreover, due to wafers passivated with SiriON got better passivation quality than wafers passivated with SiO_2/SiN_x (see section 3.3), the optimum for obtaining the best results regarding to the electrical properties and passivation quality is reached by the use of paste T2 on silicon wafers passivated with SiriON stacks.

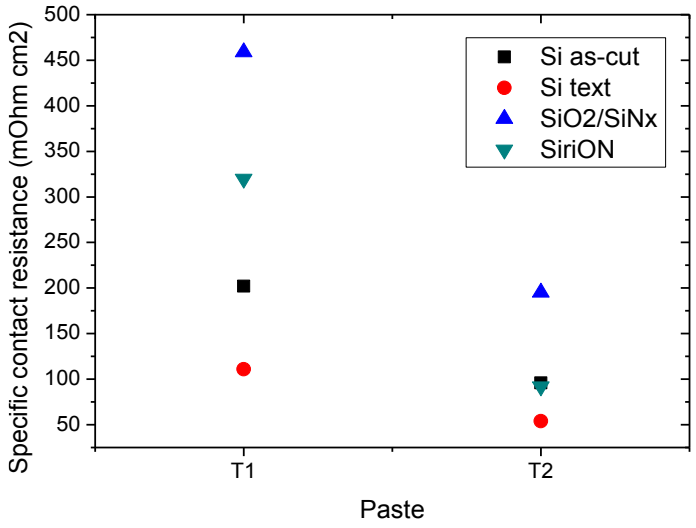

Figure 5.16. Specific contact resistance for lines of 1.2 mm width deposited by dispensing printing on differentsilicon substrates and dielectric layers by the FTC method.

Summing up, it was demonstrated that dispensing technology can be used as an alternative to screen-printing technology for the creation of local back surface field in silicon solar cells, although it is a new technique, and it must be improved to reach contact resistances as good as the obtained using screen-printing method by the moment.

6

Optimization of Al emitter for BC-BJ solar cells

This chapter contains the investigation carried out at Fraunhofer ISE related to the optimization of aluminum emitter for BC-BJ solar cells using screen-printing technology, attending to the topic of the national project "Transfer of high-efficiency solar cell structure into industrial production". Different structures were first printed with various aluminum pastes and then fired at different firing conditions. The results were compared in regard to the contact resistance, the effective surface recombination velocity and a microstructural analysis.

6.1. Back-contacted solar cells

Back-contacted silicon solar cells comprise solar cells where the electrical busbars of both polarities are located on the rear. Specifically, back-contact back-junction (BC-BJ) silicon solar cells have both the complete metallization and the complete contacted diffused regions located on the rear of the cell [107].

Due to this fact the back-contact solar cells exhibit some major advantages over the conventional solar cell with metal contact on the front side. Some of these advantages are written below:

- Due to the absence of the metallization grid in the front side, there is no shading [108,109]. This leads to an increasing in the short-circuit current (J_{sc}) of the cell. Because of that, the front surface can also be optimized for optimum light trapping and surface passivation properties. The result is that the front surface recombination can be reduced and the light trapping improved.
- Since the front side does not collect carriers and no metal needs to contact the area, a lowly phosphorus-doped front surface field is sufficient. Therefore low front surface recombination velocities can be reached.
- On the rear surface, the metal coverage can be high because it does not influence the shading. Furthermore, the metal acts as a mirror which allows the increasing of the light trapping.
- Potentially easier and fully automated co-planar interconnection of the back-contact solar cells in the module assembly process.
- Due to the uniform appearance, it is an attractive issue in the building-integrated photovoltaic sector (BIPV) [110,111].

But these solar cells have also some disadvantages, written below:

- In some cases, fatal shunting can exists due to both polarities are situated close to each other on the rear [112]. To overcome this risk, high-precision tools for structuring are needed.
- The complexity of the processing flow, due to the large steps that the process requires.
- Additional passivation steps than standard industrial methods are required, since a good passivation quality is needed especially in the front side [113].
- High-quality bulk material is essential in order to reach a high diffusion length.

Summing up, back-contact back-junction cells have a very high efficiency and cost per watt peak reduction potential, but complexity and production costs are challenging.

6.1.1. Critical parameters of the BC-BJ silicon solar cells

One of the challenges related to the back-contact back-junction solar cell structure (Figure 6.1) is the requirement of a high-quality bulk material, which means a high minority carrier lifetime in the silicon bulk (τ_{bulk}), and a low front surface recombination velocity (S_{front}). In silicon solar cells, most of the photogeneration occurs at the front side of the cell, but in the back-junction cell structure, the pn junction is located on the back cell side, so S_{front} must be low because most of the carriers are generated at the front side of the solar cell and would recombine for the case of a high value of this parameter [110]. Moreover, even if the front surface is well passivated, a risk of recombination within the bulk silicon exists.

Therefore, τ_{bulk} and S_{front} are the two most critical parameters of a BC-BJ solar cell and without fulfilling these requirements, high device efficiencies cannot be achieved.

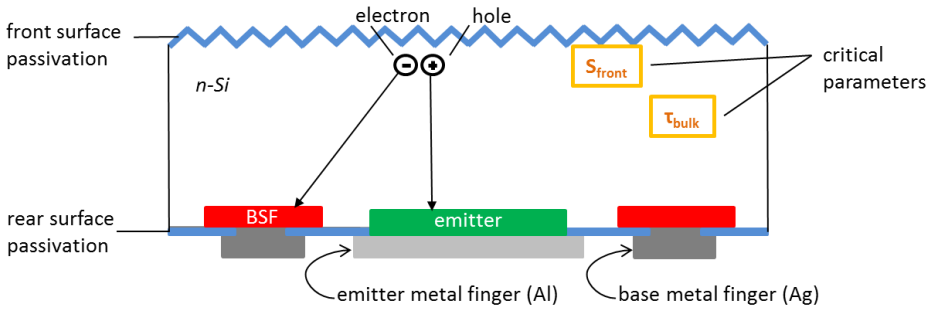

Figure 6.1. Schematic cross-section of an n-type BC-BJ solar cell with carriers needing to diffuse to the rear.

6.2. Experimental

The wafers material used in this chapter was p-type FZ silicon, with a specific resistivity of 8-12 Ωcm, 150 mm diameter and 250 µm thickness. After wet chemically cleaning, wafers were phosphorus-doped with $POCl_3$ for the front surface field (FSF). The wafers were passivated with a thin thermally grown oxide and SiN_x, opened with several structures relating to different approaches in the process for aluminum-alloyed rear emitter back-contact back-junction cells. On these structures, different aluminum pastes named A and P were used, but also were mixed with different AlB and BO content to print the dots and fingers and compare the results. There were TLM samples on each wafer (on openings/dielectic) to measure the contact resistance and isolation quality and SEM samples for microstructural study.

The aim of this experiment is to identify the optimal paste-mixture and firing conditions in dependency on the geometric structure of the Al-doping.

6.3. Wafer design

For the different processes the wafers were divided into several parts (Figure 6.2). At the top of the wafers fingers structures with different widths were printed to analyze the resistances with TLM measurements. Below these structures, different widths of fingers and points were printed to study the microstructure of the cross-sections by SEM. Four marks, one in each corner, were printed to place accurately the wafer in the screen-printing machine. 12 different structures were printed in squares of 31.25 x 31.25 mm^2 (except numbers 9 and 12) with the aim to carry out QSSPC measurements and analyze the lifetimes. The geometry of the different structures of the layout is described in Table 6.1, where f is the percentage of aluminum coverage.

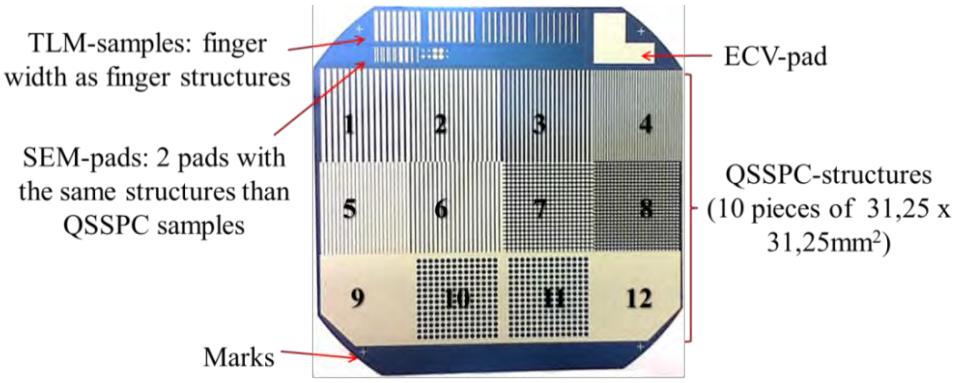

Figure 6.2. Picture of a processed wafer (125x125 mm^2) with the different screen-printed structures.

Structure	Pitch (µm)	Opening (µm)	f (%)
1	2000	1200	60
2	1600	1000	62.5
3	1500	600	40
4	900	350	39
5	1300	700	54
6	1500	500	33
7	1500	1125	16
8	1200	725	16
9*	-	-	-
10, 11	955	1630	-
12**	-	-	-

*Table 6.1. Structures geometries measured from the layout. *Full pad Al on silicon. **Full pad Al on passivated layer on silicon.*

6.4. Passivation and etching

Before the screen-printing with the different pastes, passivation layers of SiO_2/SiN_x stacks were carried out to the wafers. After that, a resin with the reverse structures than the ones depicted in Figure 6.2 was inkjet-printed to carry out the etching of the passivation layer (Figure 6.3) on the zones without that resin. After this etching, resin paste was removed and screen-printing was carried out just on the places were passivation layer was etched, right on the silicon surface.

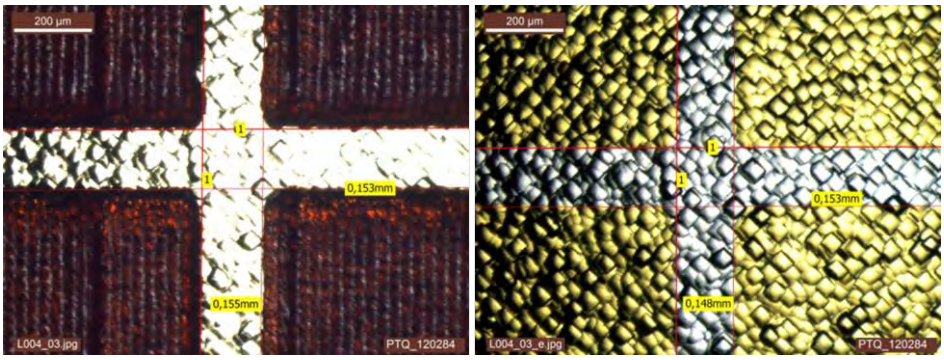

Figure 6.3. Marks before (left) and after (right) removing of the resin paste. It can be appreciated that the passivation layer on the right (yellow color) was not damaged after the etching.

6.5. Contact resistance

TLM was carried out in order to analyze the resistance of the rear contacts screen-printed with different aluminum pastes, after the firing at different conditions in a tubular fast firing oven. There were measured aluminum screen-printed lines with different widths and a common pitch of 2 mm. Table 6.2 shows the characteristics of the measured samples: aluminum paste and firing condition.

Group	Al paste	Firing condition (FC)
1	A	1
2	A	2
3	P	1
4	P + BO	2
5	P + AlB 3%	2

Table 6.2. Different groups of the wafers studied. The FC1 corresponds to 860ºC at 2600 mm/min while FC2 refers to 910 º at 4200 mm/min. BO refers to boron oxide and AlB to aluminum boride.

Figure 6.4 (a) shows the effective specific contact resistance of lines with different widths (632 µm, 1026 µm and 1231 µm), screen-printed with the same aluminum paste (A) but firing at different conditions. In general, higher lines width means lower contact resistance as it was expected. Regarding to the firing conditions, FC1, which was made at lower peak temperature and lower rate than FC2, leads to better conductivity, reaching until 60 mΩ cm^2 less of effective specific contact resistance for the same line width. Then, it could be concluded that for paste A, the peak temperature of 860ºC at a rate of 2600 mm/min was the best firing condition. On the other hand, carrying out the same firing condition to the pastes A and P, the second one outperforms the first one with regard to the effective specific contact resistance (Figure 6.4 b).

TLM measurements were also carried out for samples screen-printed with different aluminum pastes, and mixtures of aluminum paste plus an additional component, being BO for group 4 and AlB3% for group 5. Figure 6.5 shows the effective specific contact resistance for the different lines width printed on the samples and fired at the same firing condition (FC2). For this firing condition, paste P+BO got better values of effective specific contact resistance, while paste A got the worst values, which were explained in detail in Figure 6.4 (a).

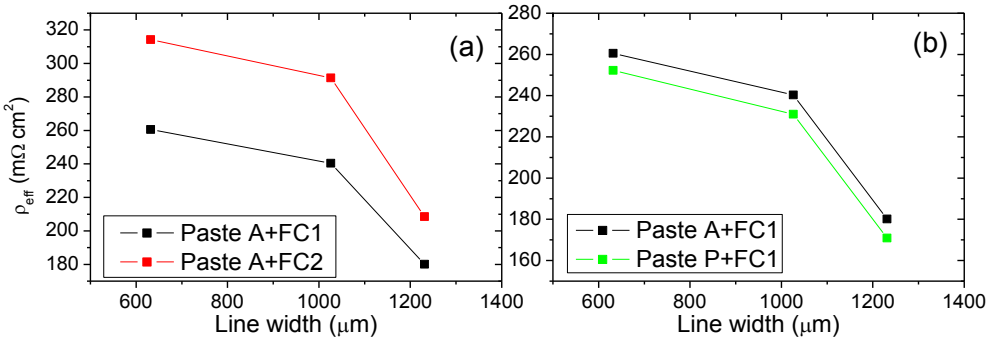

Figure 6.4. Effective specific contact resistance for samples printed with the same paste (A)+different FC (a) and different paste +same FC (b) on a passivation layer of SiO_2/SiN_x.

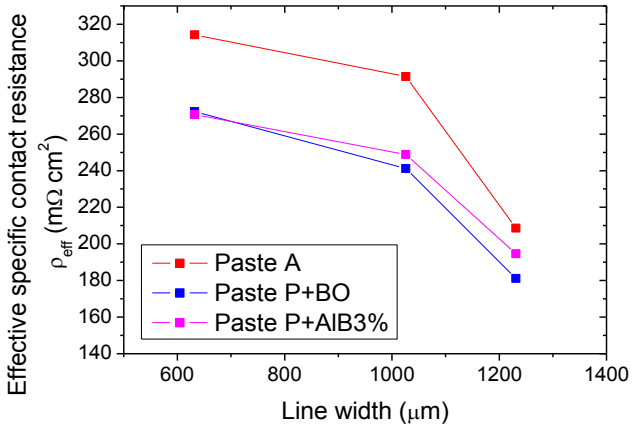

Figure 6.5. Effective specific contact resistance for samples printed with the same firing condition (FC2) and different pastes on a passivation layer of SiO_2/SiN_x.

Comparing the pastes with mixtures of other components, the effective specific contact resistance achieved was similar, but with a little improvement for samples of group 4 (aluminum paste P mixtured with boron oxide).

In conclusion, for paste A, the best firing condition was FC1 (860ºC at a rate of 2600 mm/min), reaching the minor effective specific contact resistance with line width of 1231 μm, taking a value of 180 mΩ cm^2. In addition, this firing condition FC1 was better for paste P than for paste A, achieving an effective specific contact resistance of 171 mΩ cm^2 for line width of 1231 μm. The firing condition 2 (FC2) was studied for samples screen-printed with mixtures of aluminum paste P with an additional

component: boron oxide or aluminum boride. The biggest difference in the effective specific contact resistance was noticed for lines width of 1231 µm, achieving the best value with the mixture of aluminum paste P and BO (181 mΩ cm^2). Thus, it is demonstrated the improvement of the specific contact resistance with the addition of boron compounds to the aluminum pastes.

6.6. Effective surface recombination velocity

QSSPC measurements were carried out to analyze the effective surface recombination velocity (S_{eff}) of the different lines and points geometries (Table 6.3), printed on the wafers with several aluminum pastes, and after fired at different conditions of peak temperature and belt velocity (Table 6.4).

The samples were first of all etched with an ultrasonic-assisted HCl etch, in order to remove the aluminum residuals, and annealed in forming gas atmosphere afterwards to re-activate the passivation after the ultrasonic treatment.

Structure	Geometry	Opening (µm)	Pitch (µm)	Width (µm)	%Al-coverage
1	Lines	1267.3	2000.0	1300.0	70
2		1045.6	1600.0	1100.0	70
3		651.8	1500.0	700.0	50
4		413.9	900.0	450.0	50
5		361.9	1300.0	1100.0	80
6		256.5	1500.0	1100.0	70
7	Points	-	1500.0	1175.0	50
8		-	1200.0	775.0	30

Table 6.3. Geometric characteristics of the different printed structures. The opening refers to the etched width on the structures are printed.

Firing condition	Temperature (°C)	Velocity (mm/min)
FC1	860	2600
FC2	910	4200
FC6	930	4200
FC7	960	5200

Table 6.4. Firing conditions.

When symmetrical samples are processed that allow a QSSPC measurement, τ_{eff} can be determined and related to S_{eff} as was explained in chapter 2 (Fundamentals) and eq. 6.1.

$$S = \frac{W}{2}\left[\frac{1}{\frac{1}{\tau_{eff}} - \frac{1}{\tau_b}} - \frac{W^2}{D\pi^2}\right]^{-1} \tag{6.1}$$

Then, S_{eff} was calculated for the different lines and points structures. In Figure 6.6, S_{eff} is represented against the aluminum paste for different firing conditions, with regard to screen-printed lines of several widths and distances between them.

The lowest value of S_{eff} for all the possible combinations was obtained with the structure 1 (Figure 6.6-top left), reaching a value of 12.4 cm/s for the lines printed with paste P+AlB1.5% and fired at a peak temperature of 960ºC at a velocity of 5200 mm/min (FC7). For this aluminum paste, the best firing condition regarding the effective surface recombination velocity was FC7 for all the line geometries, but with more difference against FC1 (860ºC at 2600 mm/min) regarding to wider lines. On the other hand, FC1 outperforms FC7 for paste P and its mixture with AlB3%. Then, the increasing of the AlB concentration to 3% implies both lower temperature and lower belt velocity for the firing (FC1). FC6 (930ºC at 4200 mm/min) was applied only to the structures printed with the paste P+AlB3% to compare with the other two firing conditions. For this paste, the best firing condition regarding the values of S_{eff} obtained was FC1 in the most of the cases.

With regard to the addition of the boron compound to the paste P with different percentages, both pastes P+AlB1.5% and P+AlB3% outperform paste P when firing condition FC7 is applied, reaching the best values of S_{eff} for the paste with less content of AlB.

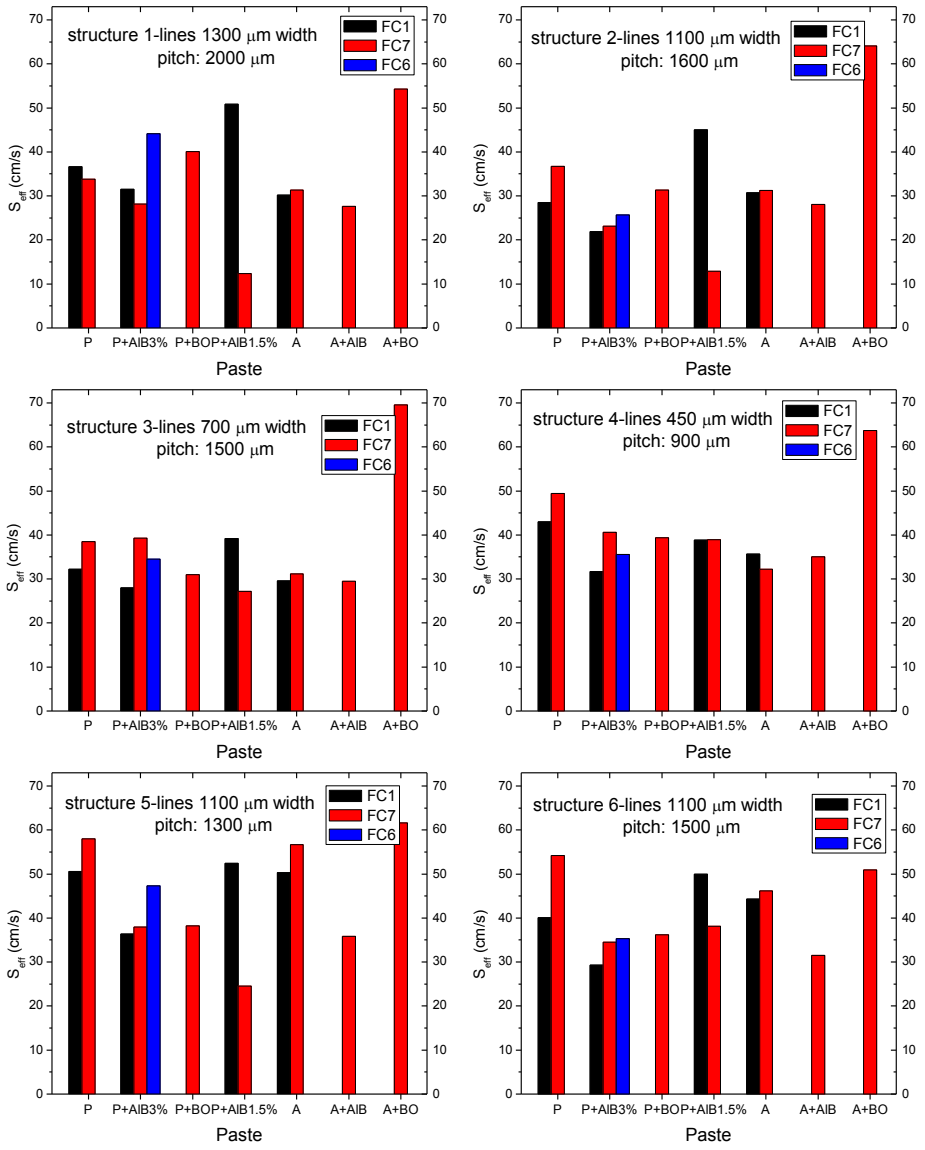

Figure 6.6. Effective surface recombination velocity S_{eff} for the different line geometries depicted in Figure 6.2 printed and fired with different aluminum pastes and firing conditions.

For 1100 µm line width, S_{eff} is represented against the pitch (distance between lines) for the FC1 and FC7 (Figure 6.7). As it is shown, S_{eff} values decrease with the pitch increasing, due to the Al coverage is lower and therefore the metallized region. Then, the lowest values of S_{eff} were found for 1600 µm pitch. For both firing conditions, paste P+AlB3% outperformed the others, although for FC7, S_{eff} values obtained from paste A+AlB were closed to the ones obtained with the paste P+AlB3%.

Comparing paste A and P without more components, it is clear that FC1 outperforms FC7, but for FC1, there were reached better S_{eff} values for lines printed with paste P than with paste A and for FC7 the effect was the opposite. In fact, it was the paste P which reveals more difference between the two firing conditions.

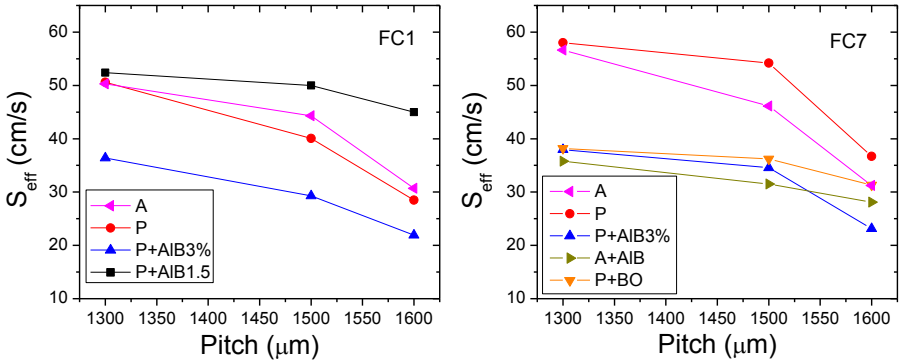

Figure 6.7. Effective surface recombination velocity for lines of 1100 µm width at different pitches under firing condition 1 (left) and 7 (right).

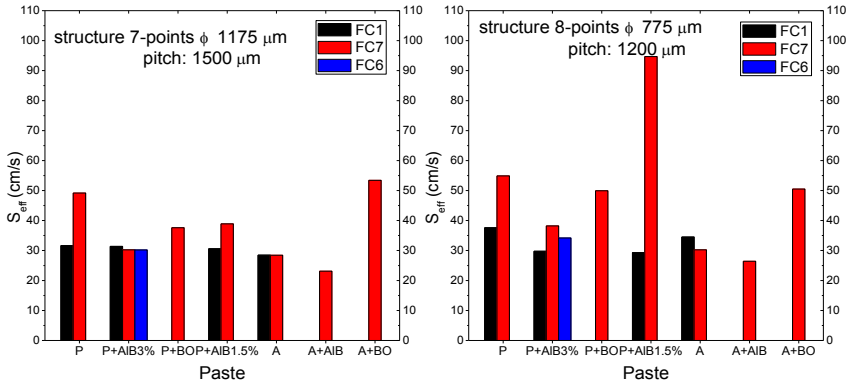

Figure 6.8. Effective surface recombination velocity S_{eff} for the different point geometries depicted in Figure 6.2 printed and fired with different aluminum pastes and firing conditions.

Considering point geometries, effective surface recombination velocity was also extracted from eq. 6.1, for the different aluminum pastes and firing conditions as depicted in Figure 6.8. Comparing FC1 with FC7 for both geometries, there is not a big difference regarding the S_{eff} values, apart from the ones extracted for the structures printed with the pastes P and P+AlB1.5%. In these cases, FC1 outperforms FC7. As the pitch is lower for structure 7 (1500 μm) than for structure 8 (1200 μm), the values obtained for S_{eff} are also lower in general. This is due to lifetimes were higher because of there was more dielectric between these points.

In summary, for lines structures, the lowest value of S_{eff} for all the possibilities was obtained with the structure 1 for the lines printed with paste P+AlB1.5% and fired at a peak temperature of 960ºC, at a belt velocity of 5200 mm/min (FC7). In the case of point structures, the lowest value of S_{eff} was found when using paste A+AlB at the same firing condition FC7. Then, it is proved the enhancement of the aluminum pastes when certain additives are added.

6.7. Photoluminescence

In luminescence imaging of silicon wafers, the surface of the sample is excited to emit luminescence, and a camera is used to acquire an image of the luminescent emission. Photoluminescence (PL) imaging avoids contacting the wafer, an advantageous practical feature for inline applications in terms of the reduced risk of mechanical damage to the wafer [114,115].

Photoluminescence is the measure of radiative recombination when the wafer is illuminated to excite excess carriers. Light generates excess carriers, then their concentration build up to values that depend on impurities, defects, and other recombination mechanisms in that region. PL intensity is proportional to the carrier concentration; so in photoluminescence images, bright areas indicate generally higher minority-carrier lifetime regions, whereas dark areas indicate in general higher defect concentration.

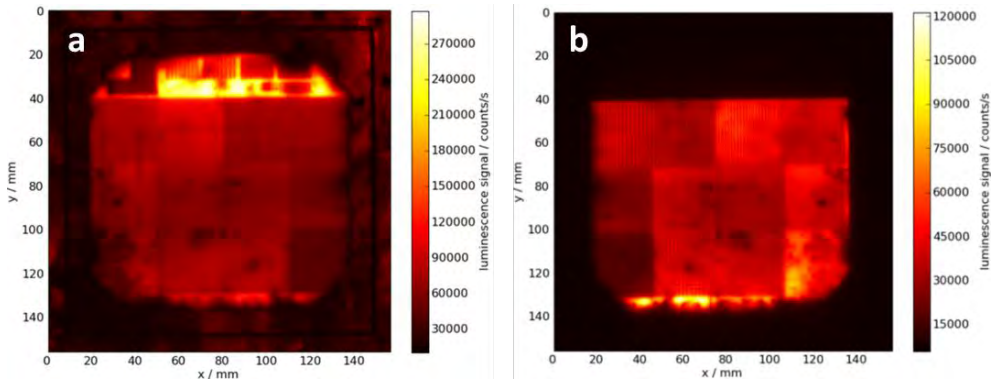

Figure 6.9. Photoluminescence image of a SiN_x passivated wafer, printed with paste P and fired under firing condition 7. (a) Rear side of the structures (b) front side of the structures. The image was taken after the removal of the aluminum residuals.

With the aim to compare qualitatively the lifetimes of the front and the rear surface of the wafers, PL measurements were carried out to the samples after passivating, printing, firing and finally HCl etching to remove the Al residuals. An example is depicted in Figure 6.9 for a wafer passivated symmetrically with SiN_x, printed with paste P and fired under firing condition 7. As it can be seen in Figure 6.9 (a) (rear side of the structures), colors are obviously much brighter than in Figure 6.9 (b) (front side of structures) due to the passivation quality is better in the front side because of there is not diffused aluminum there, in contrast to the rear side, where aluminum structures were printed. Note that the second image (b) lacks the upper part of the wafers because the picture was taken after cutting this part for the SEM analysis.

6.8. Microstructural study

Cross-sections of the upper points shown in Figure 6.2 were carried out in order to take FESEM images. The same screen-printing layout and number of layers (two) were used for all the samples, but changing the aluminum paste and carrying out two different firing conditions, FC1 and FC2 (see Table 6.4). After the firing, the diffusion of de aluminum into the silicon and vice versa took place, and therefore the Al emitter (p^+-layer) was formed under the eutectic. The groups of the wafers together with the characteristic of the metallization were described in Table 6.2.

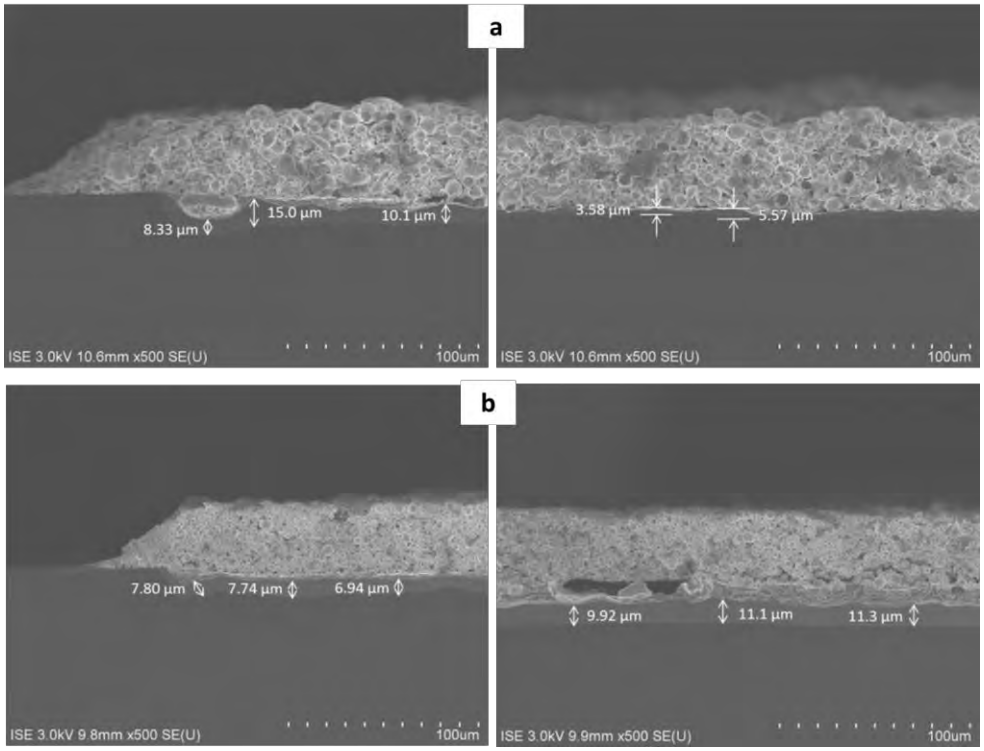

Figure 6.10. FESEM cross-sections of the edge (left) and a central place (right) of points of wafers of group 2 (a) and group 5 (b). The emitter obtained was thicker and more homogeneous around the whole point for wafers of group 5 than group 2.

The thickest and most homogeneous emitter around the whole point was obtained for wafers of groups 1 and 5. On the other hand, wafers of groups 2, 3 and 4 presented thinner emitter layer in central places of the points than in the edges. Two representative samples are depicted in Figure 6.10 to show this. This result could be related to the spread of the aluminum paste carried out by screen-printing causing the accumulation of the paste on the edges of the circles and allowing more diffusion.

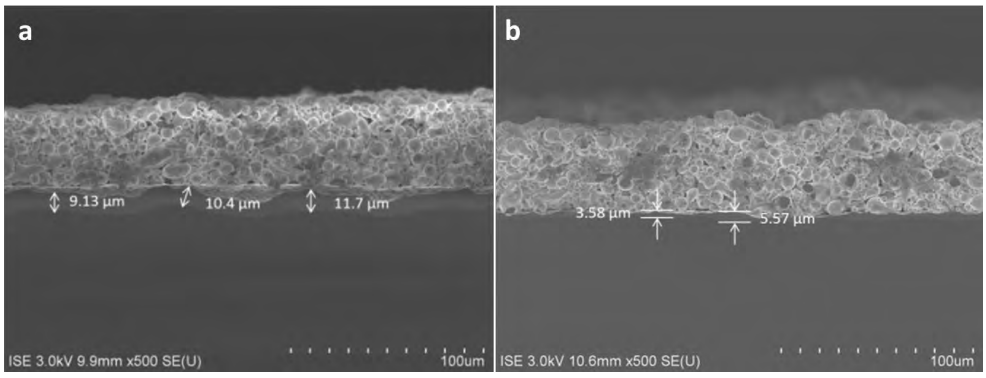

Figure 6.11. FE-SEM cross-sections of a wafer of group 1 (a) and other one of group 2 (b). The thickness and homogeneity of the emitter for group 1 was better than for group 2 (both groups with the same aluminum paste A).

Figure 6.11 shows that for the aluminum paste A, the best firing condition, regarding the thickness and homogeneity of the obtained emitter, was 860ºC at 2600 mm/min (FC1) against 910ºC at 4200 mm/min (FC2). Then, for this paste it is better low velocity of the belt furnace to guarantee a homogeneous emitter around the whole sample. This result was corroborated by the TLM measurements (Figure 6.5), which also confirmed that FC1 outperforms FC2 regarding the contact resistance.

For paste P and FC1 (Figure 6.12), the thickest thickness of Al emitter was found, taking a value of 16.5 µm. In the eutectic layer it could be appreciated little inclusions going from this layer to the aluminum residuals. That could be explained as a *back diffusion* process of the aluminum particles.

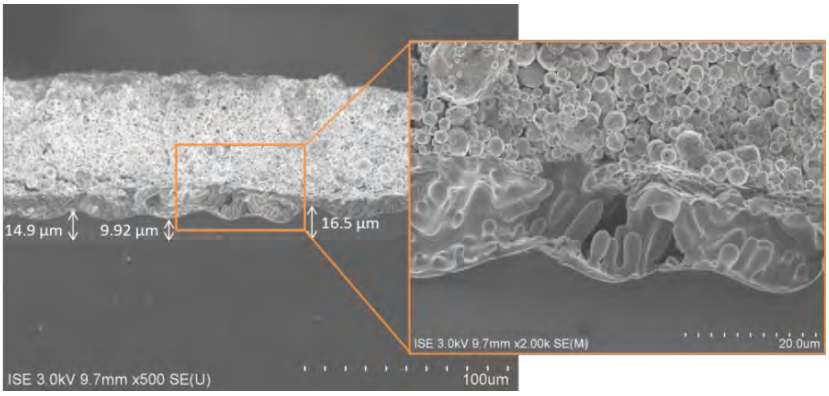

Figure 6.12. FE-SEM cross-section of a wafer of group 3 (paste P and FC1). The zoom of the picture shows the diffusion of the aluminum from the eutectic layer to the interface between this layer and the aluminum paste residuals.

7

Summary and final conclusions

Summary and final conclusions

- Thin films were prepared on silicon substrates by thermal oxidation, PECVD and magnetron sputtering, whose properties as passivation layers, antireflection layers or transparent conductive oxides for heterojunction silicon solar cells were analyzed by diverse characterization techniques.

- The best value of minority carrier lifetime of all the layers grown by PECVD was the obtained for the layer called SiriON, reaching 1477 μs after a forming gas annealing.

- The thin layers of SiN_x grown by magnetron sputtering had a maximum transmittance at 550 nm of 91.6% and a refraction index of 1.91, obtained by the ellipsometry. A high content in oxygen implies a lower refraction index and also lower transmittance.

- It was demonstrated the transmittance of the thin Al:ZnO layers grown by magnetron sputtering, giving more value of bandgap for the most aluminum-doped samples, reaching 3.57 eV. These samples were also the most conductive, so it could be concluded that they could work as TCOs in heterojunction silicon solar cells.

- Two different aluminum pastes for local contact formation in rear passivated silicon solar cells using the fire through contact (FTC) approach were investigated. Besides the formation of the rear surface passivation layer and screen-printing of the fire-through structures, no additional technology was required compared to the standard Al-BSF process. The contact density area and thus the specific contact conductivity are higher for the newly developed paste A (see chapter 4) than for formerly investigated pastes. Furthermore, paste A delivered better contact conductivity than paste B for the same recombination velocity and firing condition. This could be attributed to the formation of a homogeneous local p^+-layer in case of paste A by microstructural analysis.

- The using of a manual screen printer was optimized for the obtaining of a local back surface field on silicon substrates and passivation layers grown on silicon. Different layouts were designed with the aim to obtain aluminum structures with line widths between 0.35 and 1.5 mm using three aluminum pastes, B, T1 and T2 (see chapter 4). The best values of specific contact resistance were obtained for line width of 1.2 mm for the most of the pastes printed on silicon. Thus, this line width was used to create the LBSF on the

passivated silicon substrates. The optimum values were obtained for the paste T2 printed on the substrates passivated with SiriON.

- The feasibility of the dispensing technology was demonstrated for the formation of a local back surface field using the same aluminum pastes than in manual screen printing. With silicon as substrate, the best result of specific contact resistance was obtained for line width of 1.2 mm dispensed with paste T2 (see chapter 5). The FTC approach was used by the dispensing of the pastes T1 and T2 on the passivation layers on silicon SiriON and SiO_2/SiN_x. The best values were obtained for the SiriON passivation layer, although it was demonstrated the formation of the LBSF with the two aluminum pastes on the two passivation layers by the resistance measurements and the microstructural analysis.

- The aluminum emitter was optimized for BC-BJ solar cells by the use of diverse aluminum pastes and mixtures of these pastes with boron compounds. An optimum firing is stablished for a low recombination velocity, and thus in an improvement of the surface passivation. It was demonstrated an improvement of the specific contact resistance using the aluminum pastes mixed with boron compounds.

List of publications

Refereed papers presented at international conferences

- E. Navarrete, A. Kimmerle, B. Thaidigsmann, R. Woehl, J.R. Ramos-Barrado, D. Biro. *Evaluation of fire-through aluminum pastes for local contact formation in silicon solar cells*. Proceedings of the 28th European Photovoltaic Solar Energy Conference and Exhibition, Paris, France, 1839-1841 (2013).

- C. Vázquez, L J Caballero, R. Sierras, J. Alonso, E. Navarrete, J.R. Ramos-Barrado, R. Gutiérrez. *Low cost industrial PERC solar cell: cost viability versus solar cell based on current screen printing BSF-Al*. Proceedings of the 28th European Photovoltaic Solar Energy Conference and Exhibition, Paris, France, 1770-1773 (2013).

- Elena Navarrete Astorga, Efraín Ochoa Martínez, José. R. Ramos Barrado. *Low cost spray-coating boron diffusion on n-type silicon*. 9th Spanish Conference on Electron Devices, Valladolid, Spain, 325-327 (2013).

- Elena Navarrete Astorga, Miguel Marín Enríquez, Jorge Rodríguez Moreno, José Ramón Ramos Barrado. *Feasibility of dispensing technology to create local aluminum contacts on silicon solar cells*. 10th Spanish Conference on Electron Devices, Aranjuez, Spain, p-p (2015).

Other refereed papers presented at international journals

- F. Martín, E. Navarrete, J. Morales, C. Roldán, J.R. Ramos-Barrado, L. Sánchez. *High-Energy, Efficient and Transparent Electrode for Lithium Batteries*. Journal of Materials Chemistry, 20 (14) (2010) 2847-2852.

- Jorge Rodríguez-Moreno, Elena Navarrete-Astorga, Francisco Martín, Ricardo Schrebler, José R. Ramos-Barrado, Enrique A. Dalchiele. *Semitransparent ZnO/poly(3,4-ethylenedioxythiophene) based hybrid inorganic/ organic heterojunction thin film diodes prepared by combined radio-frequency magnetron-sputtering and electrodeposition technique*. Thin Solid Films 525 (2012) 88-92.

- Jorge Rodríguez, Elena Navarrete, Enrique A. Dalchiele, Luis Sánchez, José Ramón Ramos-Barrado, Francisco Martín. *Polyvinylpyrrolidone-$LiClO_4$ solid polymer electrolyte and its application in transparent thin film supercapacitors*. Journal of Power Sources 237 (2013) 270-276.

- Jorge Rodríguez-Moreno, Elena Navarrete-Astorga, Rocío Romero, Francisco Martín, Ricardo Schrebler, José Ramón Ramos-Barrado, Enrique A. Dalchiele. *Electrochemically grown vertically aligned ZnO nanorod array/p^+-Si <100> heterojunction contact diodes*. Thin Solid Films 548 (2013) 235-240.

- Jorge Rodríguez-Moreno, Elena Navarrete-Astorga, Enrique A. Dalchiele, Ricardo Schrebler, José R. Ramos-Barrado, Francisco Martín. *Vertically aligned ZnO@CuS@PEDOT core@shell nanorod arrays decorated with MnO_2 nanoparticles for a high-performance and semi-transparent supercapacitor electrode*. Chemical Communications, 50 (2014) 5652.

APPENDIX

Appendix A. Silicon substrates cleaning

Appendix B. Layouts for manual screen-printing

Appendix C. Characterization techniques

Appendix D. Resumen en español

Appendix E. Conclusiones

Appendix A. Silicon substrates cleaning

The cleaning method for the silicon wafers before processing was carried out following these five steps:

1. Boiled in Isopropanol 10 min.
2. Dip in NH_4OH 27%:H_20_2 30% :H_2O (1:1:5)[A] for 10 min@80ºC (RCA-1); followed by ultrasonic DI water rinse.
3. Dip HF:H_2O (1:20)[C] 30s; followed by DI water rinsed.
4. Dip in HCl 27%:H_20_2 30% :H_2O (1:1:6)[B] for 10 min@80ºC (RCA-2); followed by ultrasonic DI water rinse
5. Dip HF:H_2O (1:20)[C] 30s; followed by DI water rinsed.

Being the three solutions A, B and C prepared as following:

A. 35 ml RCA-1: 25ml H_2O + 5ml H_2O_2 30% + 5ml NH_3 27%
B. 32 ml RCA-2: 24ml H_2O + 4ml H_2O_2 al 30% + 4ml HCl al 37%
C. 50 ml HF 5%: 5ml HF 48% + 45ml H_2O

Appendix B. Layouts for manual screen-printing

Line width: 0.35 cm

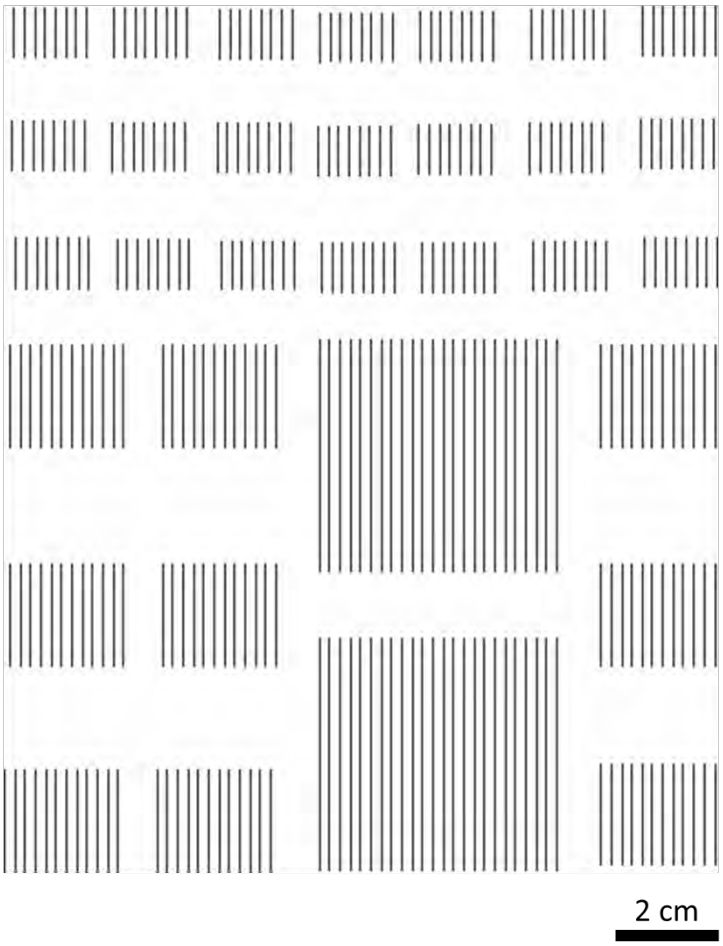

Line width: 0.6 cm

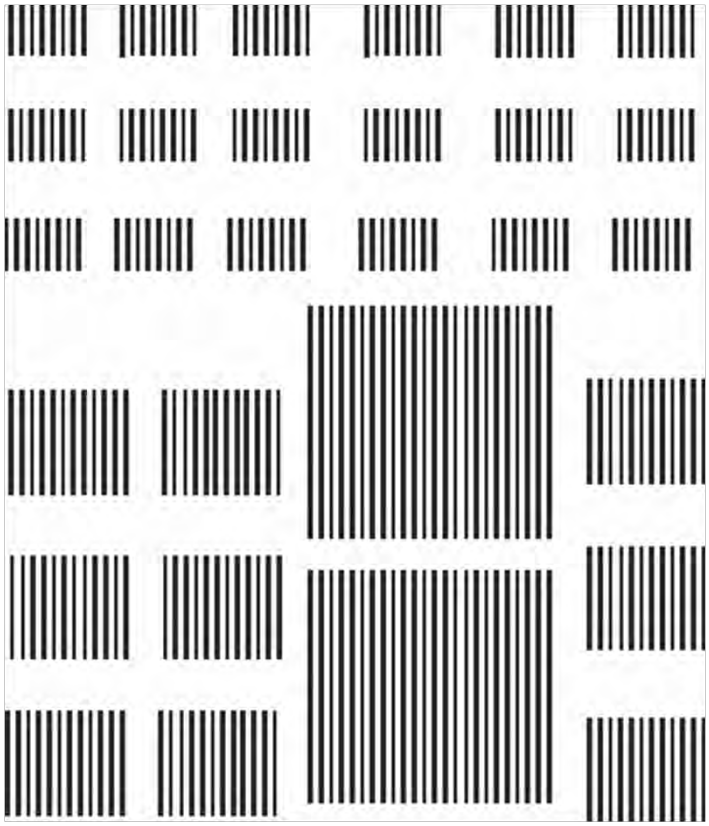

2 cm

Line width: 1 cm

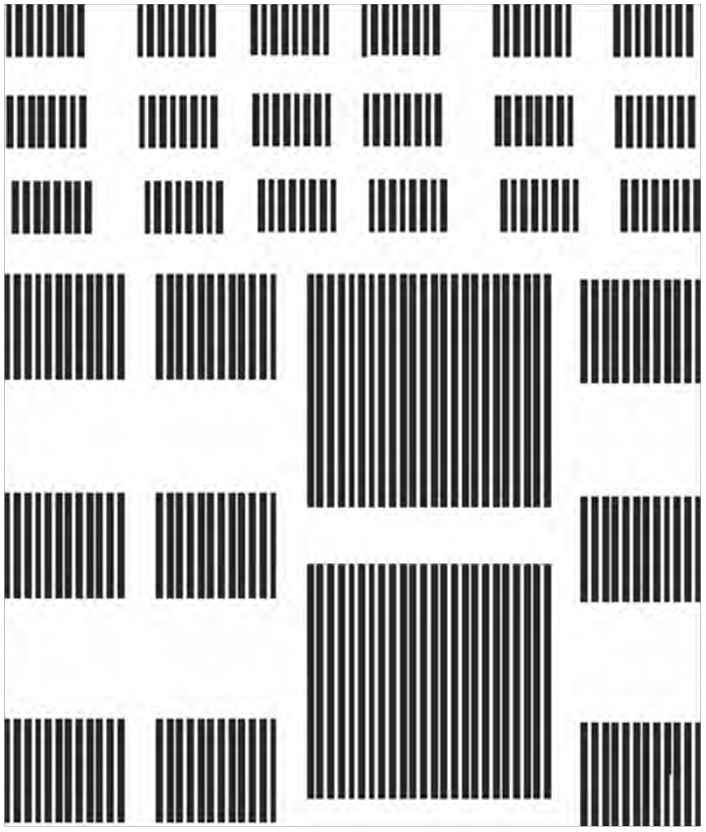

2 cm

Line width: 1.2 cm

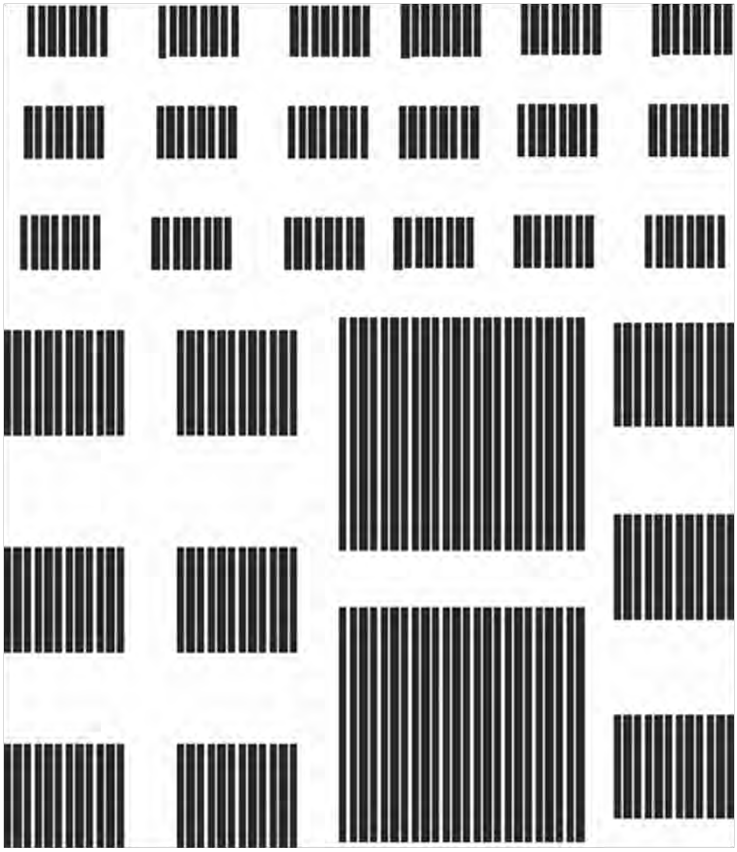

2 cm

Line width: 1.5 cm

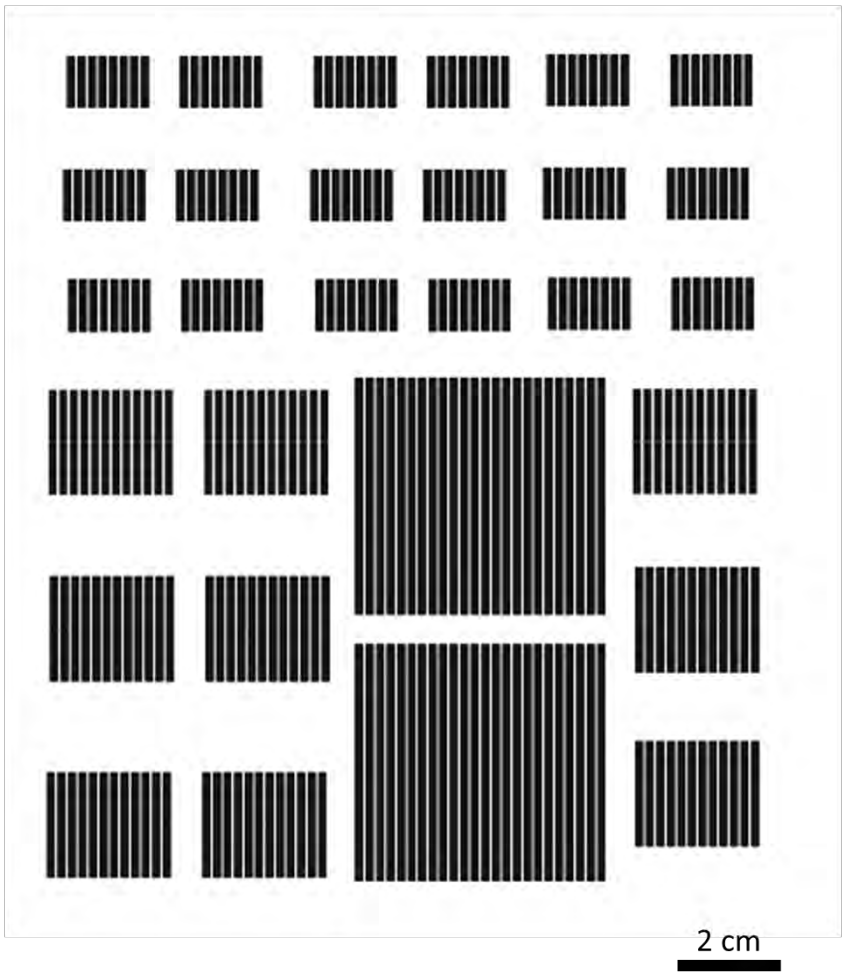

Appendix C. Characterization techniques

1. X-ray diffraction (XRD)

X-ray diffraction is a form of electromagnetic radiation of high energy and low wavelength, in the order of the interatomic space solids. When an X-ray beam impacts in a solid sample, part of this beam is dispersed in all directions due to the electrons associated to the atoms or ions found in the way. But the rest of the beam may result in the phenomenon of X-ray diffraction which occurs if an ordered disposure of atoms exists and if the Bragg conditions relating to the X-ray wavelength and the interatomic distance with the incident angle of the diffracted beam are reached. In the case the Bragg law is not fulfilled, the interference is not constructive and the field of the diffracted beam has a very low intensity.

The equipment used in this thesis was the X'Pert Pro from PANalytical with X'Celerator detector, which enables a very high data acquisition rate. The system operates in two different configurations. The first one is the very high resolution mode, with the primary monochromator of Ge (111), which is ideal to study crystalline compounds and structural and textural analysis. The second configuration is the parallel beam mode, where the primary monochromator of Ge (111) is replaced by a primary hybrid monochromator which generates a parallel beam that is ideal or studying samples at tilted angles (thin layers) and samples with irregular surfaces. Depth profile diffractograms can be performed depending on the angle and the absorption coefficient of the sample.

For the present work, X-ray diffraction was used to study the crystallinity of the thin layers prepared by magnetron sputtering, with the aim to identify the crystal phases by comparison of the obtained diffractogram with the PDF (Powder Database File) database.

2. X-ray photoelectron spectroscopy (XPS)

X-ray photoelectron spectroscopy is nowadays the superficial analytical technique most used. Studied by Siegbahn et al. was named as ESCA (Electron Spectroscopy for Chemical Analysis) to emphasize the chemical (rather than merely elemental) information that the technique provides, but currently that name is considered too general due to the amount of the surface electron spectroscopies that are used.

XPS is a surface chemical analysis technique that can be used to analyze the surface chemistry of a material giving information of the elemental composition at the parts, empirical formula, chemical state and electronic state of the elements that exist within that material.

The principle of this technique consists in irradiating the surface of the sample with soft X ray photons. When a photon with energy hν interacts with an electron in a level with a binding energy E_B, the photon energy is transferred completely to the electron, resulting in the emission of one photoelectron with a kinetic energy

$$E_{Kin} = h\nu - E_B - e\varphi \qquad (h\nu > EB)$$

The emitted electron can come from an inner level or an occupied part of the valence band, but in this technique the most attention is focused in the electron of the inner levels. As there are not two elements sharing the same band gap, measuring the kinetic energies provides an elemental analysis. Furthermore, any change in E_B reflected in the E_{Kin}, which means that changes in the chemical environment of an atom can be studied with changes in the photoelectron energies, providing chemical information. XPS technique can analyze all the elements of the periodic Table with the exception of the hydrogen and helium.

Although the XPS is related mainly to photoelectrons and their kinetic energies, the leaving of electrons through other processes also occurs. An emitted photoelectron leaves an inner gap in the atom. The hole is created in the K layer, giving place to a photoelectron whose kinetic energy must be ($h\nu$-E_{Kin}), and this gap is occupied by an electronic transition from L_2 layer. The E_{Kin}-E_{L2} energy associated to the transition can dissipate in an X-ray photon or losing an electron of a third layer (layer L_3 in the example).

The other possibility is called Auger process because of its discoverer. The emitted electron is called Auger electron and its energy is the following:

$$E_{KinL2L3} = E_{Kin} - E_{L2} - E^*_{L3}$$

where E^*_{L3} is referred to the band gap of the electron in the L_3 layer in presence of a hole in L_2 layer. The emission of X-ray photons (X-ray fluorescence) and the emission of an Auger electron are processes that compete with each other, but Auger process is favored due to the superficiality of the inner levels involved in the XPS and Auger processes. Therefore, in all the X-ray photoelectronic spectra photoemissions and Auger emissions are produced.

In this work, the analysis was carried out by a system called ESCA 5701, from Physical Electronics (PHI), consisting of a standard dual X-ray source with Mg K_α (1253.6 eV)

and Al K_α (1486.6 eV) anodes. XPS was used for the thin films obtained by magnetron sputtering, described in chapter 3.

3. Field Effect Scanning Electronic Microscopy (FESEM)

FESEM images were taken by a Helios Nanolab 650 dual microscope from FEI. This SEM/FIB combines the most advanced scanning electron microscope (SEM) and focused ion beam (FIB) technologies with innovative gas chemistries, detectors and manipulators.

The equipment is composed by two columns. The FESEM column (Elstar XHR immersion lens) has a resolution of 0.8nm at 15 kV and 0.9 nm at 1 kV and it has an integrated monochromator (UC) and beam deceleration. It delivers sub-nanometer resolution across a 1-30 kV range. The FIB column (Tomahawk ion column) is vacuum-pumped at the lowest level, allowing a well-defined beam profile to hit the sample surface. The equipment has 5 different gas injectors for nanodeposition and local etching of certain materials. Furthermore, the equipment has electrical microprobes and nanoindenters, EDX, EBSD+CBD and STEM detectors.

In this work this equipment was used to take pictures of the surface of the samples to check the homogeneity and the cross sections of some other samples to notice the diffused aluminum forming the back surface field (Chapters 4, 5 and 6). The FIB column in combination with the Omniprobe nanomanipulator was useful to the lamellae preparation of ZnO samples before TEM analysis (Chapter 3). To analyze in a qualitative way the element composition the EDX detector was used.

4. Ultraviolet-Visible spectrometry

Ultraviolet–visible spectroscopy (UV-Vis) refers to absorption spectroscopy or reflectance spectroscopy in the ultraviolet-visible spectral region. This means it uses light in the visible and adjacent (near-UV and near-infrared (NIR)) ranges. When the light spot interacts with the material, certain wavelengths are absorbed.

The spectrophotometer used in this work was a Varian Cary 5000 model composed by a light source, a monochromator which splits the light into a continuous wavelength spectrum, and the detectors which register the intensity of transmitted or reflected light depending on the measuring mode.

In this thesis, transmittance and reflectance measurements were carried out in order to gain knowledge about the optical properties of the different samples prepared by magnetron sputtering (Chapter 3). In the case of Al:ZnO samples, it was mainly used to determine the variation of the band gap with the dopant amount.

5. Secondary Neutral Mass Spectroscopy (SNMS)

SNMS is one of the most efficient methods to determine the depth distribution of atomic compositions. In SNMS, the sample surface is bombarded by an ion beam and the sputtered neutral particles, atoms and clusters are detected by a mass spectrometer after some post-ionization, which can be performed by an electron beam, electron gas or laser beam. In SNMS the processes of emission and ionization of sputtered particles are strictly separated, which is the main difference with SIMS.

The equipment used in this work is capable to carry out the depth profiles analysis of inorganic and organic thin films with a high depth resolution of 1 nm and a high sensitivity with detection limit down to 1 ppm. The depth profile analysis carried out in this work were performed using a SNMS, INA-x, SPECS Gmbh, in high frequency mode (HFM) by using Ar+ ions with an energy for sputtering of 350 eV. The erosion area was confined to a circle of 2 mm of diameter by means of a Ta mask. The depth scale was fixed taking into account profilometer thickness determination.

In this work, SNMS has been used to analyze the depth profile of the thin films deposited on silicon by magnetron sputtering, described in Chapter 3.

6. Ellipsometry

Ellipsometry is a non-invasive optical technique devoted to the analysis of surfaces. It is based on the measurement of the variation of the polarization state of the light after reflection on a plane surface. For this, the collimated light beam impacts on the sample and then is registered on the detector, which register the angles Ψ and Δ which describe the polarization state of light. Afterwards, it is necessary to apply numerical methods and adjusting software to fit the results to the theoretical values of the unknown film properties.

The ellipsometer used in this work was the Sopra GES-5E, a spectroscopic ellipsometer with high resolution and fast acquisition variable angle capabilities which also allows performing spectroscopic scatterometry, photometry, reflectometry, polarimetry and porosimetry of thin films and bulk materials.

In this thesis, ellipsometry has been used to obtain the thickness of SiO_2, SiriON, SiN_x and Al_2O_3 layers.

7. High Resolution Transmission Electron Microscopy (HRTEM)

Transmission electron microscopy (TEM) is a microscopy technique in which a beam of electrons is transmitted through an ultra-thin sample, interacting with the sample as it passes through. When the accelerated narrow electrons beam impact with the sample, signals related to the atomic structure of the researched object are generated. These signals are selected in order to generate different type of images and to obtain analytical data. Transmitted electrons are used to create transmission images of high resolution, giving knowledge of the inner structure of the samples, size and particle distribution, crystallographic network, interphases and defects of the atomic network… Generated x-rays are used to study the chemical composition of the sample. A detailed crystallographic study of the material can be carried out through the electrons diffraction.

The equipment used in this work was a TEM model JEOL 3000F with FEG (field emission gun), 300 kV of acceleration voltage and a structural resolution of 0.17 nm.

In this work, TEM images were displayed with the aim to analyze the thin films of ZnO and aluminum doped ZnO (Chapter 3). Previously, the samples were cut and polished to prepare cross-sections by a FIB tool (see 3. FESEM).

8. Raman spectroscopy

Raman spectroscopy is a spectroscopic technique which provides information about vibrational, rotational and other low-frequency modes that can be used for sample identification and quantitation. The technique involves shining a monochromatic light source (i.e. laser) on a sample and detecting the scattered light.

In Raman spectroscopy applications, intense laser beams are used to create Raman scattered light from a sample under test. The Raman *finger print* is measured by a spectrometer. Optical filters are critical components in Raman spectroscopy systems to prevent all undesired light from reaching the spectrometer.

In this work, thicker films of ZnO and Al:ZnO on amorphous silica were specially grown for the Raman measurements because silicon substrates mask the spectrum from the films. Raman spectra were obtained for the films deposited on silica substrates, in back scattering geometry with a Renishaw Ramascope 2000 spectrometer equipped with an Olympus microscope (100x objective) and an ion argon laser (emission wavelength 514.5 nm). Laser power on the sample was about 3mW. Spectra were collected at different points on the films.

Appendix D. Resumen en español

CAPÍTULO 1. INTRODUCCIÓN

Atendiendo a los diferentes tipos de energía renovable, la fotovoltaica tiene la enorme ventaja de que ofrece una abundante capacidad sobre la Tierra debido a la luz solar, la cual está disponible en todas partes en diferente alcance y puede ser convertida directamente en electricidad. Desde 2010, el mundo ha añadido más capacidad solar fotovoltaica que en las cuatro décadas anteriores, siendo la capacidad global total de 150 GW a principios de 2014. En la actualidad, sobre el 90% de la producción de energía fotovoltaica es generada por tecnología basada en las obleas de silicio cristalino. Pero el coste de producción de esta energía es aún demasiado alto. Este coste podría disminuir simplificando los pasos del proceso, pero también usando menos material base.

La disminución de material base podría conseguirse mediante la utilización de obleas de silicio más finas como sustratos usando técnicas especiales que eviten la rotura de las obleas. En este trabajo, este punto se ha llevado a cabo a través del uso de una tecnología de impresión de no contacto llamada '*drop on demand*' o dispensado en general. Además, se ha implementado el método FTC (*fire through contact*) con el mismo objetivo de reducir costes. Mediante la aplicación de este método, el paso de crear una máscara sobre la capa pasivante para la posterior eliminación de manera local y la impresión del metal sobre los huecos creados es suprimido, usando pastas de aluminio especiales capaces de atravesar dicha capa pasivante y formar el eutéctico Al-Si para obtener el campo local superficial trasero (LBSF). Asimismo, se han utilizado pastas de aluminio en lugar de plata con el mismo objetivo de la reducción de los costes.

MOTIVACIÓN Y OBJETIVO

El principal reto de esta tesis ha sido la obtención de un campo local superficial trasero mediante diferentes técnicas usando varios tipos de capas pasivantes con el objetivo de mejorar la eficiencia de la célula final. Un profundo estudio de estas capas depositadas sobre silicio se ha llevado a cabo con la finalidad de analizar la capacidad de las mismas para actuar como recubrimientos anti-reflejantes como es el caso de las capas de SiN_x, o como óxidos conductores transparentes como el ZnO dopado con aluminio para células de silicio de heterounión. Además, se han utilizado diferentes pastas para la obtención del emisor de aluminio para células solares de contacto-trasero unión-trasera (BC-BJ). La calidad de las capas pasivantes junto con las resistencias específicas de contacto obtenidas son un signo de mejora para la celda

solar final. En definitiva, se ha utilizado tecnología de bajo coste, como el método FTC mencionado anteriormente, para conseguir una industria fotovoltaica competitiva en el mercado contribuyendo así en la dirección de una producción de energía sostenible.

ESQUEMA DE LA TESIS

Esta tesis se divide en seis capítulos. En la introducción se expone el panorama actual de la energía solar fotovoltaica, con especial referencia a España, así como la motivación y el objetivo de este trabajo. En los capítulos siguientes se describen los métodos experimentales junto con la discusión de los resultados obtenidos y las conclusiones.

En el **capítulo 2** se han descrito los fundamentos de este trabajo. En primer lugar, se presentan las ecuaciones básicas del semiconductor junto con la curva intensidad-voltaje para las celdas solares de silicio. Los mecanismos de pérdida son explicados teniendo en cuenta el proceso de texturizado de la superficie. También se describe la vida media del portador minoritario y la técnica usada para su medida. Se detalla el método utilizado para la obtención de las resistencias específicas de contacto. A continuación se presenta la teoría básica de la aleación de aluminio sobre el silicio, la cual juega un papel importante en este trabajo. Por último, son descritas las técnicas de impresión de pastas y los métodos de deposición de capas finas utilizados en esta tesis.

En el **capítulo 3** se describen las capas dieléctricas creadas mediante diferentes técnicas de preparación de capas delgadas. Algunas de ellas son estudiadas como capas pasivantes para células solares de silicio, mientras que otras son analizadas y comparadas con el objetivo de actuar como recubrimientos anti-reflejantes u óxidos conductores transparentes para aplicaciones en celdas solares de silicio. La calidad de la pasivación se ha estudiado mediante el método QSSPC (*quasi-steady state photoconductance*), mientras que la estructura fue analizada mediante el uso de diversas técnicas de caracterización como XPS (*X-ray photoelectron spectroscopy*) y DRX (difracción de rayos X) entre otras.

En el **capítulo 4**, estructuras de aluminio son serigrafiadas sobre silicio monocristalino de tipo p con el objetivo de crear un campo local superficial trasero. Las propiedades eléctricas de los contactos locales son estudiadas junto con un análisis de la microestructura formada. En primer lugar, se muestran los resultados del proceso de serigrafía automático utilizado en los laboratorios del instituto de energía solar Fraunhofer ISE, en Friburgo (Alemania) durante la estancia de la autora de la tesis en dicho lugar. El método FTC es utilizado con diferentes capas pasivantes. Finalmente, en este capítulo se describen los resultados obtenidos del proceso de serigrafía manual, usando también el método FTC y diferentes capas pasivantes.

En el **capítulo 5**, un robot dispensador es utilizado para crear estructuras de aluminio sobre obleas de silicio monocristalino de tipo p con el mismo objetivo perseguido en el capítulo anterior. El espesor del campo local superficial trasero es medido y la resistencia específica de contacto es comparada para diferentes pastas de aluminio. Para completar el estudio, se ha llevado a cabo un análisis de la microestructura creada.

El **capítulo 6** contiene los resultados de una investigación llevada a cabo en el Fraunhofer ISE relacionada con la optimización del emisor de aluminio para celdas solares tipo contacto-trasero unión-trasera. Se han utilizado varias pastas de aluminio y diferentes condiciones de quemado (*firing*) para comparar los resultados obtenidos mediante la medida de la resistencia de contacto, la velocidad de recombinación efectiva superficial y el análisis de la microestructura creada. Las técnicas empleadas fueron las mismas que en el resto de la tesis.

CAPÍTULO 2. FUNDAMENTOS

En primer lugar, se presentan las ecuaciones básicas del semiconductor junto con la curva intensidad-voltaje para las celdas solares de silicio. Los mecanismos de pérdida son detallados teniendo en cuenta el proceso de texturizado de la superficie. También se describe la vida media del portador minoritario y la técnica usada para su medida. Se detalla el método utilizado para la obtención de las resistencias específicas de contacto. A continuación se presenta la teoría básica de la aleación de aluminio sobre el silicio, la cual juega un papel importante en esta tesis. Por último, son descritas las técnicas de impresión de pastas y los métodos de deposición de capas finas utilizados en este trabajo.

CAPÍTULO 3. CAPAS DELGADAS SOBRE SILICIO

En este capítulo se han depositado capas finas sobre silicio monocristalino tipo p con la finalidad de darle propiedades específicas para su aplicación en celdas solares de silicio. Las capas dieléctricas pasivantes en la parte posterior de las celdas solares es tan importante como en la parte frontal para disminuir las pérdidas por recombinación. Estas capas deben tener el espesor suficiente para permitir una alta vida media de portadores y, por tanto, una baja densidad de saturación de corriente. Requieren baja velocidad de recombinación en la superficie trasera y trabajan como espejos ópticos, produciendo alta reflectancia interna.

En bibliografía, se han depositado films de alúmina mediante diversas técnicas como PECVD (*plasma-enhanced chemical vapor deposition*), ALD (*atomic layer deposition*) o CVD (*chemical vapor deposition*). Por otro lado, la técnica más utilizada para el crecimiento de capas de SiN_x es PECVD. En cuanto a las capas de Al_2O_3/SiN_x, normalmente son preparadas mediante PECVD y ALD en la industria fotovoltaica.

Pero, recientemente, el sputtering está siendo una técnica prometedora frente al PECVD, ofreciendo una serie de ventajas como la eliminación de gases tóxicos, la capacidad de operar a bajas temperaturas, el bajo coste, la fácil regulación de la velocidad de deposición y, en definitiva, ser un sistema más simple de deposición. Además, el sputtering es también competitivo frente al ALD, debido a que este último ofrece velocidades de deposición muy bajas. La técnica de sputtering permite modular fácilmente la temperatura de deposición, la presión de trabajo y el flujo de gas para obtener las capas finas deseadas. A su vez, la posibilidad de operación a bajas temperaturas permite la utilización de diversos sustratos y ofrece la posibilidad de usar las capas de Al_2O_3/SiN_x como films transparentes en dispositivos flexibles. Por otro lado, las capas de SiN_x son depositadas normalmente por PECVD en la industria fotovoltaica con la función de recubrimientos anti-reflejantes, pero este método tiene un alto coste químico a pesar de la uniformidad de la capa obtenida, la alta precisión y la también alta velocidad de deposición.

Este capítulo se divide en dos partes bien diferenciadas. Una es la preparación de capas finas mediante el método PECVD y su caracterización como capas pasivantes, y la otra es la preparación de capas finas mediante el método de magnetrón sputtering y su análisis como capas con diferentes propiedades para las celdas solares de silicio.

RESULTADOS Y DISCUSIÓN

Capas obtenidas mediante PECVD

En relación a las capas de SiN_x obtenidas mediante PECVD y las crecidas térmicamente de SiO_2, las primeras necesitan mucho más espesor para alcanzar vidas medias similares (ver *Figure 3.3*). Por otro lado, los mejores resultados de pasivación son obtenidos para las capas de SiriON (*silicon rich oxynitride*), que al igual que los de las demás capas, fueron obtenidos tras las medidas de QSSPC (ver *Table 3.1*) sin añadir ningún paso térmico.

Para la mejor opción de pasivación, que fue la obtenida con las capas de SiriON, se utilizaron obleas de silicio FZ (*float zone*) con el objetivo de obtener aún mejores resultados. Tras el depósito de la capa, la pasivación superficial fue activada mediante un tratamiento a alta temperatura (880ºC) y a una velocidad de 5200 mm/min. Tras esto, el resultado de vida media fue mejorado, pasando de 127 a 1238 µs. Por último, la muestra fue introducida en un horno para llevar a cabo el recocido en atmósfera de hidrógeno y nitrógeno (*forming gas*). Con esto, la vida media se mejoró aún más llegando a un valor de 1477 µs.

Imágenes de microscopio óptico de las capas obtenidas se muestran en la *Figure 3.4*, donde puede observarse la homogeneidad de dichas capas. Las obleas presentan un color azul cuando el oxígeno está presente en la composición de la capa pasivante,

como es el caso de SiO_2/SiN_x y SiriON, mientras que las de SiN_x muestran un color amarillo.

Capas obtenidas mediante magnetrón sputtering

SiN_x

Las capas de nitruro de silicio fueron preparadas con un blanco cerámico del mismo material, al que se le aplicó una potencia de 150 W y se trabajó a una presión de $1.2 \cdot 10^{-4}$ mbar durante 30 y 60 minutos a temperatura ambiente. Se ha estudiado la estructura y composición de la capa mediante XPS, EDX y SNMS, concluyendo que existe una considerable concentración de oxígeno en la misma, la cual aumenta con el tiempo de exposición en la cámara de vacío.

Para estudiar el comportamiento de la capa como recubrimiento anti reflejante se estimó el índice de refracción n a partir de las medidas de elipsometría, suponiendo que las capas estaban compuestas además por una capa de óxido de silicio y usando el modelo de Cauchy para la regresión. Se obtuvieron mejores resultados para la muestra preparada durante 30 minutos que para la preparada durante 60 minutos, siendo los índices de refracción de 1.91 y 1.82 respectivamente, y siendo ambos resultados próximos al de referencia en bibliografía para el Si_3N_4 (ver *Figure 3.9*). Se concluye que el alto contenido en oxígeno para la muestra preparada durante 60 minutos resulta ser perjudicial para el índice de refracción y para el valor de transmitancia, que a 550 nm resultó ser de 87.3% frente al 91.6% que ofreció la muestra preparada durante 30 minutos.

SiON

Se prepararon muestras similares a las del apartado anterior, pero esta vez añadiendo diferentes flujos de oxígeno a la cámara de sputtering. Tras el tratamiento de los datos de XPS, se concluye que el aumento de la concentración de oxígeno implica el detrimento de la de nitrógeno.

SiO_2/ZnO

Estas capas se prepararon con el objetivo de actuar como capas dieléctricas para la posterior serigrafía con pastas de aluminio sobre ellas, como puede verse en el capítulo siguiente. La primera capa de SiO_2 fue crecida térmicamente en atmósfera de aire, mientras que la de ZnO fue crecida por sputtering a una potencia de 150 W y una presión de trabajo de $1.2 \cdot 10^{-4}$ mbar, obteniéndose espesores de 150 y 200 nm.

Al_2O_3/SiN_x

El objetivo de la preparación de estas capas fue el de que actuaran como capas pasivantes en celdas solares de silicio. Se han realizado ambas por magnetrón sputtering, aplicando 150 W de potencia a ambos targets cerámicos y trabajando a una presión de trabajo de $1.2 \cdot 10^{-4}$ mbar a temperatura ambiente. Se realizaron a varios tiempos para controlar el espesor.

Al:ZnO

Se prepararon capas de ZnO dopado con aluminio en diferentes proporciones, haciendo en este caso co-sputtering con blancos de ZnO y Al_2O_3. El dopaje de aluminio se controló modificando la potencia aplicada al target de alúmina. Se estudió la estructura y morfología de dichas capas como aplicación para celdas solares de silicio de heterounión, en las que actuarían como óxido conductor transparente.

Como era de esperar, la resistividad fue disminuyendo con el incremento de aluminio. Por otro lado, a través de las medidas de transmitancia, se calculó el *bandgap*, concluyendo que las muestras más dopadas serían las mejores para actuar como óxidos conductores transparentes.

CAPÍTULO 4. ESTRUCTURAS DE ALUMINIO IMPRIMIDAS POR SERIGRAFÍA

La pasivación de la superficie trasera aumenta la eficiencia de las celdas solares de silicio, pero requiere unas aperturas locales para la formación de los contactos eléctricos. Dicha apertura normalmente se realiza con un láser o con otros tipos de tecnología que encarecen el proceso. En este capítulo, el objetivo es obtener un campo local superficial trasero sin la necesidad de emplear ninguna técnica adicional. Por esta razón, el LBSF creado ha sido obtenido mediante serigrafía de pastas de aluminio con fritas que permiten la penetración local de la capa pasivante durante el proceso de quemado o *firing*. Este método de contacto a través de la penetración de la pasta durante el quemado (FTC) es bastante nuevo en comparación con las otras técnicas. Mediante el uso de esta técnica, solamente es necesaria la serigrafía, aparte de la técnica de deposición de la capa pasivante, como PECVD. Por tanto, es ventajoso para la producción industrial, debido a la reducción de pasos a lo largo de los procesos de producción de celdas solares.

Con el creciente interés en la creación de contactos locales en la superficie trasera de las celdas solares, el método FTC gana importancia. En esta tesis, se evalúa dicho método mediante el uso de diferentes pastas de aluminio y se consigue una mejora considerable en el área de contacto en comparación con resultados bibliográficos.

En definitiva, el mecanismo FTC presentado emplea una penetración local de la pasta de aluminio a través de la capa dieléctrica durante el quemado, requiriendo solamente el proceso de serigrafía.

Este capítulo se divide en dos partes bien diferenciadas: la serigrafía automática realizada en los laboratorios del Fraunhofer ISE, y la manual, realizada en la Universidad de Málaga.

RESULTADOS Y DISCUSIÓN

Serigrafía automática

Los experimentos con serigrafía automática fueron realizados en los laboratorios del Fraunhofer ISE durante la estancia de la autora de este trabajo en los mismos. En primer lugar, se comprobó la formación del campo local superficial trasero haciendo uso de sustratos de silicio monocristalino tipo p crecidos mediante el método Czochralski y pasivados con capas de SiriON. La formación de dicho campo tuvo lugar tras el quemado y mediante el método FTC.

A continuación se realizó un estudio más detallado, esta vez utilizando sustratos de silicio más puros, obtenidos mediante el método FZ. Se analizó la formación del campo local superficial trasero para dos pastas de aluminio diferentes, A y B, y dos capas pasivantes, SiriON y SiN_x, mediante el método FTC. Para ello, no fue necesaria tecnología adicional a la serigrafía y la técnica para crecer las capas pasivantes, que fue PECVD en este caso. Se crearon diferentes estructuras de aluminio mediante la aplicación local de las pastas por serigrafía, seguido de una capa de cobertura de aluminio. Se estudiaron dos condiciones diferentes de quemado. Los resultados fueron comparados mediante las medidas de las conductividades de contacto a través de la técnica TLM, los valores de velocidad de recombinación obtenidos tras el tratamiento de los datos de QSSPC y las imágenes SEM del corte transversal de las muestras, en las que se observó la penetración de las pastas de aluminio a través de la capa pasivante. Previamente a las medidas de QSSPC, las muestras se sometieron a un decapado químico con HCl para eliminar los residuos de aluminio y, tras ello, se reactivó la pasivación recociéndolas bajo una atmósfera de hidrógeno y nitrógeno (*forming gas*).

Para estas muestras, la densidad de contacto observada tras la eliminación de los residuos de aluminio fue mayor para la pasta A (ver *Figure 4.6*), no observándose influencia alguna de la capa de cobertura y demostrando un claro progreso frente a resultados previos de bibliografía. Esto fue corroborado por las medidas de la resistencia específica de contacto (ver *Figure 4.5*). Además, con dicha pasta se alcanzó una mejor conductividad de contacto que con la pasta B para una misma velocidad de recombinación y condición de quemado (ver *Figure 4.7*). Todo ello se atribuyó a la formación de una capa local p^+ bajo el eutéctico mucho más homogénea en el caso de

la pasta A, que fue examinada mediante el análisis de la microestructura por microscopio electrónico de barrido (ver *Figure 4.8).* Se concluye que la pasta A muestra una alta estabilidad de proceso con baja dependencia de la capa de pasivación y la condición de quemado en comparación con la pasta B.

Serigrafía manual

En primer lugar, se comprobó la formación del campo superficial trasero con la pasta B de manera continua, no local, y se observó mediante imágenes SEM que, efectivamente, se formaba bajo la capa de eutéctico Al-Si. Tras esto, se prepararon muestras con la intención de obtener un campo local superficial trasero a partir de diferentes estructuras creadas en mallas de serigrafía con anchos de línea entre 0.35 y 1.5 mm y 10 mm de largo (ver *Appendix B*) y tres pastas de aluminio llamadas B, T1 y T2. Tras la impresión, las muestras fueron secadas a 220ºC y nuevamente imprimidas y secadas. Por último, se realizó el quemado de las muestras a 950ºC en un horno tubular. Se utilizó como sustrato silicio monocristalino de tipo p de unos 200 μm de espesor, al que se le depositaron diversas capas pasivantes para el estudio del método FTC. El LBSF formado se estudió tanto para los sustratos de silicio como para los de silicio pasivados.

Mediante microscopía óptica se comprobó que las líneas quedaron bien montadas unas sobre las otras y bien adheridas al silicio (ver *Figure 4.15*). Para las líneas imprimidas con las pastas T1 y T2, se observó un color azulado alrededor de las mismas. Tras realizar un EDX se comprobó que se trataba de un aumento de la concentración de oxígeno (ver *Figure 4.16*), lo que se concluyó en que dichas pastas estarían más oxidadas que la pasta B. Las imágenes SEM muestran claramente la formación de una capa dopada p^+ bajo el eutéctico, que resultó tener un espesor en torno a 12 μm para las tres pastas de aluminio (ver *Figure 4.18*). En referencia a los resultados de resistencia específica de contacto, los mejores valores se obtuvieron para anchos de línea de 1.2 mm para la mayoría de las pastas de aluminio empleadas.

Las capas pasivantes depositadas sobre silicio fueron SiO_2 (crecido térmicamente), SiO_2/ZnO y SiriON (crecidos pos magnetrón sputtering). Se estudió el ancho de línea de 1.2 mm, ya que fue el que ofreció mejores resultados de resistencia de contacto sobre silicio y se utilizaron las mismas tres pastas de aluminio. Los mejores valores de resistencia específica de contacto se obtuvieron para la pasta T2 (ver *Figure 4.21*). En relación a las líneas imprimidas con la pasta T2 sobre las tres capas dieléctricas, el mejor valor de resistencia se alcanzó para SiriON. Entonces, según los resultados de pasivación estudiados en el capítulo 3 en los que los mejores valores salieron para la capa de SiriON, podría concluirse que los valores óptimos se obtendrían tras la utilización dela pasta T2 sobre la capa pasivante SiriON. Por otro lado, en las imágenes

SEM (ver *Figure 4.18*) se observa que se obtiene un mayor espesor de la capa dopada p^+ para las muestras que ofrecen una menor resistencia específica de contacto.

CAPÍTULO 5. ESTRUCTURAS DE ALUMINIO IMPRIMIDAS POR DISPENSADO

La utilización de obleas finas de silicio es una vía para reducir costes de material, pero el combado de dichas obleas tras el proceso de metalización puede causar su rotura, aparte de microrroturas en la microestructura, afectando a la vida media de los portadores y, finalmente, a la eficiencia de la celda final. Este efecto puede ser reducido mediante el uso de técnicas de metalización de no contacto como el dispensado, como algunos autores reportan para la obtención de electrodos frontales con pasta de plata.

En este capítulo se demuestra viable la tecnología de dispensado para la formación del campo local superficial trasero sobre diferentes sustratos de silicio tipo p monocristalino (pulido y texturado) mediante el uso de tres pastas de aluminio. Diferentes capas dieléctricas fueron obtenidas sobre silicio con el objetivo de dispensar líneas de aluminio sobre ellas y crear un campo local superficial trasero mediante el método FTC anteriormente comentado. La resistencia específica de contacto de las diferentes estructuras de aluminio fue obtenida para verificar la formación del campo trasero y para una posible aplicación como contactos traseros en celdas solares de silicio. La microestructura aluminio-silicio obtenida tras el proceso de quemado es presentada también para verificar la formación del campo trasero y el espesor de la capa eutéctica es medido para las diferentes muestras.

RESULTADOS Y DISCUSIÓN

Pastas de aluminio

Se utilizaron las mismas pastas de aluminio que las usadas para el proceso de serigrafía manual, llamadas B, T1 y T2, sin modificación alguna. Se estudió el tamaño de partículas de las pastas llegando a la conclusión de que las de la pasta T2 eran las más voluminosas y, por tanto, pasarían con más dificultad por la boquilla. Por ello, para facilitar su paso, la pasta fue calentada mediante la inmersión de la jeringa en un baño de agua a 80ºC.

Impresión de líneas mediante el robot dispensador

El primer paso antes de programar el robot para el dispensado es colocar la boquilla en la posición XYZ deseada. Cuando el programa está preparado, las instrucciones se guardan en la unidad de memoria y se adjudica un orden a seguir. Al accionar el programa, el robot ejecuta las instrucciones en el orden indicado, en este caso para

formar líneas de aluminio (ver *Table 5.1*) a partir del dispensado de pequeños puntos que se van solapando formando dichas líneas.

La masa de pasta depositada por superficie fue medida para cada una de las tres pastas tanto tras el dispensado como tras el secado a 220ºC. Se observó que la cantidad de pasta depositada para T1 y T2 fue mayor que para B.

Campo local superficial trasero sobre silicio monocristalino de tipo p

Las tres pastas de aluminio descritas anteriormente son utilizadas para crear un campo local superficial trasero sobre silico monocristalino de tipo p <100>, 1-3 Ωcm de resistividad y 180-190 μm de espesor. En primer lugar, se llevó a cabo la limpieza de las obleas mediante el proceso descrito en el Appendix A. Seguidamente se realizó el dispensado de las líneas de aluminio utilizando una boquilla de 150 μm y se prosiguió con el secado a 220ºC y el quemado a 950ºC.

Tras el quemado, se utilizó un microscopio óptico para tomar fotografías de las estructuras creadas con las tres pastas de aluminio (ver *Figure 5.6*), donde se pudo observar la buena adhesión de las líneas a los sustratos en los tres casos. Las líneas imprimidas con la pasta B están más esparcidas sobre el sustrato, aumentando el ancho de línea, debido a la menor viscosidad de esta pasta.

Las resistencias específicas de contacto se calcularon tras las medidas de TLM y se obtuvieron los mejores valores para las líneas depositadas con la pasta T2, tanto sobre silicio as-cut como texturado. Comparando el sustrato, se obtuvieron mejores valores para el silicio texturado.

Campo local superficial trasero sobre silicio pasivado. Método FTC

En este apartado se han utilizado las pastas T1 y T2, por ser las que mejor resultado ofrecieron en el apartado anterior. Se han dispensado líneas de 11 mm de largo y 1.2 mm de ancho sobre dos capas pasivantes diferentes, utilizando una boquilla para el robot de 150 μm de diámetro. Una de ellas es SiO_2/SiN_x, compuesta por una primera capa de óxido de silicio crecido térmicamente y, sobre ella, otra capa de nitruro de silicio depositada mediante magnetrón sputtering. La otra capa pasivante es la denominada SiriON, crecida mediante PECVD en los laboratorios del Fraunhofer ISE.

Tras la medida de las resistencias específicas de contacto, se concluye que con la pasta T2 se vuelven a obtener los mejores resultados. En cuanto a las dos capas pasivantes estudiadas, se observa que para la SiriON se obtienen resistencias de contacto menores que para la capa de SiO_2/SiN_x para cualquiera de las dos pastas depositadas.

En definitiva, en este capítulo queda demostrada la viabilidad de la técnica de dispensado para la obtención de un campo local superficial trasero para celdas solares de silicio, aunque debido a que es una técnica novedosa, aún requiere mejoras para obtener resistencias de contacto tan buenas como las obtenidas mediante el método ampliamente usado de la serigrafía.

CAPÍTULO 6. OPTIMIZACIÓN DEL EMISOR DE Al PARA CÉLULAS SOLARES DE CONTACTO TRASERO-UNIÓN TRASERA (BC-BJ)

Las celdas solares de contacto trasero-unión trasera tienen la metalización y los contactos eléctricos localizados en la parte trasera de la célula. Debido a ello, este tipo de celdas tienen una serie de ventajas, destacando la eliminación de las sombras en la parte delantera. En definitiva, estas celdas ofrecen una alta eficiencia, pero también un alto coste de producción.

Uno de los retos relacionados con la estructura de estas celdas solares es el requerimiento de un material de alta calidad, que se traduce en una alta vida media de portador minoritario (τ_{bulk}) y una baja velocidad de recombinación superficial frontal (S_{front}). En las celdas solares de silicio, la mayor parte de la fotogeneración ocurre en la cara frontal de la celda, pero en las celdas con la estructura unión-trasera, la unión pn se localiza en la parte posterior, así que S_{front} debe ser baja porque la mayor parte de los portadores son generados en la parte frontal y se recombinarían para el caso de una alta S_{front}. Además, incluso si la superficie frontal está bien pasivada, existe un riesgo de recombinación dentro del *bulk*. Por tanto, τ_{bulk} y S_{front} son los dos parámetros más críticos para las celdas BC-BJ y deben ser optimizados para alcanzar una alta eficiencia en el dispositivo.

El objetivo de este capítulo es identificar la óptima composición de la pasta de aluminio y las condiciones de quemado en dependencia de las estructuras geométricas del dopaje de aluminio.

RESULTADOS Y DISCUSIÓN

Los sustratos usados en este capítulo han sido obleas de silicio FZ monocristalino de tipo p con una resistividad específica de 8-12 Ωcm, un diámetro de 150 mm y 250 μm de espesor. Tras la limpieza química, las obleas fueron dopadas con fósforo mediante $POCl_3$ para el campo superficial frontal. Las superficie de las obleas fue pasivada con una capa fina de óxido de silicio crecida térmicamente y SiN_x. En dicha capa, se realizaron una serie de aperturas de diferentes tamaños con la intención de, posteriormente, imprimir mediante serigrafía las diferentes pastas de aluminio en los huecos creados con formas de líneas y puntos (ver *Figure 6.2*).

Resistencia de contacto

Se llevaron a cabo medidas de TLM para analizar la resistencia de los contactos traseros imprimidos con diferentes pastas de aluminio tras el quemado a diferentes condiciones en un horno tubular. Las líneas imprimidas tienen diferentes anchos y un espaciado entre centro y centro de línea de 2 mm. En la *Table 6.2* se muestran las características de las muestras: tipo de pasta de aluminio y de quemado.

Para las pastas de aluminio A y P, pudo concluirse que la mejor condición de quemado fue 860ºC de temperatura a una velocidad de 2600 mm/min, obteniéndose mejores (aunque muy similares) valores de resistencia de contacto específica efectiva para la pasta P (ver *Figure 6.4*).

También se utilizaron otras pastas de aluminio, a las que se le añadieron otros componentes, como es el caso de las pastas P+BO y AlB3%, que contienen boro en su composición. En este caso, para la condición de quemado de 910ºC y 4200 mm/min de velocidad se obtuvieron mejores valores de resistencia para la pasta P+BO (ver *Figure 6.5*), aunque fueron muy similares, observándose una mayor diferencia para anchos de línea de 1231 µm.

Velocidad de recombinación superficial efectiva

A través de las medidas realizadas mediante QSSPC se analizó la velocidad de recombinación superficial efectiva (S_{eff}) de las diferentes estructuras de aluminio creadas (ver *Table 6.3*). Para ello, antes de realzar la medida se introdujeron las muestras en un baño ultrasónico de HCl para eliminar el aluminio y, tras ello, se les aplicó un recocido en horno en atmósfera de *forming gas* para reactivar la pasivación.

Para las estructuras de líneas de aluminio, el valor más bajo de S_{eff} se obtuvo para líneas de 1300 µm de ancho imprimidas con la pasta P+AlB1.5% y quemadas a una temperatura pico de 960ºC a la velocidad de 5200 mm/min. En el caso de las estructuras de puntos, el valor más bajo se obtuvo para la pasta A+AlB, para la misma condición de quemado. Por tanto, a nivel de resultados para la mejora de la pasivación, se concluye que la mejor condición de quemado es a 960ºC a la velocidad de 5200 mm/min.

Estudio de la microestructura

Para realizar imágenes con el microscopio electrónico de barrido, previamente se realizaron cortes transversales a las muestras para observar las capas bien diferenciadas de pasta de aluminio, eutéctico y capa dopada p^+ (emisor) bajo el eutéctico Al-Si.

La capa de emisor de aluminio de mayor espesor fue observada para las obleas imprimidas con las pastas A y P+AlB3%. Las muestras presentaron una capa de emisor más delgada en el centro de los puntos que en los bordes (ver *Figure 6.10*), debido probablemente a la expansión de la pasta de aluminio hacia los bordes durante la serigrafía, permitiendo así una mayor difusión.

Appendix E. Conclusiones

- Se han preparado capas finas sobre silicio mediante oxidación térmica, PECVD y magnetrón sputtering, cuyas propiedades de capas pasivantes, capas anti reflejantes u óxidos conductores transparentes para aplicación en células de silicio de heterounión se han analizado mediante diversas técnicas de caracterización.

- De todas las capas pasivantes obtenidas mediante PECVD, la denominada SiriON fue la que ofreció una mayor vida media de portadores minoritarios, alcanzando el valor de 1476.45 μs tras un tratamiento a alta temperatura y el recocido en atmósfera de hidrógeno y nitrógeno.

- Las capas de SiN_x preparadas por magnetrón sputtering tuvieron una transmitancia máxima a 550 nm de 91.6% y un índice de refracción máximo de 1.91, calculado a partir de las medidas de elipsometría. Se concluye que un alto contenido en oxígeno en las muestras implica un menor índice de refracción y un valor de transmitancia más bajo.

- La transmitancia de las capas de ZnO dopadas con aluminio fue demostrada, obteniéndose un mayor valor de la energía de band gap para las muestras más dopadas, alcanzando el valor máximo de 3.57 eV. Dichas muestras fueron también las más conductoras, así que podría concluirse que, frente a las demás estudiadas, serían las óptimas para actuar como TCOs en células de heterounión.

- Mediante serigrafía automática realizada durante la estancia de la autora de este trabajo en los laboratorios Fraunhofer ISE de Alemania, se obtuvo un campo local superficial trasero mediante el uso de diferentes pastas de aluminio, A y B, sobre dos capas pasivantes, SiriON y SiN_x crecidas sobre silicio, haciendo uso del método FTC como alternativa a otros métodos para la reducción de costes. Se obtuvieron mejores resultados con la nueva pasta A, obteniéndose así una mayor área de contacto y una mejor conductividad específica de contacto. Además, para una misma velocidad de recombinación y condición de quemado, la pasta A ofreció mejor conductividad de contacto, lo que se atribuyó a la formación de una capa dopada p^+ más homogénea observada en el análisis de la microestructura.

- Se optimizó el uso de la serigrafía manual para la obtención del campo local superficial trasero sobre sustratos de silicio y capas pasivantes crecidas sobre silicio. Se utilizaron diferentes mallas creadas con el fin de obtener

estructuras de aluminio de entre 0.35 y 1.5 mm de ancho y tres pastas de aluminio llamadas B, T1 y T2. Los mejores valores de resistencia específica de contacto se obtuvieron para anchos de línea de 1.2 mm para la mayoría de las pastas imprimidas sobre silicio, por lo que se utilizó dicho ancho de línea para crear el campo trasero sobre las obleas de silicio pasivadas. Los valores óptimos se obtuvieron tras la utilización de la pasta T2 sobre la capa pasivante SiriON.

- Se ha demostrado la viabilidad de la técnica de dispensado para la formación de un campo local superficial trasero a partir de las mismas pastas de aluminio utilizadas en la serigrafía manual. Utilizando silicio como sustrato, los mejores valores de resistencia específica de contacto se obtuvieron para líneas de 1.2 mm de ancho dispensadas con la pasta T2. Mediante el método FTC, se depositaron las pastas T1 y T2 sobre dos capas pasivantes, SiriON y SiO_2/SiN_x. Se obtuvieron los mejores valores para la capa de SiriON, creándose el campo local superficial trasero para las dos pastas estudiadas sobre las dos capas pasivantes, quedando demostrado mediante las medidas de resistencia y el análisis microestructural.

- Se optimizó el emisor de aluminio para celdas solares de contacto-trasero unión-trasera, mediante el uso de varias pastas de aluminio y mezclas de las mismas con boro y óxido de boro. Se establece un quemado óptimo para la disminución de la velocidad de recombinación, lo que se traduce en una mejora de la pasivación de la celda. Se demuestra una mejora en cuanto a la resistencia específica de contacto mediante el uso de pastas de aluminio mezcladas con compuestos de boro.

Bibliography

[1] *http://solargis.info*

[2] International Energy Agency (IEA), "Technology roadmap: solar photovoltaic energy", (2014).

[3] R. Woehl, "All-Screen-Printed Back-Contact Back-Junction Silicon Solar Cells with Aluminum-Alloyed Emitter", PhD Thesis, Universität Freiburg, (2011).

[4] J.D.Hylton, "Light coupling and light trapping in alkaline etched multicrystalline silicon wafers for solar cells", PhD Thesis, Universiteit Utrecht, (2006).

[5] C. Simeon, Baker-Finch, and Keith R. McIntosh, "Reflection distributions of textured monocrystalline silicon: implications for silicon solar cells", *Progress in Photovoltaics: Research and Applications*, vol. 21, issue 5, 960–971, (2013).

[6] J. N. Ximello, "Wet chemical textures for crystalline silicon solar cells", PhD Thesis, Universität Konstanz, (2013).

[7] P. Lalanne and G. M. Morris, "Antireflection behavior of silicon subwavelength periodic structures for visible light", *Nanotechnology*, vol. 8, 53-56, (1997).

[8] J. C. Vázquez, "Contribución a la mejora del rendimiento de células solares industriales", PhD Thesis, Universidad de Málaga, (2010).

[9] B. Liu, S. Qiu, N. Chen, G. Du, and J. Sun, "Double-layered silicon nitride antireflection coatings for multicrystalline silicon solar cells", *Materials Science in Semiconductor Processing*, vol. 16, 1014–1021, (2013).

[10] S. Duttagupta, F. Ma, B. Hoex, T. Mueller, and A. G. Aberle, "Optimised Antireflection Coatings using Silicon Nitride on Textured Silicon Surfaces based on Measurements and Multidimensional Modelling", *Energy Procedia,* vol. 15, 78-83, (2012).

[11] S. Strehlke, S. Bastide, J. Guillet, and C. Lévy-Clément, "Design of porous silicon antireflection coatings for silicon solar Cells", *Materials Science and Engineering B*, vol. 69, 81–86, (2000).

[12] E. Osorio, R. Urteaga, L.N. Acquaroli, G.García-Salgado, H.Juaréz, *et al.*, "Optimization of porous silicon multilayer as antireflection coatings for solar cells", *Solar Energy Materials & Solar Cells,* vol. 95, 3069-3073, (2011).

[13] D. Hocine, M.S. Belkaid, M. Pasquinelli, L. Escoubas, J.J. Simon, *et al*., "Improved efficiency of multicrystalline silicon solar cells by TiO_2 antireflection coatings derived by APCVD process", *Materials Science in Semiconductor Processing,* vol. 16, 113–117, (2013).

[14] L. Remache, E. Fourmond, A. Mahdjoub, J. Dupuis, and M. Lemiti, "Design of porous silicon/PECVD SiO_x antireflection coatings for silicon solar cells", *Materials Science and Engineering B*, vol. 176, 45-48, (2011).

[15] S-Y. Lien, D-S. Wuu, W-C Yeh, and J-C. Liu, "Tri-layer antireflection coatings ($SiO_2/SiO_2–TiO_2/TiO_2$) for silicon solar cells using a sol–gel technique", *Solar Energy Materials & Solar Cells,* vol. 90, 2710-2719, (2006).

[16] D. K. Schroder , "Semiconductor Material and device Characterization", Wiley-Interscience, third edition, (2006).

[17] R. Hull, "Properties of crystalline silicon", INSPEC, United Kingdom, (1999).

[18] L.A. Dobrzański, M. Musztyfaga, A. Drygala, and P. Panek, "Investigation of the screen printed contacts of silicon solar cells using Transmission Line Model", *Journal of Achievements in Materials and Manufacturing Engineering*, vol. 41, 57-65, (2010).

[19] G. K. Reeves and H. B. Harrison, "Obtaining the specific contact resistance from transmission line model measurements", *IEEE Electron Device Letters*, vol. 3, 111-113, (1982).

[20] A. Cuevas and D. Macdonald, "Measuring and interpreting the lifetime of silicon wafers", *Solar Energy,* vol. 76, 255-262, (2004).

[21] H. Nagel, C. Berge, and A. G. Aberle, "Generalized analysis of quasi-steadystate and quasi-transient measurements of carrier lifetimes in semiconductors", *Journal of Applied Physics*, vol. 86, 6218-6221, (1999).

[22] M. J. Kerr, "Surface, Emitter and Bulk Recombination in Silicon and Development of Silicon Nitride Passivated Solar Cells", PhD Thesis, Australian Nacional University, (2002).

[23] D. E. Kane and R. M. Swanson, "Measurement of the emitter saturation current by a contactless photoconductivity decay method", *Proceedings of the 18th IEEE Photovoltaic Specialists Conference*, Las Vegas, Nevada, USA, 578-583, (1985).

[24] T. Trupke, M. A. Green, P. Würfel, P. P. Altermatt, A. Wang, *et al*., "Temperature dependence of the radiative recombination coefficient of intrinsic crystalline silicon", *Journal of Applied Physics*, vol. 94, 4930-4937, (2003).

[25] M. J. Kerr and A. Cuevas, "General parameterization of Auger recombination in crystalline silicon", *Journal of Applied Physics*, vol. 91, 2473-2480, (2002).

[26] W. D. Eades and R. M. Swanson, "Calculation of surface generation and recombination velocities at the Si-SiO_2 interface", *Journal of Applied Physics*, vol. 58, 4267, (1985).

[27] M. Wolf, "Drift fields in photovoltaic solar energy converter cells", *Proceedings IEEE*, vol. 51, 674, (1963).

[28] G. Agostinelli, J. Szlufcick, P. Choulat, and G. Beaucarne, "Local contact structures for industrial PERC-type solar cells", *Proceedings of the 20th European Photovoltaic Solar Energy Conference,* Milan, Italy, 1011-1014, (2007).

[29] T. Lauermann, T. Lüder, S. Scholz, B. Raabe, G. Hahn, *et al*., "Enabling dielectric

rear side passivation for industrial mass production by developing lean printing-based solar cell processes", *Proceedings of the 35th European Photovoltaic Solar Energy Conference*, Barcelona, Spain, 942-945, (2005).

[30] A. Uruena, J. John, G. Beaucarne, P. Choulat, P. Eyebeb *et al*., "Local Al-alloyed contacts for next generation Si solar cells", *Proceedings of the 24th IEEE Photovoltaic Specialists Conference*, Honolulu, Hawaii, 28-33, (2010).

[31] F. Huster, "Investigation of the alloying process of screen printed aluminum pastes for the BSF formation on silicon solar cells", *Proceedings of the 20th European Photovoltaic Solar Energy Conference*, Barcelona, Spain, 1466-1469, (2005).

[32] J. Krause, R. Woehl, M. Rauer, C. Schmiga, J. Wilde *et al*., "Microstructural and electrical properties of different-sized aluminum-alloyed contacts and their layer system on silicon surfaces", *Solar Energy Materials & Solar Cells,* vol. 95, 2151-2160, (2011).

[33] J. del Alamo, J. Eguren, and A. Luque, "Operating limits of Al-alloyed high-low junctions for BSF solar cells", *Solid-State Electronics,* vol. 24, 415-420, (1981).

[34] S. Shankar, Y. W. Riddle, and M. M. Makhlouf, "Nucleation mechanism of the eutectic phases in aluminum-silicon hypoeutectic alloys", *Acta Materialia,* vol. 52, 4447-4460, (2004).

[35] S. Riegel, F. Mutter, T. Lauermann, B. Terheiden, and G. Hahn, "Review on screen printed metallization on p-type silicon", *Energy Procedia*, vol. 21, 14-23, (2012).

[36] A. Kaminskia, B. Vandellea, A. Favea, J. P. Boyeauxa, R. Monnab *et al*., "Aluminum BSF in silicon solar cells", *Solar Energy Materials and Solar Cells,* vol. 72, 373-379, (2002)..

[37] V. Shanmugam, J. Cunnusamy, A. Khanna, M. B. Boreland, and T. Mueller, "Optimisation of Screen-Printed Metallisation for Industrial High-Efficiency Silicon Wafer Solar Cells", *Energy Procedia*, vol. 33, 64-69, (2013).

[38] Y. T. Gizachew , L. Escoubas, J. J. Simon, M. Pasquinelli, J. Loiret, *et al*., " Towards ink-jet printed fine line front side metallization of crystalline silicon solar cells", *Solar Energy Materials & Solar Cells,* vol. 95, 70-82, (2011).

[39] D-H. Kim, S-S. Ryu, D. Shin, J-H. Shin, J-J. Jeong *et al*., "The fabrication of front electrodes of Si solar cell by dispensing printing", *Material Science and Engineering B*, vol. 177, 217-222, (2012).

[40] M. Pospischil, M. Klawitter, M. Kuchler, J. Specht, H. Gentischer, *et al*., "Process Development for a High-Throughput Fine Line Metallization Approach Based on Dispensing Technology", *Energy Procedia*, vol. 43, 111-116, (2013).

[41] M. Pospischil, T. Fellmeth, A. Brand, S. Nold, M. Kuchler, *et al*., "Optimizing Fine Line Dispensed Contact Grids", *Energy Procedia*, vol. 55, 693-701, (2014).

[42] F. Karouta, K. Vora, J. Tian, and C. Jagadish, "Structural, compositional and optical properties of PECVD silicon nitride layers", *Journal of Physics D:*

Applied Physics, vol. 45, 445301, (2012).

[43] M. Hofmann, N. Kohn, F. Schwarz, S. Nölker, S. Kastl, *et al*, "High-power-plasma PECVD of SiN_x and Al_2O_3 for industrial solar cell manufacturing". *Proceedings of the 28th European Photovoltaic Solar Energy Conference*, Paris, France, (2013).

[44] L. Remache, E. Fourmond, A. Mahdjoub, J. Dupuis, and M. Lemiti, "Design of porous silicon/PECVD SiO_x antireflection coatings for silicon solar cells", *Materials Science and Engineering: B*, vol. 176, issue 1, 45-48, (2011).

[45] Z. R. Chowdhury, H. Nabovati, and N. P. Kherani, "Effects of Gas Flow Ratio on Optical Properties of PECVD Grown Single Layer Anti-reflecting Coating for Silicon Solar Cells", *Journal of Electrical Systems and Signals*, vol. 1, no. 2, (2013).

[46] J. M. Albella, "Láminas delgadas y recubrimientos", Ed. CSIC, (2003).

[47] X. Zhang, A. Cuevas, B. Demaurex, and S. D. Wolf, "Sputtered hydrogenated amorphous silicon for silicon heterojunction solar cell fabrication", *Energy Procedia*, vol. 55, 865-872, (2014).

[48] S. W. Glunz, R. Preu, S. Schaefer, E. Schneiderlochner, W. Pfleging, *et al*., "New simplified methods for patterning the rear contact of RP-PERC high-efficiency solar cells", *Proceedings of the 28th IEEE Photovoltaic Specialists Conference*, Anchorage, Alaska, USA, 168-171, (2000).

[49] S. Konstantinidis, K. Jiang, A. Roobroek, F. Renaux, and J. M. Schneider, "Pulsed Plasma Enhanced Chemical Vapor Deposition of Alumina Thin Films: Influence of the Duty Cycle on Structure and Elastic Properties", *Plasma Processes and Polymers,* vol. 8, issue 7, 651-657, (2011).

[50] V. Naumann, M. Otto, R. B. Wehrspohn, M. Werner, and C. Hagendorf, "Interface and Material Characterization of Thin ALD-Al_2O_3 Layers on Crystalline Silicon", *Energy Procedia*, vol. 27, 312-318, (2012).

[51] G. He, X. Wang, M. Oshima, and Y. Shimogaki, "Metalorganic Chemical Vapor Deposition of Al_2O_3 Thin Films from Dimethylaluminumhydride and O_2", *Japanese Journal of Applied Physics*, vol. 49, 1502, (2010).

[52] L. Liu, W-G Liu, N. Cao, and C-L Cai, "Study on The Performance of PECVD Silicon Nitride Thin Films", *Defence Technology,* vol. 9, 121-126, (2013).

[53] T. Dullweber, R. Hesse, V. Bhosle, and C. Dubé, "Ion-implanted PERC solar cells with Al_2O_3/SiN_x rear passivation", *Energy Procedia*, vol. 38, 430-435, (2013).

[54] T. Lüdera, T. Lauermann, A. Zuschlag, G. Hahn, and B. Terheiden, "Al_2O_3/SiN_x-Stacks at Increased Temperatures: Avoiding Blistering During Contact Firing", *Energy Procedia*, vol. 27, 426-431, (2012).

[55] J. A. Tofflinger, A. Laades, C. Leendertz, L. M. Montanez, L. Korte, U. Sturzebecher *et. al*., "PECVD-AlO_x/SiN_x passivation stacks on silicon: Effective charge dynamics and interface defect state spectroscopy", *Energy Procedia*,

vol. 55, 845-854, (2014).

[56] B. Veith, F. Werner, D. Zielke, R. Brendel, and J. Schmidt, "Comparison of the thermal stability of single Al_2O_3 layers and Al_2O_3/SiN_x stacks for the surface passiviation of silicon", *Energy Procedia*, vol. 8, 307-312, (2011).

[57] L. Yao and J. He, "Recent progress in antireflection and self-cleaning technology -From surface engineering to functional surfaces", *Progress in Materials Science*, vol. 61, 94-143, (2014).

[58] X. Wu, Z. Zhan, Y. Liu, X. Chu, and Y. Li, "Process parameter selection study on SiN_x:H films by PECVD method for silicon solar cells", *Solar Energy*, vol. 111, 277-287, (2015).

[59] U. Ozgtir, Y. I. Alivov, A. Teke, M. A. Reshchikov, and S. Dogan, "A comprehensive review of ZnO materials and devices", *Journal of Applied Physics*, vol. 98, 041301, (2005).

[60] T. Minami, "Present status of transparent conducting oxide thin-film development for Indium-Tin-Oxide (ITO) substitutes", *Thin Solid Films*, vol. 516, 5822-5828, (2008).

[61] A.V. Singh, R. M. Mehra, N. Buthrath, A. Wakahara, and A. Yoshida, "Highly conductive and transparent aluminum-doped zinc oxide thin films prepared by pulsed laser deposition in oxygen ambient", *Journal of Applied Physics*, vol. 90, 5661-5665, (2001).

[62] D. G. Baik and S. M. Cho, "Application of sol-gel derived films for ZnO/n-Si junction solar cells", *Thin Solid Films*, vol. 354, 227-231, (1999).

[63] S. Xu, Z. Liang and H. Shen, "The preparation of AZO/a-Si/c-Si heterojunction structure on p-type silicon substrate for solar cell application", *Materials Letters*, vol. 137, 428-431, (2014).

[64] O. Lupan, T. Pauporté, B. Viana, I. M. Tiginyanu, V. V. Ursaki, *et al*., "*Epitaxial electrodeposition of ZnO nanowire arrays on p-GaNfor efficient UV-light-emitting diode fabrication", ACS Applied Materials and Interfaces, vol. 2, issue 7, 2083-2090, (2010).*

[65] D. J. Rogers, F. H. Teherani, A. Yasan, K. Minder, P. Kung, *et al*., "Electroluminescence at 375 nm from a ZnO/GaN:Mg/c-Al_2O_3 heterojunction light emitting diode", *Applied Physics Letters*, vol. 88, 141918, (2006).

[66] T. P. Chen, S. J. Young, S. J. Chang, C. H. Hsiao, and C. S. Huang, "Field-Emission and Photoelectrical Characteristics of ZnO Nanorods Photodetectors Prepared on Flexible Substrate", *Journal of the Electrochemical Society*, vol. 159, no. 5, J153, (2012).

[67] D. Zhang, I. A. Digdaya, R. Santbergen, R.A.C.M.M. van Swaaij, P. Bronsveld, *et al*., "Design and fabrication of a SiO_x/ITO double-layer anti-reflective coating for heterojunction silicon solar cells", *Solar Energy Materials & Solar Cells*, vol. 117, 132-138, (2013).

[68] E. Urrejola, "Aluminum-silicon contact formation through narrow dielectric

openings", PhD Thesis, Universität Konstanz, (2012).

[69] A. G. Aberle, "Crystalline silicon solar cells: advanced surface passivation and analysis", University of New South Wales, Sydney NSW 2052, Australia, (1999).

[70] A. Ulyashin, D.N. Wright, A. Bentzen, A. Suphellen, E. Marstein, *et al*., "Optical and passivation properties of double layer a-Si:h/SiN_x anti-reflective coatings for silicon solar cells", *Proceedings of the 22nd European Photovoltaic Solar Energy Conference*, Milan, Italy, 1690-1693, (2007).

[71] B. Karunagaran,J. P. Jeong, S. Nagarajan, S. J. Chung, and E. -K. Suh, "Low-Temperature Deposition of Silicon-Nitride Layers by Using PECVD for High Efficiency Si Solar Cells", *Journal of the Korean Physical Society*, vol. 48, no. 6, 1250-1254, (2006).

[72] R. Woehl, J. Krause, F. Granek, and D. Biro, "19.7% Efficient All-Screen-Printed Back-Contact Back-Junction Silicon Solar Cell With Aluminum-Alloyed Emitter", IEEE Electron Device Letters, vol. 32, no. 3, 345-347, (2011).

[73] I. Cesar, E. Bende, G. Galbiati, L. Janssen, A .Weeber *et al*., "All-side SiN_x passivated mc-Si solar cells evaluated with respect to parasitic shunting", *Proceedings of the 34th IEEE Photovoltaic Specialists Conference*, Philadelphia, Pennsylvania, USA, 1386-1391, (2009).

[74] J. Seiffe, L. Weiss, M. Hofmann, L. Gautero, and J. Rentsch, "Alternative rear surface passivation for industrial cell production", *Proceedings of the 23rd European Photovoltaic Solar Energy Conference*, Valencia, Spain, 1700-1703, (2008). SiriON

[75] J. Dupuis, E. Fourmond, O. Nichiporuk, F. Gibaja, and M. Lemiti, "Rear passivation schemes for industrial silicon solar cells", *Proceedings of the 23rd European Photovoltaic Solar Energy Conference*, Valencia, Spain, 1633-1636, (2008).

[76] C. Agashe, O. Kluth, J. Hüpkes, U. Zastrow, B. Rech, *et al*., "Efforts to improve carrier mobility in RF sputtered ZnO:Al films", *Journal of Applied Physics*, vol. 95, 1911, (2004).

[77] K. K. Kim, J. H. Song, H. J. Jung, W. K. Choi, S. J. Park, *et al*., "The grain size effects on the photoluminescence of ZnO/alpha Al_2O_3 grown by radio-frequency magnetron sputtering", *Journal of Applied Physics*, vol. 87, 3573-3575, (2000).

[78] C. H. Tseng, C. H. Huang, H. C. Chang, D. Y. Chen, C. P. Chou *et al*., "Structural and optoelectronic properties of Al-doped zinc oxide films deposited on flexible substrates by radio frequency magnetron sputtering", *Thin Solid Films*, vol. 519, 7959-7965 (2011).

[79] B. Mayumi, Takeyama, Masaru Sato, Yoshihiro Nakata, Yasushi Kobayashi, *et al*., "Characterization of silicon nitride thin films deposited by reactive sputtering and plasma-enhanced CVD at low temperatures", *Japanese Journal*

of Applied Physics, vol. 53, 05GE01, (2014).

[80] John F. Moulder, "Handbook of X-ray Photoelectron Spectroscopy*",* Ed. Physical Electronics Division, (1995).

[81] T. Pauporté, "Design of solution-grown ZnO nanostructures", *Towards Functional Nanomaterials*, 77-125, (2009).

[82] J. Schmidt , A. Merkle, R. Brendel, B. Hoex, M. C. M. van de Sanden, *et al*., "Surface passivation of high-efficiency silicon solar cells by atomic-layer-deposited Al_2O_3", *Progress in Photovoltaics*, vol. 16, 461-466, (2008).

[83] S. Gatz, H. Plagwitz, P. P. Altermatt, B. Terheiden, and R. Brendel, "Thermal stability of amorphous silicon/silicon nitride stacks for passivating crystalline silicon solar cells", *Applied Physics Letters*, vol. 93, 173502, (2008).

[84] M. Gabás, A. Landa-Cánovas, J. L. Costa-Krämer, F. Agulló-Rueda, A. R. González-Elipe, *et al*., "Differences in n-type doping efficiency between Al- and Ga-ZnO films", *Journal of Applied Physics*, vol. 113, 163709, (2013).

[85] P. Nunes, E. Fortunato, P. Tonello, F. Braz Fernandes, P. Vilarinho, *et al*., "Effect of different dopant elements on the properties of ZnO thin films", *Vacuum*, vol. 64, 281-285, (2002).

[86] B. K. Sharma and N. Khare, "Stress-dependent band gap shift and quenching of defects in Al-doped ZnO films", *Journal of Physics D: Applied Physics*, vol. 43, 465402, (2010).

[87] S. Mondal, S. R. Bhattacharyya and P. Mitra, "Effect of Al doping on microstructure and optical band gap of ZnO thin film synthesized by successive ion layer adsorption and reaction", *Pramana-Journal of Physics*, vol. 80, 315-326, (2013).

[88] J. Sengupta, R.K. Sahoo and C.D. Mukherjee, "Effect of annealing on the structural, topographical and optical properties of sol–gel derived ZnO and AZO thin films", *Materials Letters*, vol. 83, 84-87, (2012).

[89] C. Bundesmann, N. Ashkenov, M. Schubert, D. Spemann, T. Butz, *et al*., "Raman scattering in ZnO thin films doped with Fe, Sb, Al, Ga and Li", *Applied Physics Letters*, vol. 83, 1974-1976, (2003).

[90] M. Gabás, P. Díaz-Carrasco, F. Agulló-Rueda, P. Herrero, A. R. Landa-Cánovas, *et al.,* "High quality ZnO and Ga:ZnO thin films grown onto crystalline Si (100) by RF magnetron sputtering", *Solar Energy Materials & Solar Cells*, vol. 95, 2327-2334, (2011).

[91] E. Schneiderlöchner, R. Preu, R. Lüdemann *et al.,"*Laser-Fired Contacts (LFC)", *Proceedings of the 17th European Photovoltaic Solar Energy Conference,* 1303-1306, (2001).

[92] R. Preu, S. W. Glunz, S. Schäfer *et al.,* "Laser ablation-a new low-cost approach for passivated rear contact formation in crystalline silicon solar cell technology", *Proceedings of the 16th European Photovoltaic Solar Energy Conference and Exhibition,* 1181-1184, (2000).

[93] M. Rauer, C. Schmiga, K. Ruhle, *et al*., "Investigation of aluminum-alloyed local contacts for rear surface-passivated silicon solar cells", *IEEE Journal of Photovoltaics*, vol. 1, 22-28, (2011).

[94] J. Song, S. Park, S. Kwon, *et al*., "A study on the aluminum fire-through to a-SiNx:H thin film for crystalline solar cells", *Current Applied Physics,* vol. 12, 313-318, (2012).

[95] B. Thaidigsmann, C. Kick, A. Drews, F. Clement, A. Wolf, *et al.,* "Fire-through contacts-a new approach to contact the rear side of passivated silicon solar cells*", Solar Energy Materials & Solar Cells*, vol. 108, 164-169, (2013).

[96] C. Kick, B. Thaidigsmann, M. Linse, F. Clement, A. Wolf, *et al.,* "Printed fire-through contacts (FTC) - an alternative approach for local rear contacting of passivated solar cells", *Proceedings of the 27th European Photovoltaic Solar Energy Conference,* 544-546, (2012).

[97] E. Navarrete, A. Kimmerle, B. Thaidigsmann, R. Woehl, J.R. Ramos-Barrado, *et al.*, "Evaluation of fire-through aluminum pastes for local contact formation in silicon solar cells*", Proceedings of the 28th European Photovoltaic Solar Energy Conference and Exhibition*, Paris, France, 1839-1841, (2013).

[98] J. Seiffe, L.Gautero, M. Hofmann, et al., "Surface passivation of crystalline silicon by plasma-enhanced chemical vapor deposition double layers of silicon-rich silicon oxynitride and silicon nitride", *Journal of Applied Physics,* vol. 109, 034105, (2011).

[99] E. Urrejola, K. Peter, H. Plagwitz, and G. Schubert, "Silicon diffusion in aluminum for rear passivated solar cells", *Applied Physics Letters*, vol. 98, 153508, (2011).

[100] P-H. Tsai, Y-N. Chang, C-W. Chen, W-P. Chen, and C-H. Wu, "Bow analysis after soldering process for silicon solar cell with special bus bar pattern design", *Proceedings of the 27th European Photovoltaic Solar Energy Conference,* 845-847, (2012).

[101] B. Bunkenburg, S. Kim, B. Cruz, and K. Barringer, "Enabling thin wafers for today's high efficiency silicon solar cells", *Advancing solar technology*.

[102] Chen, X., K. Church, and X. Yang, "High speed non-contact printing for solar cell front side metallization", *Proceedings of the 35th IEEE Photovoltaic Specialists Conference*, 1343-1347, (2010).

[103] M. Balucani, L. Serenelli, K. Kholostov, P. Nenzi, M. Miliciani, *et al.,* "Aluminum-Silicon interdiffusion in screen printed metal contacts for silicon based solar cells applications", *Energy Procedia*, vol. 43, 100-110, (2013).

[104] T. Miyoshi, S. Hara, T. Mukai, and K. Higashi, "Development of a Closed Cell Aluminum Alloy Foam with Enhancement of the Compressive Strength", *Materials Transactions*, vol. 42, 2118-2123, (2001).

[105] N. Eustathopoulos, J. C. Joud, P. Desre, and J. M. Hicter, "The wetting of carbon by aluminium and aluminium alloys", *Journal of Materials Science*, vol. 9, issue

8, 1233-1242, (1974).

[106] J. Hashim, L. Looney, and M. S. J. Hashmi, "The wettability of SiC particles by molten aluminium alloy", *Journal of Materials Processing Technology*, vol. 119, 324-328, (2001).

[107] K. Mangersnes, "Back-contacted back-junction silicon solar cells", PhD Thesis, University of Oslo, (2010).

[108] R. Keding, D. Stüwe, M. Kamp, C. Reichel, *et al*., "Co-diffused back-contact back-junction silicon solar cells", *Proceedings of the 28th European Photovoltaic Solar Energy Conference*, Paris, France, (2013).

[109] S. W. Glunz, R. Preu, and D. Biro, "Crystalline silicon solar cells. State-of-the-art and future developments", *Comprehensive Renewable Energy*, vol 1, chapter 1.16, (2012).

[110] Filip Granek, "High-efficiency back-contact back-junction silicon solar cells". PhD Thesis, Universität Freiburg im Breisgau, (2009).

[111] K. Sinapis and M. van den Donker, "State of the art in Building Integrated Photovoltaics", BIPV report 2013.

[112] A. Edler, "Development of bifacial n-type solar cells for industrial application", PhD Thesis, Universität Konstanz, (2014).

[113] F. Granek, C. Reichel, M. Hermle, D. M. Huljić, O. Schultz, *et al*., "Front surface passivation of n-type high-efficiency back-junction silicon solar cells using front surface field", *Proceedings of the 22nd European Photovoltaic Solar Energy Conference*, Milan, Italy, 1454, (2007).

[114] T. Trupke, B. Mitchell, J. W. Weber, W. McMillan, R.A. Bardos *et al.,* "Photoluminescence Imaging for Photovoltaic Applications", *Energy Procedia*, vol. 15, 135-146, (2012).

[115] T. Trupke, R. A. Bardos, M. D. Abbott, P. Würfel, E. Pink, *et al*., "Progress with luminescence imaging for the characterization of silicon wafers and solar cells", *Proceedings of the 22nd European Photovoltaic Solar Energy Conference*, Milan, Italy, 22-31, (2007).